

**Exclusive η Meson Reconstruction
in Proton-Proton Collisions at 2.2 GeV
with the HADES Spectrometer
and
High Resolution Tracking**

Vom Fachbereich Physik
der Technischen Universität Darmstadt

zur Erlangung des Grades
eines Doktors der Naturwissenschaften
(Dr. rer. nat.)

genehmigte Dissertation von
Master-Phys. Anar Rustamov
aus Shamakhi, Aserbaidshan

Referent: Prof. Dr. Peter Braun-Munzinger
Korreferent: Prof. Dr. Jochen Wambach

Tag der Einreichung: 5. Juli 2006
Tag der Prüfung: 26. Juli 2006

Darmstadt 2006
D17

Declaration of Originality

With this I confirm that this doctoral thesis contains the results of my research carried out at GSI in Darmstadt.

Excluding an introductory part the research described in this thesis is original unless an explicit reference is made to work of others. I further state that no part of this thesis has been submitted for any qualification other than the degree Dr. rer. nat. at the Technical University of Darmstadt.

Zusammenfassung

HADES (**H**igh **A**cceptance **D**i**E**lectron **S**pectrometer) ist ein Di-Elektronen-Spektrometer, das am Schwer Ionen Synchrotron (SIS) an der GSI in Darmstadt aufgebaut wurde.

Das Physik Programm von HADES befasst sich hauptsächlich mit den in-Medium Eigenschaften der leichten Vektormesonen $\rho(770)$, $\omega(783)$ und $\phi(1020)$, sowie verschiedenen anderen wichtigen Fragestellungen der Physik der Hadronen, wie etwa der Gültigkeit des Vektordominanzmodells (VDM) zur Beschreibung von Meson und Baryon-Dalitzzerfällen und dem elektromagnetischen Formfaktor des Nukleons in der zeitartigen Region.

Die vorliegende Arbeit präsentiert eine detaillierte Analyse der exklusiven Rekonstruktion des η -Mesons in Proton-Proton- Kollisionen bei einer kinetischen Energie des einfallenden Protons von 2,2 GeV. Die exklusive Messung des η -Mesons wurde in den zwei elektromagnetischen Zerfallskanälen des η -Mesons ($\eta \rightarrow \pi^+\pi^-\pi^0$ und $\eta \rightarrow e^+e^-\gamma$), deren relatives Verzweigungsverhältnis bekannt ist, durchgeführt.

Um die Impulsauflösung der Spurrekonstruktion und damit die Auflösung des Experimentes in der invarianten Masse zu verbessern, wurde ein Algorithmus zur simultanen Anpassung der rekonstruierten Teilchenspuren unter Ausnutzung der kinematischen Randbedingungen entwickelt. Die Ergebnisse dieser Untersuchung wurden zur Bestimmung der Rekonstruktionseffizienz des HADES-Experimentes für Di-Elektronen verwendet.

Anhand der kinematischen Daten der elastischen Proton-Proton Streuung wurde die Auflösung der Spurrekonstruktion und die Ausrichtung der Detektoren im Raum untersucht.

Desweiteren wurde eine Methode zur Impulsrekonstruktion der Teilchenspuren entwickelt, die auf der Verwendung eines kubischen Splines als Spurmodell im Bereich des magnetischen Feldes basiert. Die in den Driftkammern des Spektrometers rekonstruierten Teilchenspuren wurden durch eine weitere, im Rahmen dieser Arbeit entwickelte, Methode mit den Spurpunkten der Spuren in den Flugzeitwänden korreliert. Beide Methoden wurden für die Analyse in der vorliegenden Arbeit verwendet.

Aufgrund der unterschiedlichen Phasenraumverteilung der obengenannten Zerfallskanäle ist die Akzeptanz des HADES-Spektrometers fuer die Zerfallsprodukte aus beiden Kanälen ebenfalls verschieden. Daher wurde durch eine Simulation das relative Verzweigungsverhältnis innerhalb der Akzeptanz des HADES-Spektrometers bestimmt. Es wurden verschiedene anisotrope Winkelverteilung des η -Mesons, wie sie vom DISTO-Experiment beobachtet wurden, simuliert und mit den gemessenen Daten verglichen.

Im Vektordominanzmodell wechselwirkt das Photon mit einem Hadron nicht nur direkt, sondern auch durch Vektormesonen. Insbesondere für das neutrale pseudoskalare η -Meson erfolgt der Dalitz-Zerfall in zwei Schritten: Zuerst werden zwei Photonen (reell und virtuell) emittiert, danach zerfällt das virtuelle Photon in ein e^+e^- Paar.

Die Gültigkeit der Beschreibung des Dalitz-Zerfalls des η - Mesons durch das VDM wurde durch einen Vergleich mit der experimentell rekonstruierten invarianten Massenverteilung der e^+e^- Paare geprüft.

Der Produktionsmechanismus des η -Mesons wurde anhand der Winkelverteilung der Mesonen im Schwerpunktsystem untersucht.

Die vorliegende Arbeit unterteilt sich in zwei Teile:

Der erste Teil gibt eine kurze Beschreibung des Physik Programs des HADES-Experimentes, eine Beschreibung des Spektrometers und eine detaillierte Darstellung der Spurrekonstruktionsalgorithmen.

Der zweite Teil der Arbeit befasst sich mit der Analyse der Proton-Proton-Daten und den obengenannten Untersuchungen, sowie der Diskussion der Resultate.

Abstract

HADES (**H**igh **A**cceptance **D**i**E**lectron **S**pectrometer) is a unique apparatus currently assembled at heavy-ion synchrotron SIS at GSI, Darmstadt.

The main part of the HADES physics program is focused on in-medium properties of the light vector mesons $\rho(770)$, $\omega(783)$ and $\phi(1020)$, but also concerns several important problems of hadron physics like: validity of the **V**ector meson **D**ominance **M**odel (VDM) in the description of meson and baryon Dalitz decays and of the electromagnetic form-factor of the nucleon in time-like region.

In the framework of the present thesis a detailed study of the exclusive η meson reconstruction in proton-proton collisions at 2.2 GeV kinetic energy of the incident proton beam is presented. The exclusive measurement of the η mesons has been performed for two electromagnetic decay channels ($\eta \rightarrow \pi^+\pi^-\pi^0$ and $\eta \rightarrow e^+e^-\gamma$), the relative branching ratios of which are known.

In order to obtain better tracking resolution, an algorithm of kinematic fit has been developed and tested. The main goal of the kinematic fit is to improve the reconstruction resolution by using physical constraints governing the process. Studied results have been used to evaluate the dielectron detection efficiency of the HADES experiment. The kinematic fit algorithm has been used for above mentioned analysis as well.

Apart from these studies, using the kinematics of the elastic scattering channel, the spectrometer performance has been studied in terms of reconstruction resolution and detector alignments.

From a technical point of view, a new method for momentum reconstruction, using a cubic spline track model in the magnetic field region of the HADES spectrometer, has been developed. An algorithm for matching of different hits belonging to one track reconstructed by the spectrometer systems has also been developed. Both algorithms have been used for the data analysis described in this work.

The phase-space distributions of $\eta \rightarrow \pi^+\pi^-\pi^0$ and $\eta \rightarrow e^+e^-\gamma$ decay channels being different, the relative branching ratio of these decay channels will differ from that obtained for full phase space. Therefore the simulation data has been generated in order to find out the relative branching ratios of the above mentioned decay channels inside the HADES acceptance. We have done different types of simulations in order to compare with the data. In particular, the anisotropy in the angular distributions of the η mesons, observed by the DISTO experiment, have been included in the simulation and compared with our data.

According to the VDM, the photon interacts with the hadron of interest not only directly, but also through vector mesons. In particular for the η meson, which is a neutral pseudoscalar meson, the Dalitz decay goes in two steps, where in a first step it emits two photons (real plus virtual), and in a second step the virtual photon decays into a e^+e^- pair.

The validity of the VDM model in describing the Dalitz decay of the η meson has been investigated by comparing the experimentally reconstructed invariant-mass distribution of the e^+e^- pairs with the VDM model predictions.

To investigate the production mechanism of the η meson, their angular distributions in the center-of-mass system have been studied.

This thesis is divided into two parts:

In the first part a brief introduction to the physics program of the HADES experiment is given. A description of the detector systems of the spectrometer and the detailed explanation of track reconstruction algorithm of the HADES experiment is given in this part as well.

The second part mainly concerns the analysis of the proton-proton data and the discussion of the results.

Contents

Contents	i
List of Figures	v
List of Tables	xi
I Physics motivation, spectrometer setup and tracking	1
1 Physics motivation	3
1.1 Vector meson Dominance Model	3
1.2 Dalitz decays of mesons and transition form factors	7
1.3 Previous measurements	9
1.3.1 η meson form factor	9
1.3.2 η meson production	10
1.4 Vector mesons in hadronic matter	11
2 HADES detector system	13
2.1 Start and Veto detectors	15
2.2 Ring Imaging Cherenkov Detector	16
2.2.1 Energy loss of charged particles	18
2.2.2 HADES tracking system	20
2.3 Magnet	22
2.4 Multiplicity Electron Trigger Array (META)	23
2.4.1 TOF and TOFINO detectors	24
2.4.2 Pre-Shower Detector	25
2.5 HADES trigger system	27
3 HADES Tracking	31
3.1 Track parametrization in the HADES experiment	32
3.2 Track reconstruction algorithm	33

3.3	Track finder	34
3.4	Track fitter	38
3.5	Alignment	43
3.6	Matching of hits	44
3.7	Kick plane algorithm	48
3.8	Method of spline	50
3.8.1	Track model assumption	50
3.8.2	Field equations	51
3.8.3	Solution of field equations	53
3.9	Method of Runge Kutta	56
II	Proton-proton data at 2.2GeV	59
4	Elastic scattering channel	65
4.1	Introduction	65
4.2	Results from elastic scattering	66
5	Exclusive η meson reconstruction	75
5.0.1	Introduction	75
5.1	Meson production in NN collisions	78
5.2	Simulation	80
5.2.1	Reaction parametrization	81
5.3	Analysis Strategy	82
5.3.1	Event selection and particle identification	83
5.3.2	Removal of fake tracks	85
5.3.3	Reaction selection	86
5.4	η meson reconstruction	88
5.4.1	Results for the simulation	91
5.4.2	Results for experimental data	93
5.4.3	Kinematic fit	94
5.4.4	Contribution from $\eta \rightarrow \gamma\gamma$	104
5.5	Estimation of the dilepton identification efficiency	106
5.6	η meson production	106
5.7	η meson decay	108
6	Discussion and Outlook	111
6.0.1	Dilepton identification efficiency of the HADES spectrometer	113
6.0.2	η meson production	117
6.0.3	η meson decay	118
6.0.4	Investigation of the spectrometer performance using elastic scattering	121

<i>CONTENTS</i>	iii
A Lorentz transformations	123
B Kinematics of elastic scattering	127
C Formulas for kinematic fit	131
D Data levels	135
E Spline interpolation	137
E.1 Solution of field equations using cubic spline	139
F Software implementation	141
Bibliography	147
Acknowledgments	153

List of Figures

1.1	Interaction of fast electrons with hadrons through one photon, two virtual pions, three virtual pions and so on [1].	4
1.2	Diagrams for the transition form factor of the pseudoscalar meson in the VDM.	8
1.3	Data on the η meson transition form-factor. The points are experimental values [2]. The solid line is the result of fitting the experimental data points with formula 1.21. The dashed curve is the VDM prediction. A point-like η meson would imply that the the data follow the blue dashed line.	9
1.4	Data on the transition form-factor for the $\omega\pi^0$ vertex [2]. The solid line is the fit of the experimental data points with formula 1.22. Curve 3 has been calculated with the VDM.	10
2.1	The HADES spectrometer (a) 3-D view and (b) side view.	13
2.2	The diamond START detector. The VETO detector is identical.	15
2.3	The Ring Imaging Cherenkov detector.	17
2.4	Stopping power ($=\langle -dE/dx \rangle$) for positive muons in copper as a function of $\beta\gamma = p/Mc$	19
2.5	Arrangement of MDC chambers with respect to magnet coils (a) and arrangement of sense wires in different layers of one MDC (b).	20
2.6	Geometry of a drift cell for MDCII. The position of the cathode wires are labeled with +, the sense wires with 0, and the potential wires with x. The yellow area marks the drift cell.	21
2.7	Two dimensional coordinate system of the parametrization of a particle track in GARFIELD. The parametrization of the track is based on the minimum distance to the sense wire and the impact angle of the track to the drift cell.	22
2.8	Contour plots for the main component of the magnetic field at different azimuthal angles.	23
2.9	TOF (a) and TOFINO (b) detectors.	24
2.10	Side view of the Pre-Shower detector.	26
2.11	Hades trigger system.	27

2.12	Event selection scheme used for data acquisition.	28
3.1	Track parametrization (θ, ϕ, ρ, z) in the HADES experiment.	31
3.2	The track viewed along the z axis. The beam is directed perpendicular to Figure plane, along z axis.	32
3.3	Projection of fired wires onto the plane for the combined mode of cluster finding.	35
3.4	Two dimensional (left) and 3 dimensional(right) views of the projected wires	36
3.5	The value of the weight as a function of χ^2	40
3.6	Scaling of the fit parameters in order to speed up the minimization procedure.	42
3.7	3D view of measured MDCI and MDCII points	43
3.8	Matching of track candidates with META hits in case of (a) four MDC chambers and (b) three MDC chambers.	45
3.9	Illustration of the kick plane algorithm.	49
3.10	Positions of the fixed planes with respect to the main component lines of the magnetic field. The picture is obtained for the middle of the sector, $\phi = 90^0$. The radial distance means $\sqrt{X^2 + Y^2}$. Through intersection points of inner and outer segment with the corresponding planes (green crossings) the spline fit has been performed. The red points are selected from spline curve for which the equations of motion are solved.	50
3.11	Momentum resolution as a function of momentum for different resolutions of GEANT hits.	55
3.12	Schematic view of participating detector parts during the run. The parts with full colors correspond to operational detectors (some of them are not fully operational, for details see text), while white boxes show the missing detectors.	61
4.1	Kinematics of elastic scattering in (a) LAB system and (B) center-of-mass system of protons.	65
4.2	The distributions used to select the elastic scattering channel. $3 * \sigma$ cuts around peaks in (a) and (b) have been used.	68
4.3	The distributions showing the quality of elastic channel selection.	69
4.4	Distribution of the absolute value of azimuthal angle differences of protons for each pair of opposite sectors.	70
4.5	Distribution of polar angle products of two protons for each pair of opposite sectors.	71
4.6	The momentum resolution obtained for each sector using elastic scattering for spline(green) and Runge Kutta (red) methods. The resolution is defined as $\frac{\frac{1}{P_{preconstructed}} - \frac{1}{P_{calculated}}}{\frac{1}{P_{calculated}}}$	72

4.7	The momentum resolution as a function of polar angle obtained for each sector using elastic scattering for the Runge Kutta method. The resolution is defined as $\frac{\frac{1}{P_{preconstructed}} - \frac{1}{P_{calculated}}}{P_{calculated}}$	73
5.1	A nonet of pseudoscalar mesons.	76
5.2	Decay channels of the η meson with well known branching ratios studied in this work.	77
5.3	Ground state of a nucleon.	79
5.4	Excited state of a nucleon, via spin flip (a) corresponding to P_{33} and orbital excitation (b) corresponding to S_{11} or D_{13}	79
5.5	Production mechanisms of η mesons in NN collisions a)resonance decay b)hadronic current c)direct decay d)mesonic fusion.	80
5.6	Parameters describing η meson production.	82
5.7	Candidates created from an event in the case of exactly 3 positive and one negative particles (a) for the 3 pion final state (negative particle is assumed to be π^-) and (b) for the Dalitz decay (the negative particle is assumed to be e^-).	83
5.8	Graphical cuts used for particle identification: a) for 3 pion final state and b) for the Dalitz decay of the η meson.	84
5.9	Strategy for removing fake META candidates when (a) one track candidate is matched with two different META hits and (b) two track candidates are matched with the same META hit (See text for details).	85
5.10	Strategy for removing fake track candidates when (a) one inner segment is matched with two outer ones, (b) like in case (a), but tracks have different polarity and (c) two inner segments are matched with one outer segment.	86
5.11	Missing-mass distributions of (a) $pp\pi^+\pi^-$ and (b) ppe^+e^- . Both (a) and (b) are fitted with Gaussian for a signal plus polynomial for background. 3.5σ cut around signal peak is used in order to select the reactions with missing π^0 and missing γ , correspondingly.	87
5.12	Missing mass distribution of $pp\pi^+\pi^-$ as a function of missing mass distribution of two protons for the experimental data, the η peak is seen in the region where the missing mass of four particles is located near the missing pion mass.	88
5.13	Square of missing mass distribution of ppe^+e^- as a function of missing mass distribution of two protons for the experimental data, the η peak is seen in the region where the missing mass of four particles is located at zero (γ peak).	89
5.14	Multiplicity of η candidates per event left after all applied cuts. Only the events with one η candidate have been kept.	90

5.15	Missing-mass distribution of two protons after selecting the events with missing π^0 ; the distribution is fitted with a Gaussian for the signal plus a polynomial for background.	91
5.16	Missing-mass distribution of two protons after selecting events with missing γ ; the distribution is fitted with a Gaussian for the signal plus a polynomial for background.	92
5.17	Missing-mass distribution of two protons after selecting events with missing π^0 ; the distribution is fitted with a Gaussian for the signal plus a polynomial for background. The yield was calculated by counting the histogram entries above the background due to small structure in the signal.	93
5.18	Missing-mass distribution of two protons after selecting events with missing γ ; the distribution is fitted with a Gaussian for the signal plus a polynomial for background.	94
5.19	Comparison of missing-mass distributions of two protons for simulation before (green) and after (red) the kinematic fit algorithm. (a) after selecting events with missing π^0 in missing mass distributions of $pp\pi^+\pi^-$ and (b) after selecting events with missing γ in missing-mass distributions of ppe^+e^-	96
5.20	Comparison of missing-mass distributions of two protons for experimental data before (green) and after (red) the kinematic fit algorithm. (a) after selecting events with missing π^0 in missing mass distributions of $pp\pi^+\pi^-$ and (b) after selecting events with missing γ in missing-mass distributions of ppe^+e^-	97
5.21	χ^2 distribution of the kinematic fit for 3-pion final state (a) and the Dalitz decay (b) for experimental data. The green distributions correspond to the calculated χ^2 function, while red distributions are obtained from the data.	98
5.22	Pull distributions for inverse momenta of p,p, π^- and π^+	99
5.23	Pull distributions for polar angles of p,p, π^- and π^+	100
5.24	Pull distributions for azimuthal angles of p,p, π^- and π^+	101
5.25	Missing mass distributions of two protons after selecting events with missing π^0 for simulation after the kinematic fit.	102
5.26	Missing mass distributions of two protons after selecting events with missing γ for simulation after the kinematic fit.	102
5.27	Missing-mass distributions of two protons after selecting events with missing π^0 for experimental data after the kinematic fit.	103
5.28	Missing-mass distributions of two protons after selecting events with missing γ for experimental data after the kinematic fit.	104
5.29	Missing-mass distribution of two protons for the Dalitz decay for all pairs (black), when at least one of the dileptons is coming from γ conversion (green) and when both leptons are parent particles (red), before applying the cuts (a) and after applying the cuts (b).	105

5.30	Angular distributions of the η mesons after background subtraction in the center-of-mass system of protons from experimental data (red points) compared with those obtained from simulation (blue line) generated isotropically through the N_{1535}^* resonance. The green line corresponds to the simulation where the anisotropy observed by the DISTO experiment has been included.	107
5.31	Illustration of the background subtraction. The background is estimated as the averaged mean from side bands.	108
5.32	Invariant mass distributions of e^+e^- pairs, from experimental data, after acceptance correction compared with Vector Dominance Model calculations (red) and QED calculations (blue).	109
5.33	Invariant mass distributions of e^+e^- pairs, from simulation, after acceptance correction compared with Vector Dominance Model calculations (red) and QED calculations (blue).	110
6.1	Missing-mass distributions of two protons before applying the kinematic fit algorithm; (a) for experimental data after applying a cut around π^0 peak in the missing-mass distributions of four particles, (b) for experimental data after applying a cut around γ peak in the missing mass distributions of four particles, (c) for simulation corresponding to the 3-pion decay of the η meson, and (d) for simulation corresponding to the Dalitz decay of the η meson.	112
6.2	Missing-mass distributions of two protons after applying the kinematic fit algorithm; (a) for experimental data after applying a cut around π^0 peak in the missing-mass distributions of four particles, (b) for experimental data after applying a cut around γ peak in the missing mass distributions of four particles, (c) for simulation corresponding to the 3-pion decay of the η meson, and (d) for simulation corresponding to the Dalitz decay of the η meson.	115
6.3	Angular distributions of η mesons in the center-of-mass system of the 2 protons. Red points are obtained from data, while blue and green lines are obtained from simulations through N_{1535}^* resonance with isotropic (blue) and anisotropic (green) angular distributions observed by the DISTO experiment.	117
6.4	Invariant-mass distribution of e^+e^- pairs from the Dalitz decay of the η meson for real data (a) and for simulation (b). Red line corresponds to the VDM model calculations, while the blue line represents the pure QED calculations.	120
B.1	Kinematics of elastic scattering in (a) LAB and (b) center of mass system of two protons.	127

D.1	Global time offset determination	136
F.1	Block diagram for track finder and fitter.	143
F.2	Block diagram of matching code.	144

List of Tables

4.1	Momentum resolution from spline and Runge Kutta, obtained for each sector using elastic scattering.	74
4.2	Systematic shifts in momentum reconstruction for spline and Runge Kutta for each sector.	74
5.1	Processes included in cocktail simulation.	81
5.2	Number of events left under corresponding conditions.	90
6.1	Number of reconstructed η mesons before the kinematic fit.	113
6.2	Number of reconstructed η mesons after the kinematic fit.	113

Part I

Physics motivation, spectrometer setup and tracking

Chapter 1

Physics motivation

1.1 Vector meson Dominance Model

One of the physics goals of the HADES experiment is to test the validity of the Vector meson Dominance Model in describing the Dalitz decays of mesons.

The vector mesons ρ, ω, ϕ play a special role in the description of hadronic interactions in the non-perturbative QCD regime. In this regime, effective hadron models use composite hadrons and mesons as field carriers instead of quarks and gluons.

The discrepancy of magnetic moments of protons and neutrons from their Dirac values ($1\mu_b$ and 0 correspondingly) was explained as a possibility for the nucleon to be a composite system of an idealized (bare) nucleon and a π meson cloud. In this schema, a proton is existing part of the time as a bare one with a π^0 cloud and another part as a bare neutron with a π^+ cloud. Qualitative estimation of the π meson cloud radius gives as a result a value of the order of the Compton wave length for pions. Thus the above schema predicts that the electric charge inside a proton is not concentrated at a point but spread in a finite volume.

Taking into account this interpretation, the interaction of fast electrons with a nucleon can be explained with Feynman diagrams as shown in Figure 1.1. The left part of the Figure expresses the net effect consisting of several parts on the right side [1]:

- One photon
- Two virtual pions from the pion cloud
- Three virtual pions from the pion cloud
- etc.

Theoretical calculations have shown that this picture explains the experimentally obtained data on form factors if one assumes a strong resonant interaction between pions

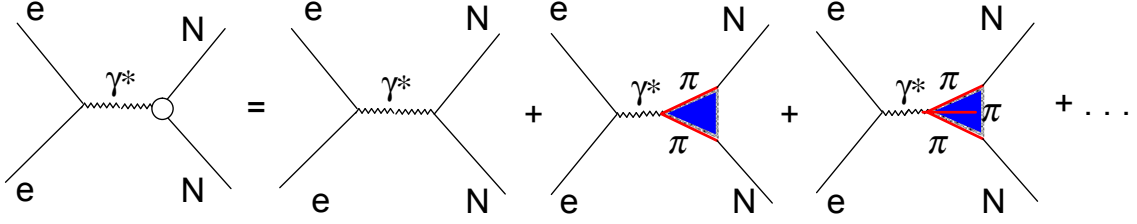


Figure 1.1: Interaction of fast electrons with hadrons through one photon, two virtual pions, three virtual pions and so on [1].

and assumes the systems of two and three pions as new particles: vector mesons [1, 3, 4] (Shaded area in Figure 1.1).

It turns out, that in contrast to the case of space-like momentum transfers where the form factors of charged particles decrease as q^2 increases, another spectacular phenomenon arises in the case of time-like momentum transfers. A virtual photon can interact with a hadron of interest not only directly, but also after a transition to a virtual vector meson state [2]. This is the essential idea behind the **V**ector **m**eson **D**ominance **M**odel (VDM).

In the field theory, the particle interactions are described via Lagrangian (L), which depends on field (φ) and its first derivative ($\partial_\mu \varphi$), of interacting currents and fields. There one obtains the equations of motion by requiring the variation of the action $S = \int d^4x L$ to vanish:

$$\frac{\delta S}{\delta \varphi} = 0 \quad (1.1)$$

which leads to the so called Euler-Lagrange equations:

$$\frac{\partial L}{\partial \varphi} - \partial_\mu \frac{\partial L}{\partial (\partial_\mu \varphi)} = 0 \quad (1.2)$$

For example, the Lagrangian for free fermion with mass m can be written as:

$$L = \bar{\psi}(i\gamma^\mu \partial_\mu - m)\psi \quad (1.3)$$

This Lagrangian is not invariant under local gauge transformations:

$$\psi \rightarrow \psi' = e^{iQ\theta(x)}\psi \quad (1.4)$$

because $\partial_\mu \psi$ which enters into 1.3 will transform as:

$$\partial_\mu \psi \rightarrow e^{iQ\theta(x)} (\partial_\mu + iQ\partial_\mu \theta(x)) \psi \quad (1.5)$$

where the term $iQ\partial_\mu\theta(x)\psi$ breaks the symmetry. But we want the Lagrangian to be invariant under the local transformations as well. This can be done by introducing a covariant derivative D_μ which transforms as the field does:

$$D_\mu\psi \rightarrow (D_\mu\psi)' = e^{iQ\theta(x)}D_\mu\psi \quad (1.6)$$

If we manage to build such a covariant derivative the Lagrangian 1.3 will be invariant under the local transformations as well.

Our aim was to eliminate the symmetry breaking term which has a Lorentz index, therefore the covariant derivative should also contain something with Lorentz index, which we will denote as A_μ

$$D_\mu\psi \equiv (\partial_\mu - ieQA_\mu)\psi \quad (1.7)$$

where e is called a coupling constant.

In order for the covariant derivative to transform like 1.6, the introduced field should transform like:

$$A_\mu \rightarrow A_\mu + \frac{1}{e}\partial_\mu\theta(x) \quad (1.8)$$

Now we can write a Lagrangian 1.3 with the covariant derivative

$$L = \bar{\psi}(i\gamma^\mu D_\mu - m)\psi \quad (1.9)$$

which is clearly invariant under local transformations.

Substituting definition of of the covariant derivative from 1.7 into Lagrangian 1.9 we have

$$L = \bar{\psi}(i\gamma^\mu\partial_\mu - m)\psi + eQA_\mu(\bar{\psi}\gamma^\mu\psi) \quad (1.10)$$

By comparing this Lagrangian with the Lagrangian for interacting electron and photon fields one can easily see that the introduced fields A_μ are nothing but the photon field.

We can write the interaction term in the Lagrangian as:

$$L_{int}^{em} = eJ_\mu^{em}A^\mu \quad (1.11)$$

Summarizing, by requiring the local gauge invariance of the Lagrangian for free fermion field we had to introduce a photon field and got the interaction term in the Lagrangian, which describes the interaction of fermions with photon. One can also note that it is automatically obtained that photon should be massless because the Lagrangian 1.10 does not contain a mass term for the photon.

In a similar way in order to preserve the invariance of the free Lagrangian under local SU(2) isotopic transformations:

$$\psi \rightarrow e^{i\frac{\tau_\alpha}{2}\theta_\alpha(x)} \quad (1.12)$$

where τ_α are Pauli matrices, one has to introduce the vector meson fields. The corresponding interaction term can be written as ¹:

$$g\rho_\mu^\alpha \bar{\psi}\gamma^\mu(\tau_\alpha/2)\psi \quad (1.13)$$

where g is the corresponding coupling constant and ρ_μ is the vector meson field. Similar to 1.11 we can write an interaction term in Lagrangian as:

$$L_{int}^h = gj_\mu^\alpha \rho_\alpha^\mu \quad (1.14)$$

where \vec{j}_μ is the hadronic vector current and $\vec{\rho}^\mu$ is the vector meson field.

In other words the requirement of the invariance of the free Lagrangian under local isotopic rotations gives an interactions term in the Lagrangian with vector mesons. As the vector mesons and a photon has the same quantum numbers a virtual photon can interact with a hadron after a transition to a virtual vector meson state.

The coupling constants (g_v) of the vector mesons into photons can be obtained from the measured dielectron decay widths of the vector mesons. For any vector meson V with a mass m_v , neglecting the electron mass, the decay width into e^+e^- pairs can be written as [3]:

$$\Gamma(V \rightarrow e^+e^-) = \frac{4\pi\alpha^2}{3g_v^2} m_v \quad (1.15)$$

According to Equation 1.15 the ratios of $\Gamma_V^{e^+e^-}$ for the ρ , ω and ϕ mesons are proportional to m_v/g_v^2 . The coupling constants g_v can be expressed with a help of one universal coupling constant g_γ :

$$\Gamma_\rho^{e^+e^-} : \Gamma_\omega^{e^+e^-} : \Gamma_\phi^{e^+e^-} = \frac{m_\rho}{g_\gamma^2} : \frac{m_\omega}{9g_\gamma^2} : \frac{m_\phi}{4.5g_\gamma^2} \approx 1 : 9 : 4.5 \quad (1.16)$$

for $g_\gamma = 5.7 \approx g_\rho$.

VDM hypothesis also assumes that the same coupling $g = g_\gamma$ describes also the meson-hadron interactions (See Equation 1.14). This can be verified by an analysis of the di-pion decay width of ρ meson. The corresponding width is given by [5]

$$\Gamma(\rho \rightarrow \pi^+\pi^-) = \frac{2}{3} \frac{|p_{cm}|^3}{m_\rho^2} \frac{f_{\rho\pi\pi}^4}{4\pi} \quad (1.17)$$

¹Here we show an example for the case when the ψ field is an iso-doublet. In general the covariant derivative introduced in this case has a form $\partial_\mu\psi \rightarrow \partial_\mu\psi - ig\vec{\rho}_\mu\vec{T}\psi$. In our example when ψ field is an iso-doublet the matrix \vec{T} is $\vec{\tau}/2$.

where $|p_{cm}| = \sqrt{(m_\rho/2)^2 - m_\pi^2}$

Taking the experimental value of $\Gamma(\rho \rightarrow \pi^+\pi^-)$ one can obtain $f_\rho\pi\pi = 6.05$ which is close to the universal coupling constant $g_\gamma = 5.7$.

1.2 Dalitz decays of mesons and transition form factors

The process of single-photon exchange described in the previous section is forbidden for neutral mesons A (e.g., π^0, η, η'). Indeed, the neutral particle being identical to its antiparticle, it transforms into itself under charge conjugation. Consequently, the wave function of a neutral particle either remains unaffected by charge conjugation or only reverses its sign. Electromagnetic forces are responsible for the decay of π^0, η and η' mesons into two γ quanta. Therefore the charge conjugation parity of such neutral particles is a positive quantity. As the photon, being the quantum of the electromagnetic field, has a negative charge-conjugation parity the one photon exchange breaks the conservation of the charge conjugation parity.

However, a neutral particle with a given charge-conjugation parity can convert as a result of the interaction into another particle with the sign-reversed value of this quantum number. Therefore decays of the type $A \rightarrow Be^+e^-$ are not real multi body decays (for which usually the name Dalitz is used) but can be reduced to a decay into B plus a virtual photon (with an invariant mass $m_{e^+e^-}^2$) and subsequent conversion of the latter [6].

The probability of formation of a lepton pair with an effective mass m_{l+l^-} in a conversion decay, $A \rightarrow B + l^+ + l^-$, is proportional to the probability of emitting a virtual γ quantum with time-like 4-momentum $q^2 = m_{l+l^-}^2$. However, the probability of emission of this photon is determined by the dynamic structure arising at the vertex of the transition. This structure which is due to the cloud of virtual states in the region of the transition $A \rightarrow B$ is characterized by a transition form factor.

The transition form factor can be obtained by studying the probability of the decay $A \rightarrow B + l^+ + l^-$ as a function of the squared effective mass of the lepton pair, $q^2 = m_{l+l^-}^2$. Referred to a unit interval of q^2 , this probability gives so-called spectrum of effective mass of lepton pairs, $d\Gamma/dq^2$.

If the particles A and B were structureless objects, it would be possible to calculate the mass spectrum of leptonic pairs, $[d\Gamma/dq^2]_{pointlike}$ with high accuracy, by the methods of quantum electrodynamics. The complicated internal structure of particles modifies this spectrum:

$$d\Gamma/dq^2 = [d\Gamma/dq^2]_{pointlike} |F_{AB}(q^2)|^2 \quad (1.18)$$

By comparing the measured spectrum of lepton pairs with pure QED calculations for point-like particles, it is possible to determine experimentally the transition form factor $|F_{AB}(q^2)|^2$ in the time-like region of momentum transfer.

The decays $P \rightarrow \gamma + l^+ + l^-$ occupy a special place. In this case the transition form factor describes the electromagnetic structure of the vertex $P \rightarrow \gamma$ which incorporates only one hadron, the decaying meson.

The leptonic pair mass spectrum of the decays of type:

$$P \rightarrow e^+e^-\gamma \quad (1.19)$$

normalized to the total probability of radiative transition is defined as [2]:

$$\frac{d\Gamma(P \rightarrow e^+e^-\gamma)}{dq^2\Gamma(P \rightarrow \gamma\gamma)} = \frac{2\alpha}{3\pi} \left[1 - \frac{4m_e^2}{q^2}\right]^{1/2} \left[1 + 2\frac{m_e^2}{q^2}\right] \frac{1}{q^2} \left[1 - \frac{q^2}{m_p^2}\right]^3 |F_p(q^2)|^2 = [QED] \cdot |F_p(q^2)|^2 \quad (1.20)$$

From general considerations the influence of the form factor can either increase the leptonic pair spectrum, as compared with that obtained for point particles, or decrease it. To estimate the order of magnitude and sign of the expected effect, one may use the VDM hypothesis described in the previous section.

In the VDM, the transition form factors in meson conversion decay are described according to the diagrams in Figure 1.2.

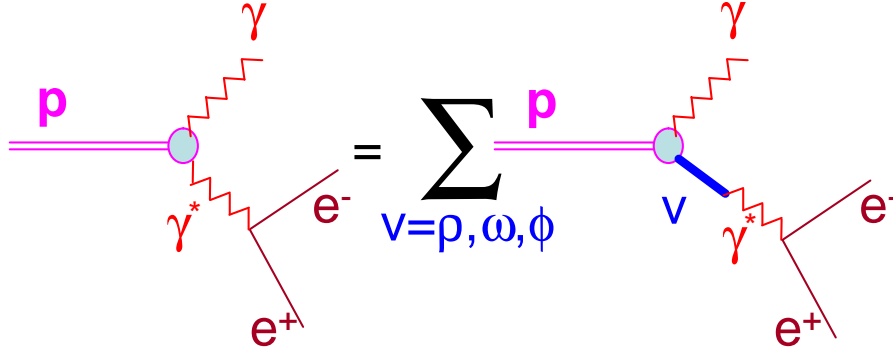


Figure 1.2: Diagrams for the transition form factor of the pseudoscalar meson in the VDM.

In order to test the validity of the VDM model in describing the η meson decay, the reconstructed invariant-mass spectrum of e^+e^- pairs coming from η Dalitz decay ($\eta \rightarrow e^+e^-\gamma$) will be compared with the VDM calculations in this work.

1.3 Previous measurements

1.3.1 η meson form factor

Only two measurements of the η meson form factor has been performed so far. One of them was done for the $\eta \rightarrow \mu^+ \mu^- \gamma$ decay channel which puts a constraint from lower part of the distribution due to the mass of the muon as shown in Figure 1.3[2]. Nevertheless as it is seen from the Figure the VDM model (dashed curve) describes the data quite well in the allowed region. In the Figure the form factor is measured as a ratio of effective mass spectrum of di-muons to the QED calculations (see Equation 1.18). The solid line in the Figure corresponds to the fitting of the experimental data with:

$$F_\eta(q^2) = \left(1 - \frac{q^2}{\Lambda_\eta^2}\right)^{-1} \quad (1.21)$$

where $\Lambda_\eta = 0.72 \pm 0.09 \text{ GeV}$.

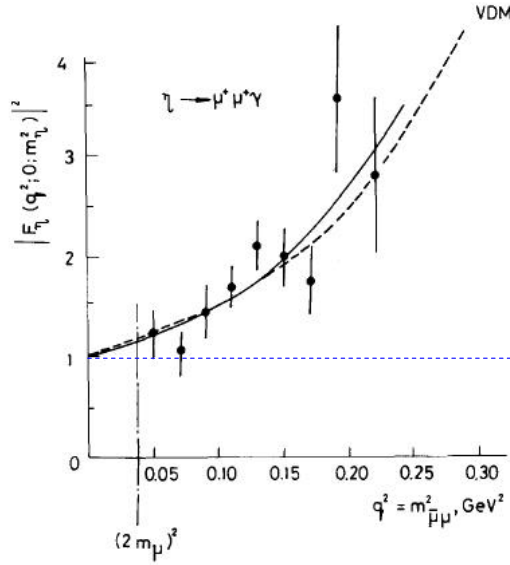


Figure 1.3: Data on the η meson transition form-factor. The points are experimental values [2]. The solid line is the result of fitting the experimental data points with formula 1.21. The dashed curve is the VDM prediction. A point-like η meson would imply that the the data follow the blue dashed line.

The another measurement had been performed for $\eta \rightarrow e^+ e^- \gamma$ with poor statistics (50 counts) [7].

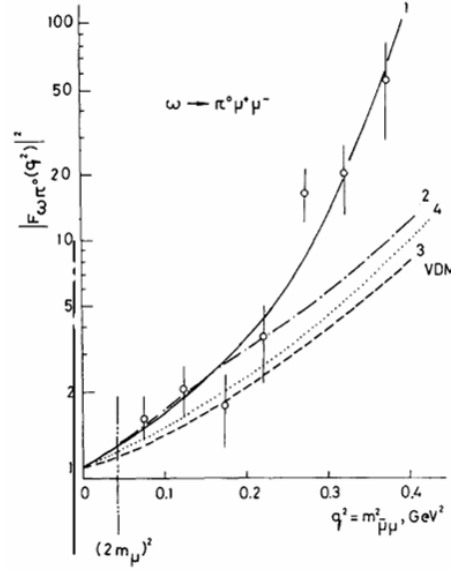


Figure 1.4: Data on the transition form-factor for the $\omega\pi^0$ vertex [2]. The solid line is the fit of the experimental data points with formula 1.22. Curve 3 has been calculated with the VDM.

The VDM model fails to explain the decay of the ω meson. The data obtained for $\omega \rightarrow \pi^0\mu^+\mu^-$ is shown in Figure 1.4 [2]. Line 3 in the Figure corresponds to the VDM model which clearly does not describe the data. Line 1 in the Figure corresponds to the parametrization of the experimental data with:

$$|F_{\omega\pi^0}(q^2)|^2 = \left(1 - \frac{q^2}{\Lambda_\omega^2}\right)^{-2} \quad (1.22)$$

where $\Lambda_\omega = 0.65 \pm 0.03 \text{ GeV}$.

1.3.2 η meson production

At CELSIUS [8], angular distributions of the η emission in the center-of-mass system has been measured in proton-proton collisions at near threshold energies (excess energies $Q = \sqrt{s} - s_0 = 16$ and 37 MeV). It has been shown that the η differential cross section as a function of the η polar angle in center-of-mass frame is not isotropic and shows a maximum of emitted η mesons perpendicular to the beam direction.

The angular distribution measurement at COSY [9] at similar excess energies shows, however, no deviation from isotropy, which is in contradiction to the measurements at CELSIUS.

Exclusive measurement of the η mesons in proton-proton collisions at the beam kinetic energies of 2.15 GeV, 2.50 GeV, and 2.85 GeV had been performed by the DISTO experiment [10]. It was observed that, angular distributions of differential cross section indicates the polar angle anisotropy of the η meson in the center-of-mass system. Furthermore these investigations have shown that the anisotropy gradually vanishes with increasing beam energy.

The anisotropy in angular distributions of the η mesons observed by the DISTO experiment has been included in our simulation [11] and compared with the reconstructed one from experimental data.

1.4 Vector mesons in hadronic matter

Major part of the HADES physics program is focused on in-medium properties of the light vector mesons $\rho(770)$, $\omega(783)$ and $\phi(1020)$. The in-medium properties of the vector mesons in hot and dense matter play an important role in the low-mass dilepton production resulting from heavy-ion collision experiments. This has, hence, been a topic of great interest in recent past, both experimentally [12, 13, 14, 15, 16] and theoretically [17, 18, 19, 20, 21].

Such investigations can be done by studying the proton-nucleus, pion-nucleus and heavy-ion collisions.

In particular, the short-lived ρ meson is an ideal candidate for such studies. The mean life time of the ρ meson, $c\tau \approx 1.5 fm$, is shorter than the fireball lifetime, thus allowing to explore decays inside the hot and/or dense nuclear matter. In-medium modifications of the ρ properties should be reflected in dielectron invariant mass distribution.

Chapter 2

HADES detector system

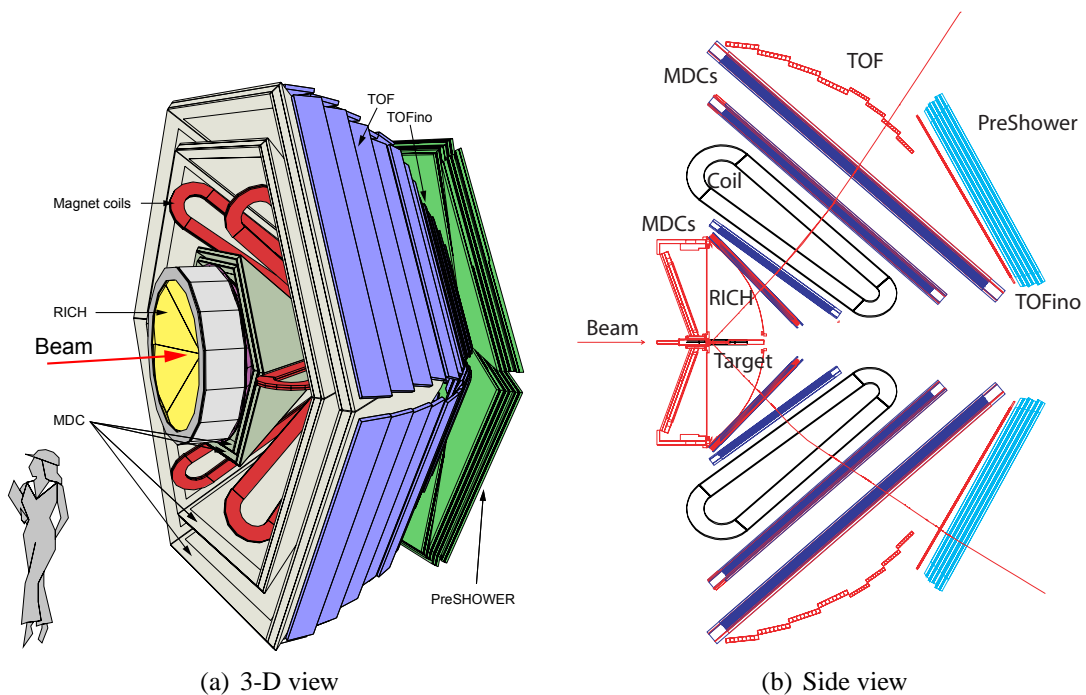


Figure 2.1: The HADES spectrometer (a) 3-D view and (b) side view.

The main goal of detector systems is to deliver several information about a particle:

- energy E (or the momentum p) of the particle at some defined point.
- Identification of the particle, thus defining its mass and charge.
- The coordinates of point on the track together with directions at those points.

Using these information it is possible to calculate a particle's energy at any point of its trajectory, and particularly at the point of interaction.

The main goal of the HADES experiment is to investigate decays of vector mesons via the dilepton decay channel. These decay channels of the vector mesons are suppressed by a factor of $\approx 10^{-5}$ as compared to the hadronic decays. In order to accumulate significant statistics in a reasonable time, the HADES spectrometer design should meet several conditions [22]:

- Large geometrical acceptance in order to maximize the probability of detecting a pair once it is produced.
- High rate capabilities allowing for an operation at beam intensities of up to 10^8 particles/s.
- The high interaction rate together with high hadron multiplicity resulting from the large acceptance represents a serious challenge to the trigger system which has to filter out events containing lepton tracks.
- Sufficient granularity on detectors, so that it is possible to deal with high particle multiplicities.
- The pair mass resolution has to be sufficient to detect changes of the in-medium width of the ω and ϕ mesons. The pair mass resolution should therefore be comparable to the natural width of these states which is about 1%. This requirement subsequently sets conditions on single trajectory momentum resolution as well as on the determination of position which is used for the reconstruction of the momentum of the particles and the pair opening angle. Therefore a magnetic spectrometer is needed with high position resolution before and after the magnetic field.

The HADES spectrometer is a rotationally symmetric, large acceptance toroidal spectrometer with a complete azimuthal coverage [22, 23, 24]. The spectrometer acceptance in polar angles covers the $18^\circ - 85^\circ$ range. The achieved geometrical acceptance of $\sim 40\%$ represents an improvement by a factor of 100 as compared to the pioneering experiments performed with the DLS spectrometer at Berkeley [13].

The HADES detector system consists of the following sets of detectors:

- Start and Veto detectors
- Ring Imaging Cherenkov detector (RICH)
- Magnet
- Multi wire Drift Chambers (MDC)

- Time Of Flight detectors (TOF) and (TOFINO)
- Pre-Shower detectors (SHOWER)

2.1 Start and Veto detectors

The START and VETO diamond detectors are two identical octagonal shaped diamonds synthesized using the Chemical Vapor Deposition (CVD) technique [25]. The thickness of the detector is $100\mu\text{m}$ to minimize multiple scattering. The START detector, as well as the VETO, both have dimensions of $25\text{mm}\times 15\text{mm}$, and placed 75cm upstream and downstream of the target position, are segmented into 8 strips and work in anti-coincidence, such that when a beam particle crosses without interacting with the target it provides a signal in the VETO detector as well and the corresponding event is vetoed. The width of the strips is optimized to guarantee 96.5% VETO efficiency. The START and VETO detectors are used to give a start to the time measurements.

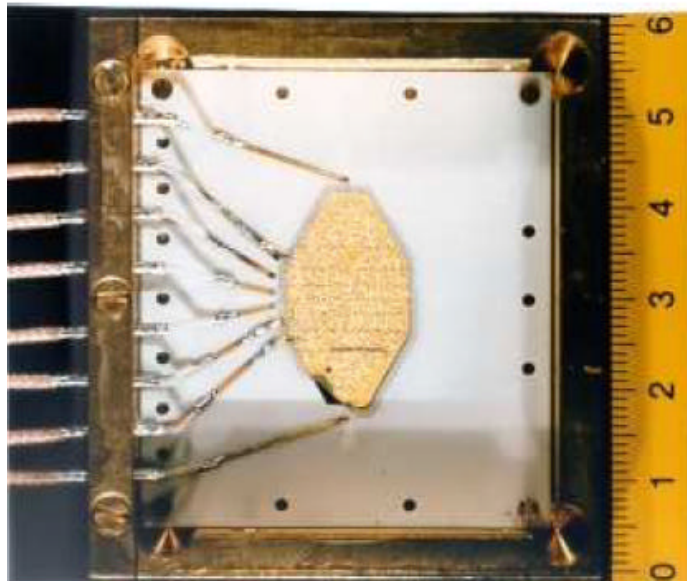


Figure 2.2: The diamond START detector. The VETO detector is identical.

The diamond detectors were not used for proton beams, because the energy loss inside the START material is so small that it does not produce a useful signal. Therefore for the proton beams a pair of scintillating hodoscopes were tested in a commissioning run.

Due to the large number of secondaries produced in proton interaction with the detectors it was decided not to use any START detector for the proton production run. The data

acquisition was started by a fastest particle which crossed the TOF/TOFINO walls and produced a signal above threshold. Therefore during this run the TOF/TOFINO system was measuring the difference between particle's time-of-flight and the time-of-flight of the particle which triggered the data acquisition. The start time of the reaction was reconstructed using an algorithm based on assigning a theoretically calculated time of flight to the identified particle¹. The difference between a theoretically calculated value of time-of-flight (t_{th}) and the experimental one (t_{exp}) allows one to calculate the start time of the reaction (t_0)

$$t_0 = t_{th} - t_{exp} \quad (2.1)$$

The reconstructed start time in this way should be added to the measured time of the other particles inside the same event to obtain the corrected time-of-flight. This procedure is performed on event-by-event basis.

2.2 Ring Imaging Cherenkov Detector

In 1934 P. A. Cherenkov observed a new radiation with the following properties [26, 27]:

- The polarization of the radiation changes under influence of a magnetic field. This means the radiation is induced by charged particles.
- The radiation intensity is independent of the medium charge Z that is why it cannot be of radiative origin
- The radiation is emitted along certain direction.

This radiation later on was explained by I.E. Tamm and I.M. Frank within classic electrodynamics [28]. According to classical electrodynamics a uniformly moving charged particle in a vacuum cannot lose its energy due to radiation, but one can easily deduce based on the energy-momentum conservation laws that this can happen when particle moves through a medium if its velocity is greater than the phase velocity of light in the medium.

The emission of Cherenkov radiation is based on coherent radiation of dipoles created in a medium by the field of the passing particle. When a particle traverses with a relatively small speed it polarizes the medium around it in a symmetric way that is why the net radiation from all dipoles will cancel each other.

¹The negative particle was assumed to be an electron if there was a matching with the signal from the RICH detector or a negative pion in the other case.

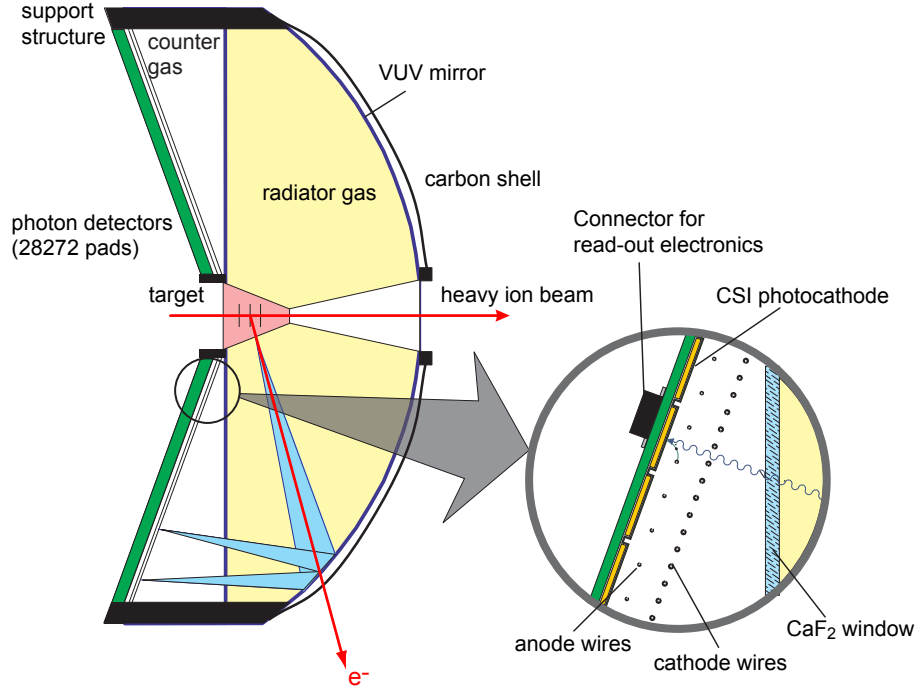


Figure 2.3: The Ring Imaging Cherenkov detector.

On the other hand in case of high speed particle there will be so called polarization delay effect of the medium resulting in polarization mainly in the direction of particle motion. In this case there can be coherent radiation of created dipoles in some direction. The coherent wave front formed is conical and is emitted at an angle

$$\cos \theta = \frac{1}{\beta n} \quad (2.2)$$

with respect to the trajectory of the particle.

This physics is used in the HADES **R**ing **I**maging **C**herenkov **D**etector (RICH) for lepton identification. The particle is identified if $\beta \geq 1/n$, therefore

$$\gamma \geq \sqrt{\frac{n^2}{n^2 - 1}} \quad (2.3)$$

The RICH is the main component of the HADES spectrometer for a lepton identification [29, 30]. It consists of a C_4F_{10} gaseous radiator surrounding the target located roughly in the focal point $f=R/2$ of a spherical mirror with radius of $R=87.1$ cm and a position sensitive Photon Detector (See Figure 2.3). The radiator gas has an index of refraction

$n=1.00151$, which corresponds, according to Equation 2.3, to a threshold of $\gamma_{thr} \approx 18.3$ and guarantees the hadron blindness of the detector. Indeed, the threshold energies to emit a Cherenkov light in such a medium are therefore 15.9 GeV for protons, 2.4 GeV for pions, far above the SIS energies, while for electrons it is 8.5 MeV which is well below the range of interest.

Electrons with velocities $\beta \approx 1$ radiate a Cherenkov light in a cone along their tracks through the radiator. The light is reflected by the aluminized carbon fiber mirror and is focused as an elliptical image on the position sensitive Photon Detector, which is separated by a 5 mm CaF_2 window from the radiator volume. The Photon Detector is composed of Multi Wire Proportional Chambers with a segmented photocathode. When Cherenkov photons reach the photocathode, electrons are emitted by photoelectric effect, induce an electric charge on the photocathode, in one (or more neighboring) pads it is segmented into.

2.2.1 Energy loss of charged particles

Charged particles other than electrons lose energy in matter primarily by ionization and atomic excitation. The mean rate of energy loss (or stopping power) is given by the Bethe-Bloch equation,

$$-\frac{dE}{dx} = Kz^2 \frac{Z}{A} \frac{1}{\beta^2} \left[\frac{1}{2} \ln \frac{2m_e c^2 \beta^2 \gamma^2 T_{max}}{I^2} - \beta^2 - \frac{\delta}{2} \right] \quad (2.4)$$

with $K/A=4\pi N_A r_e^2 m_e c^2 / A=0.307075 \text{ MeV g}^{-1} \text{ cm}^2$ for $A=1 \text{ g mol}^{-1}$

- r_e : classical electron radius= $2.817 \times 10^{-13} \text{ cm}$
- N_A : Avogadro's number= $6.022 \times 10^{23} \text{ mol}^{-1}$
- m_e : electron mass
- I : mean excitation potential
- Z : atomic number of absorbing material
- A : atomic weight of absorbing material
- z : charge of incident particle in units of e
- β = v/c of the incident particle
- γ = $1/\sqrt{1-\beta^2}$
- δ : density correction
- T_{max} : maximum energy transfer in a single collision

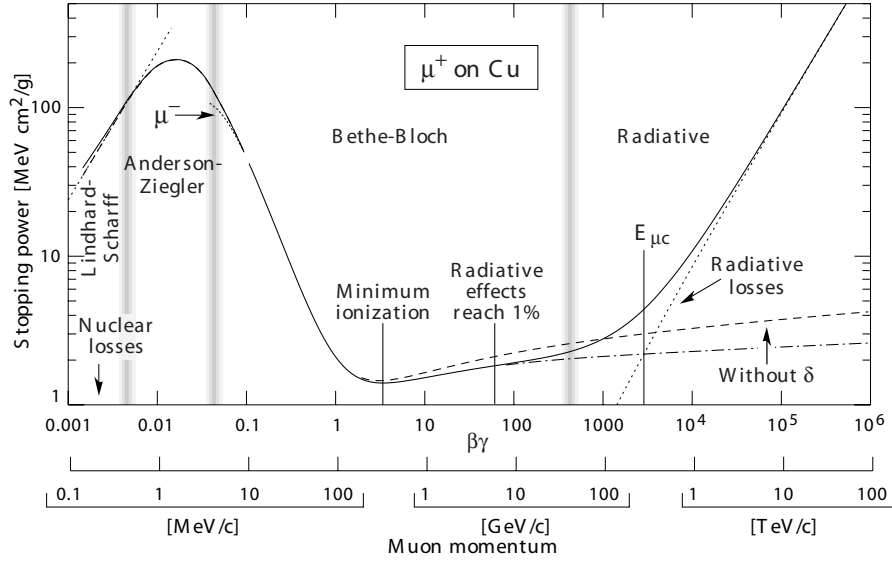


Figure 2.4: Stopping power ($= \langle -dE/dx \rangle$) for positive muons in copper as a function of $\beta\gamma = p/Mc$.

An example of the energy dependence of dE/dx is shown in Figure 2.4 [31] for muons on copper. As $\beta\gamma$ is increased dE/dx falls at first with $1/\beta^2$ factor, then goes through a minimum. Particles at this point are known as minimum ionizing. The minimum value of dE/dx is almost the same for all particles of the same charge. As the $\beta\gamma$ increases beyond this point, the term $1/\beta^2$ becomes almost constant and dE/dx rises again due to the logarithmic terms in 2.4, describing a relativistic rise. It was discovered later that the relativistic rise would not continue infinitely due to the "density effect", calculated by Fermi. A corresponding correction term δ is introduced into Equation 2.4 [28, 32].

Ionization detectors were the first electrical devices developed for radiation detection. These instruments are based on the direct collection of the ionization electrons and ions produced in a gas by passing radiation.

Because of the greater mobility of electrons and ions, a gas is the obvious medium to use for the collection of ionization from radiation.

We distinguish between primary and secondary ionization. The electrons and ions created by the incident radiation itself are known as a primary ionization. In primary ionization, one or sometimes two or more electrons are ejected from the atom X encountered by a fast particle p,



Most of the charge along a track is from secondary ionization where the electrons are

ejected from atoms not encountered by the passing particle. This happens either in collisions of ionization electrons with atoms, or through intermediate excited states X^* .

Multiplication in gas detectors occurs when the primary ionization electrons gain sufficient energy from the accelerating electric field to also ionize gas molecules. The resulting secondary electrons then produce an ionization and so on. This results in the formation of an avalanche. The pulse signal is created on the electrodes due to the movement of the ions and electrons as they drift towards the cathode and anode. Spatial information can be obtained by measuring the drift time of the electrons coming from an ionizing effect.

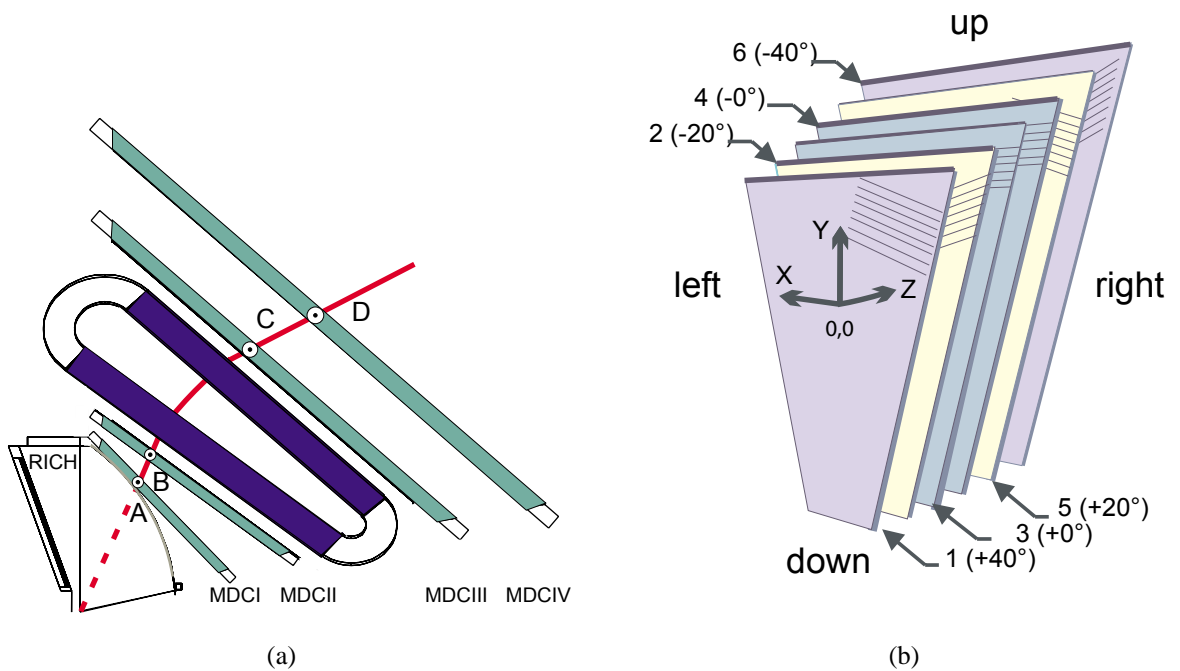


Figure 2.5: Arrangement of MDC chambers with respect to magnet coils (a) and arrangement of sense wires in different layers of one MDC (b).

2.2.2 HADES tracking system

The physics described in the previous section makes the basics of operation of a Multi wire Drift Chambers (MDC), the main tracking part of the HADES experiment [32].

There are in total 24 MDCs, of trapezoidal shape, symmetrically arranged in six identical sectors. They provide a polar angle coverage between 18° and 85° around the beam axis, forming four tracking planes (I-IV) of increasing size. In each sector, two chambers (plane I and II) are located in front of, and two (plane III and IV) behind, the toroidal magnetic field of the super-conducting magnet, as shown in Figure 2.5(a). To cope with

ambiguities (left right ambiguity) in track reconstruction in the high multiplicity environment of a heavy ion reaction, all chambers are composed of six sense/field wire layers oriented in five different stereo angles and seven layers of cathode wires. The cathode wires are oriented perpendicular to the top and bottom frames of the MDCs [33, 34].

This arrangement of wire layers allows for maximum spatial resolution in polar directions, which points in the direction of the momentum kick. From geometrical point of view the two potential wires, the sense wire being in between, together with the cathode wires form a drift cell. The field and cathode wires are made of bare aluminium, with diameters of $100\ \mu\text{m}$ and $80\ \mu\text{m}$ respectively. The sense wires are made of gold plated tungsten with a diameter of $20\ \mu\text{m}$. All four chamber types contain about 1100 drift cells each, with increasing size, from $5\times 5\ \text{mm}^2$ (plane I) to $14\times 10\ \text{mm}^2$ (plane IV), to maintain the granularity per solid angle.

A particle passing the drift cell ionizes the counting gas. The ionization is statistically distributed along the track, initiates separate clusters of electron clouds drifting towards the sense wire and triggers the signal picked up by a fast amplifier connected to the wire. This signal gives the start of the time measurement. The stop is deduced from an external detector e.g. delayed trigger of the start detector. The resulting arrival time of the electrons, after time offset subtraction and calibration of the TDC slope is converted into a distance from sense wire to the point of closest approach of the trajectory.

In the HADES experiment the drift cells are modeled in a two dimensional representation. In the model the cathode wires are parallel to the sense and potential wires. The model of the drift cell is shown in Figure 2.6. The drift cells are investigated using the simulation program GARFIELD [35], which is capable of electric and magnetic field computations of two dimensional geometries.

Using GARFIELD simulations, to each position of the track in space in terms of impact angle to the cell and closest distance to the sense wire of the cell the calculated value of the drift time and its error is assigned (xt relation) (See Figure 2.7).

In order to achieve a mass resolution better than 1% in ρ/ω mass region the drift cells have to provide a position resolution of better than 140 micron. Therefore, both the in-

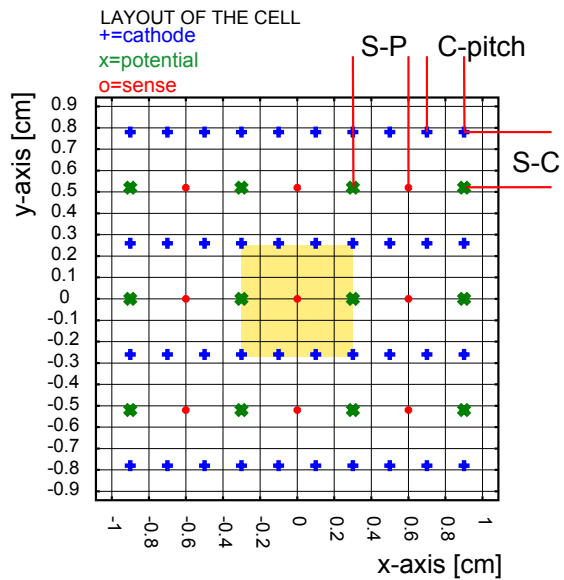


Figure 2.6: Geometry of a drift cell for MD-CII. The position of the cathode wires are labeled with +, the sense wires with o, and the potential wires with x. The yellow area marks the drift cell.

intrinsic position resolution of the drift chambers as well as the multiple scattering along the spectrometer play a key role. Multiple scattering is dominant at low ($< 0.4\text{GeV}/c^2$) dilepton invariant mass. The use of the Helium as the main counter gas is mandatory to keep the contribution of the multiple scattering at tolerable level, because its radiation length is almost 50 times longer than that of Argon. The lack of total primary ionization of Helium is usually compensated by using iso-butane as quencher. Several small and one full size prototypes of MDCs have been built and tested for different concentrations of iso-butane in Helium. From these investigations it was concluded that the mixture containing 40% iso-butane is the optimal choice for application, because it provides enough primary ionization statistics under stable operation at moderate gains [36].

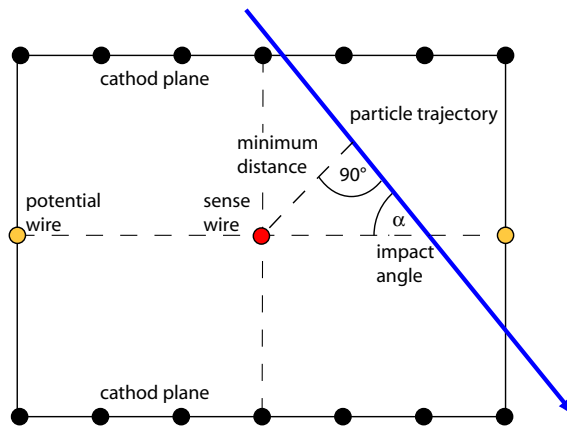


Figure 2.7: Two dimensional coordinate system of the parametrization of a particle track in GARFIELD. The parametrization of the track is based on the minimum distance to the sense wire and the impact angle of the track to the drift cell.

2.3 Magnet

The magnetic field should fulfill several requirements:

- It must deflect charged particles such that their momenta can be obtained with sufficient resolution.
- There should be nearly field free region in the RICH detector.
- Large momentum range must be accepted simultaneously within a large solid angle.

The HADES magnet consists of six super-conducting coils surrounding the beam axis producing the toroidal field. Each coil consists of a straight entrance and exit section

connected by two arcs. The angles of the entrance and exit sections of 40° and 45° with respect to the beam line were chosen to minimize the azimuthal deflection of particles over the whole polar angular range from 18° to 85° .

Figure 2.8 shows contour plots of the main magnetic field component at azimuthal angles of $\phi = 90^\circ$, $\phi = 75^\circ$ and $\phi = 60^\circ$. The maximum field of 3.7T is obtained at the coil surface inside the forward arc. In between the coils, i.e., at the azimuthal angle of 90° , the field extends over a wider region as compared to the azimuthal angle of 60° which is close to the coil.

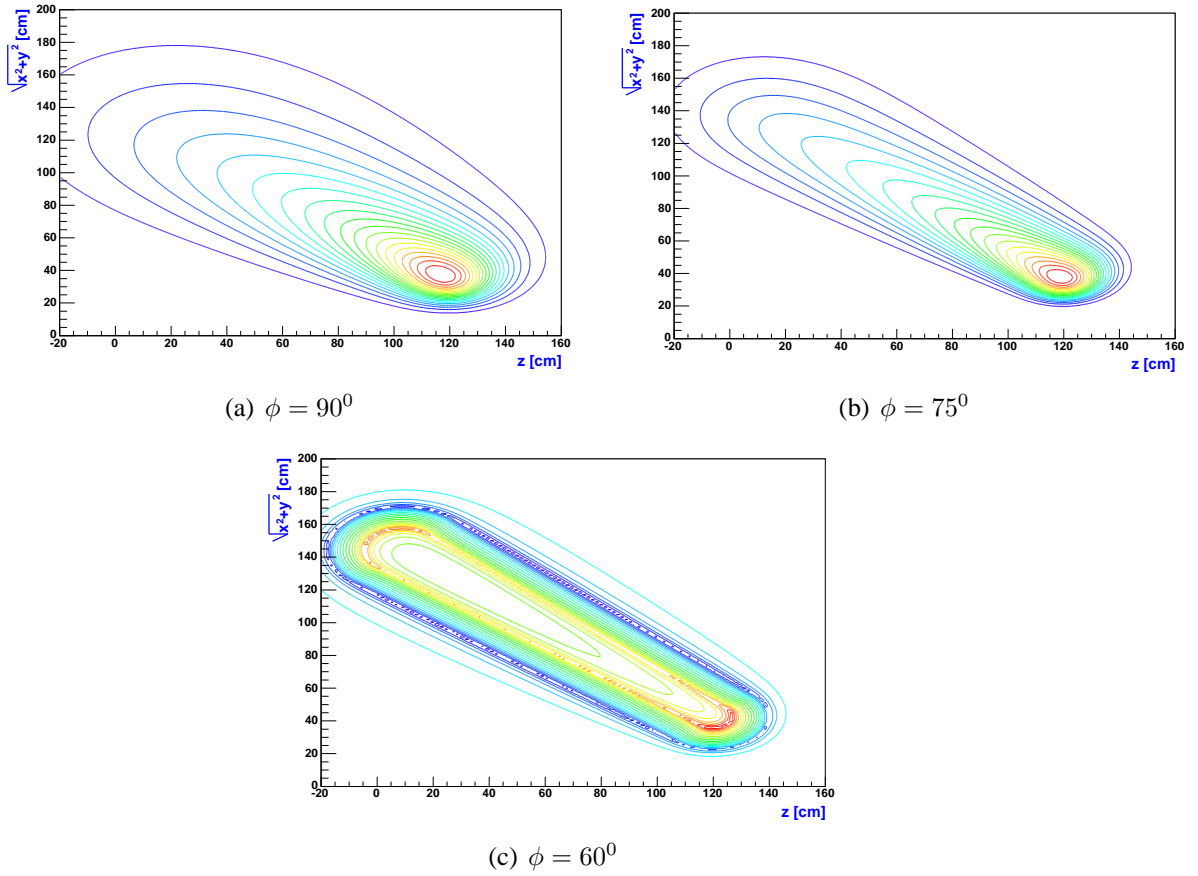


Figure 2.8: Contour plots for the main component of the magnetic field at different azimuthal angles.

2.4 Multiplicity Electron Trigger Array (META)

The META is positioned behind the outer MDCs and is used for particle identification by measuring the time between start detector signal and arrival time. It is used for triggering

purpose as well. The META consists of two Time of Flight systems, an outer TOF and inner TOFINO, covering the full HADES acceptance and the Pre-Shower gas chambers at forward polar angles $\theta < 45^\circ$.

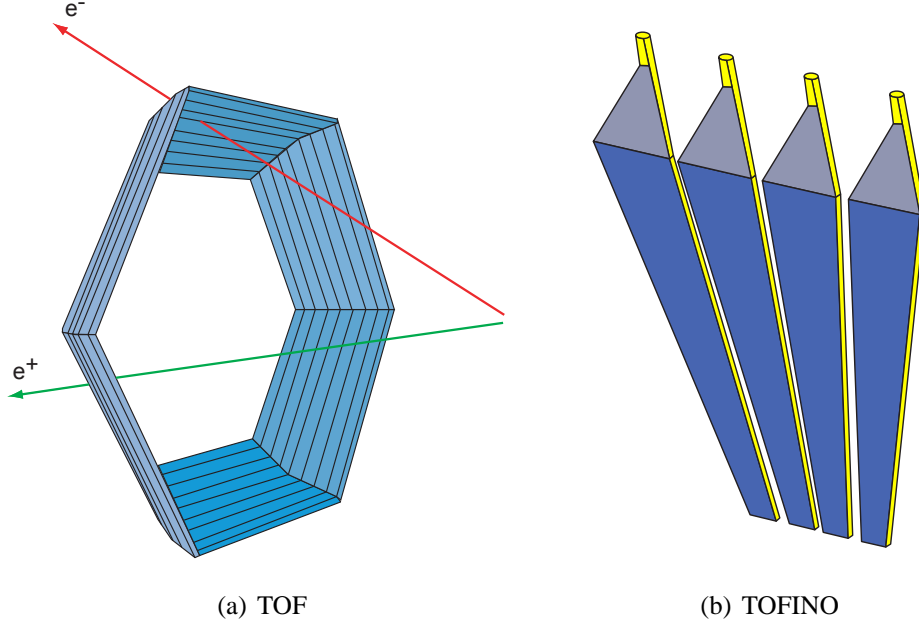


Figure 2.9: TOF (a) and TOFINO (b) detectors.

2.4.1 TOF and TOFINO detectors

Certain materials when struck by a nuclear particle or radiation, emit a small flash of light, i.e. a scintillation. The scintillator detector is undoubtedly one of the most often and widely used particle detection devices in nuclear and particle physics today. The TOF detector follows the hexagonal geometry of the whole spectrometer, and consists of 8 modules per sector each of them being composed of 8 scintillator rods (therefore 64 bars per sector) connected from both sides to photomultiplier tubes [37]. When hit by a particle it provides the light signal which is collected at both ends and then converted to time signal by a TDCs (Time-to-Digital Converter). By combining this information one can extract time-of-flight and hit position of the particle.

If the t_l and t_r are times measured by the left and right TDCs we can write,

$$\begin{aligned}
 t_l(x) &= tof + \frac{1}{v_g} \left(\frac{L}{2} + x \right) \\
 t_r(x) &= tof + \frac{1}{v_g} \left(\frac{L}{2} - x \right)
 \end{aligned}
 \tag{2.6}$$

where t_{of} is the time of flight of the particle, V_g is the group velocity of the light in the scintillator material, L is the length of the rod, and x is the distance between the center of the rod to the point where the particle hits the rod.

From two equations in 2.6 we find:

$$\begin{aligned} t_{of} &= \frac{t_r(x)+t_l(x)}{2} + t_{offset} \\ x &= \frac{t_r-t_l}{2} V_g \end{aligned} \quad (2.7)$$

where

$$t_{offset} = -\frac{L}{2V_g} \quad (2.8)$$

Using time of flight information it is possible to distinguish electrons from protons and pions from protons up to some momentum range.

For time of flight measurements the region of polar angles $\theta < 45^\circ$, is currently covered by a low granularity system called TOFINO. It is divided into six sectors, and each sector is made of four scintillator paddles, arranged radially with respect to the beam axis as shown in Figure 2.9(b). The operation principle of the TOFINO wall is similar to the TOF detector, but in this case the light is collected only at one edge of the scintillator pad. Therefore using only TOFINO information it is not possible to have the position information of the hit. The position information in this case is defined by correlation with the SHOWER detector.

2.4.2 Pre-Shower Detector

Particles passing through matter are scattered and lose energy by collisions. Under these collisions the particles undergo acceleration, hence they emit electromagnetic radiation. The radiation emitted during atomic collisions is customarily called bremsstrahlung (braking radiation) because it was first observed when high energy electrons were stopped in a thick metallic target. For non-relativistic particles the loss of energy by radiation is negligible compared with the collisional energy loss, but for ultra-relativistic particles radiation can be the dominant mode of energy loss. The energy loss is proportional to the square of acceleration. It is clear that Coulomb forces (F) between particles of equal charges (z) and nuclear are the same, hence

$$[(\ddot{x})^2 \sim \frac{1}{m^2}]_{z=const} \quad (2.9)$$

therefore,

$$[(\frac{dE}{dx})_{radiation}]_{z=const} \sim \frac{1}{m^2} \quad (2.10)$$

So, radiative losses for particles of equal charge are inversely proportional to the squared masses; bremsstrahlung therefore plays a particularly important role for light particles.

For each material a critical energy is defined where the average energy loss by ionization and radiation are the same and hence for the electrons above critical value the main mechanism for energy loss is a radiation one.

The combined effects of bremsstrahlung and pair production by an emitted photon produces the so called electromagnetic shower: a high energy electron emits by bremsstrahlung a photon which then by conversion produces an electron- positron pair; electron and positron emits again photons and so on, resulting in a cascade of electrons, positrons and photons.

The HADES Pre-Shower detector uses this effect to distinguish electrons, which develop such a shower, from pions which do not, in the region of small polar angles. Pre-Shower modules are mounted together with four TOFINO paddles in six azimuthally symmetric sectors. The side view of the Pre-Shower detector is shown in Figure 2.10.

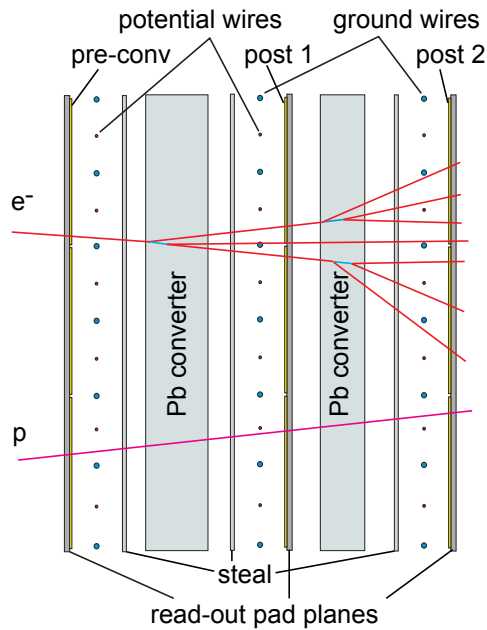


Figure 2.10: Side view of the Pre-Shower detector.

It is composed of a stack of three wire chamber layers (pre-converter, post1-converter, post2-converter) [38]. Each chamber is filled with an argon-isobutan mixture and contains one wire plane and two flat cathodes. In between the planes there is a layer of lead converter with a thickness of almost 1cm. One cathode plane is divided into pads of varying dimensions with an individual signal read-out while the other cathode plane is a flat stainless steel plate. A charged particle passing through the chamber produces an avalanche

of electrons drifting towards the closest anode wire. The avalanche current induces the current of positive polarity on adjacent cathode pads. It is integrated into charge afterwards. The chambers operate in a Self-Quenching Streamer mode which guaranties that the collected charge depends only weakly on the particle specific energy loss [39]. The integrated charge is proportional to the number of particles which enter the chamber. The electromagnetic shower recognition algorithm is based on direct comparison of the integrated charges on corresponding areas of the pre-converter and the post1/post2-converter planes. The integration area has been limited to 3×3 pads.

2.5 HADES trigger system

Since the branching ratio for dilepton decays of vector mesons is on the order of $10^{-5} - 10^{-6}$, in order to collect enough statistics an online selection trigger is needed.

The resulting rate of the nuclear reactions which might reach the spectrometer, for the beam intensities of $10^8/s$, is of the order of 10^6 events per second for the target thickness of 1% interaction length. The maximal limit of $10^5/s$ was taken as an upper limit for the trigger design.

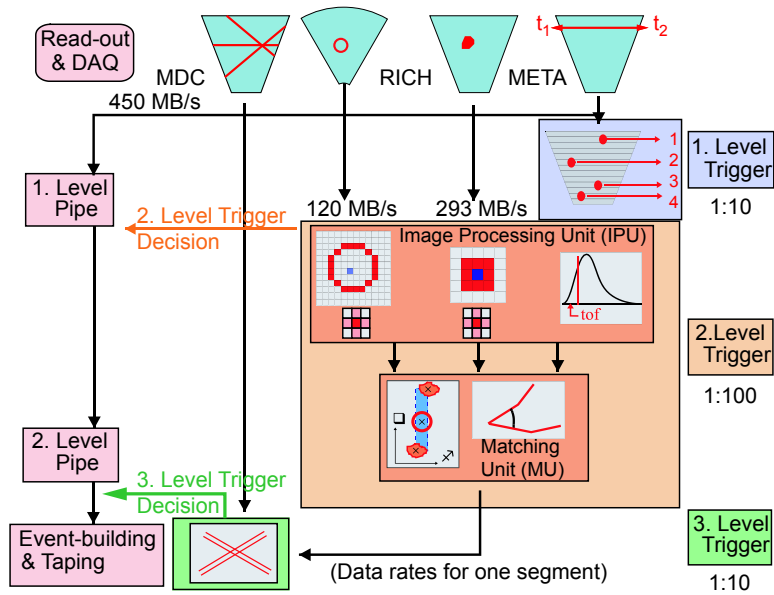


Figure 2.11: Hades trigger system.

The first level trigger (LVL1) selects the most central collisions, based on the multiplicity of charged particles collected in TOF and TOFINO detectors and reduces the event

rate by a factor of 10, down to 10^5 events per second.

The aim of the HADES second level trigger (LVL2) is to perform fast dielectron identification in the RICH and META Image Processor Units (IPU) and to limit data written on tape to events with at least one electron candidates. The LVL2 trigger performs a two step process shown in Figure 2.11. In the first step a search for electrons ring images on the RICH pad plane, charge clusters with the signature of electromagnetic cascade in the Pre-Shower detector and hits with appropriate time of flight in the TOF detectors is done. In the second step a Matching Unit (MU) correlates the position coordinates of electron candidates in RICH and META detectors taking into account the deflection due to the magnetic field [40].

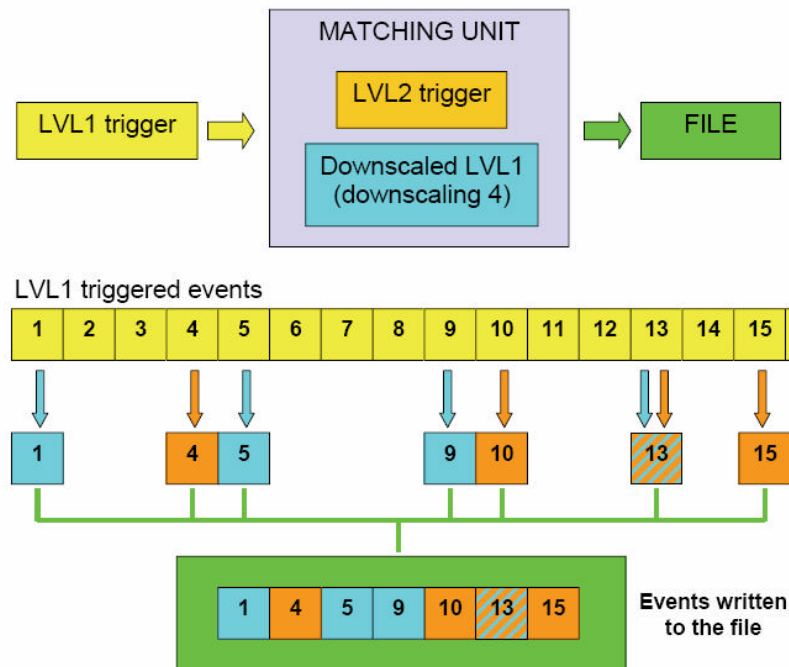


Figure 2.12: Event selection scheme used for data acquisition.

All the events which pass 1st level trigger decision are sent to the matching unit board, which decides whether the event has to be accepted or discarded. This decision is taken separately by two different systems which operate independently: the downscaling box and the 2nd level trigger itself. The 2nd level trigger selects events which contain a lepton candidate, according to the information from IPU; all these events are stored into the data file. We call them LVL2 events.

However, we do not want to acquire only the events with lepton pairs, but also events which contain only hadrons; if we would record all the 1st level triggered events without

any further scaling, the stored data will be dominated by hadronic reactions.

The downscaling box purpose is to select and scale down events in a statistical fashion, regardless of whether they contain lepton pairs or not. In this case we talk about down-scaled events.

Figure 2.12 represents a scheme of the event selection used for data acquisition. A first selection of events is done by the 1st level trigger (yellow boxes), and they are sent to the matching unit, where the downscaling factor is set to 4. This means that one event out of four is stored (1,5,9,13,...), regardless of the 2nd level trigger decision. It is flagged as downscaled in the event header and the related downscaling factor is stored as well. All the events with a recognized lepton are stored as well, and flagged as LVL2. This means that an event can be at the same time downscaled (LVL1) and with positive 2nd level trigger decision (LVL2) like for instance the event number 13 in the example.

If we want to have the total number of 1st level triggered events, we must multiply the number of downscaled events (4) by the downscaling factor (4); in this case we obtain 16 triggered events, against 7 which are effectively stored to file. In this particular case we are roughly saving half of the disk space, and half of the time needed for the data acquisition.

In fact 2nd level trigger has an efficiency below 100%, therefore in evaluating the number of dilepton events in the data sample this correction has to be taken into account.

Chapter 3

HADES Tracking

In this section the tracking algorithm of the HADES spectrometer is described. The tracking procedure consists of several steps: track finding, track fitting and momentum reconstruction. For the momentum reconstruction, different methods have been developed described in the following sections.

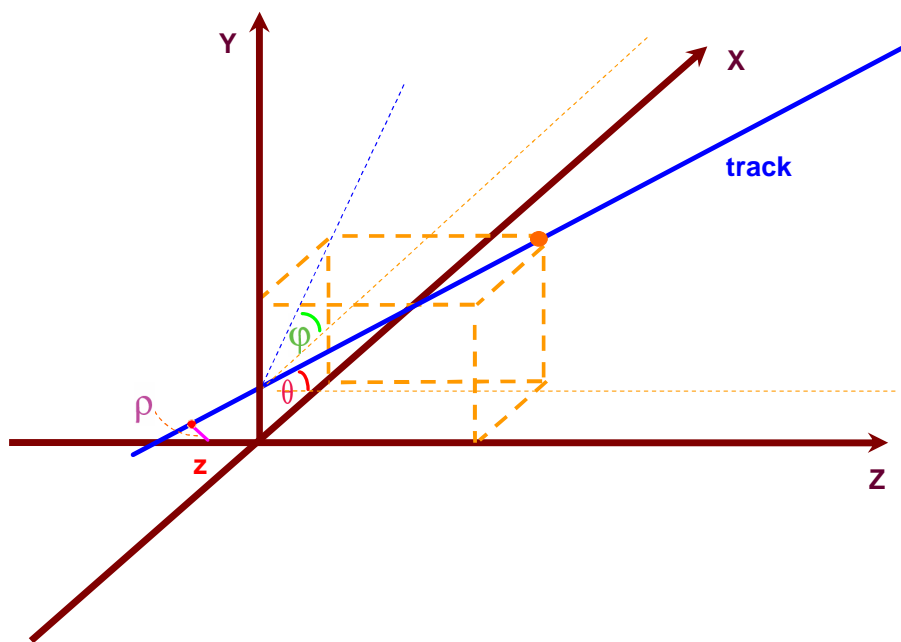


Figure 3.1: Track parametrization (θ, ϕ, ρ, z) in the HADES experiment.

3.1 Track parametrization in the HADES experiment

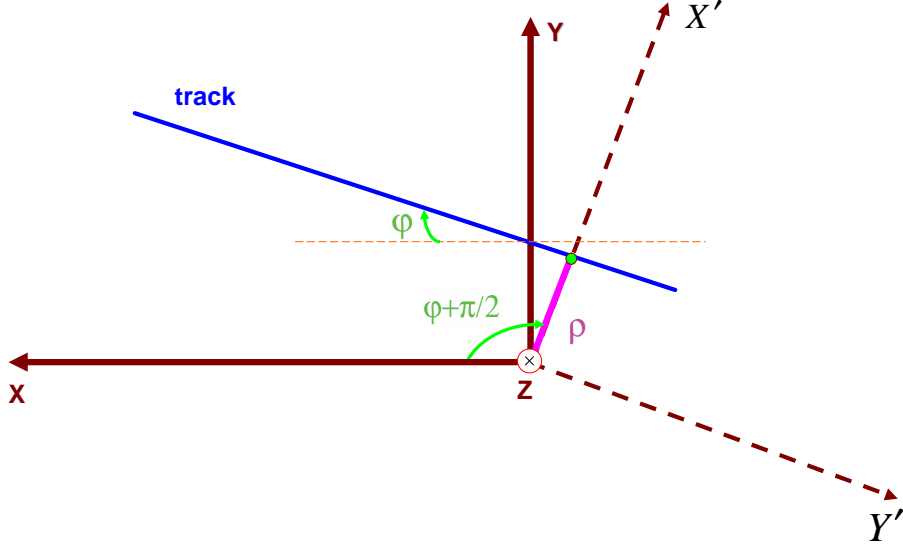


Figure 3.2: The track viewed along the z axis. The beam is directed perpendicular to Figure plane, along z axis.

In the HADES experiment a track is parameterized with four variables in the sector coordinate system:¹ θ , ϕ , ρ and Z . Here θ and ϕ are polar and azimuthal angles correspondingly, ρ is a distance between the z axis and a closest point of the track to that axis, and Z is the z coordinate of that point. Let us assume the x and y coordinates of the closest point on the track to z axis to be X and Y (See Figure 3.2 (the z axis is perpendicular to the Figure plane)). In the Figure the blue line represents the track while the pink line shows the closest distance from the track to the z axis looked at in the direction of the z axis. It can easily be seen from Figure 3.2 that, if we rotate our coordinate system around z axis by an angle $\phi + \pi/2$, which can be realized by the following rotation matrix:

$$\begin{pmatrix} \cos(\phi + \pi/2) & \sin(\phi + \pi/2) \\ -\sin(\phi + \pi/2) & \cos(\phi + \pi/2) \end{pmatrix} \quad (3.1)$$

in the new coordinate system (X', Y') the ρ vector will be along the X' axis with its module being equal to $\sqrt{X'X'}$; therefore the x coordinate of the closest point will be just

¹In the Hades experiment a left-handed coordinate system as illustrated in Figure 3.1 is used. Sector coordinate system means that the system is attached to the sector. In this coordinate system the ϕ angle ranges between 60^0 and 120^0 . It is just rotated with respect to the LAB coordinate system by an angle $n*60^0$ where n stands for the sector number.

just to the module of the closest distance (ρ), while the y coordinate will be equal to 0, which can be written using the above transformation matrix:

$$\begin{cases} \rho = X * \cos(\phi + \pi/2) + Y * \sin(\phi + \pi/2) \\ 0 = -X * \sin(\phi + \pi/2) + Y * \cos(\phi + \pi/2) \end{cases} \quad (3.2)$$

Solving equations 3.2 one can easily obtain:

$$\begin{cases} X = \rho * \cos(\phi + \pi/2) \\ Y = \rho * \sin(\phi + \pi/2) \end{cases} \quad (3.3)$$

The next step is to obtain the directions, for instance, by taking the unit radius sphere around (X, Y, Z) point.

$$\begin{cases} dirX = \sin(\theta) * \cos(\phi) \\ dirY = \sin(\theta) * \sin(\phi) \\ dirZ = \cos(\theta) \end{cases} \quad (3.4)$$

3.2 Track reconstruction algorithm

The main purpose of the tracking algorithm is to find the four parameters described in the previous section which define the orientation of the track pieces (segments) in space before and after the MAGNET belonging to a given track. Furthermore, using the information from track bending inside the magnetic field, the momentum of the track is calculated as well. The HADES track reconstruction algorithm consists of several steps:

- Track finder
- Track fitter
- Momentum reconstruction

In the track finder the initial position of the track is found using only geometrical considerations which serves then as an input to the track fitting.

The track fitting algorithm improves the parameters found by the track finder by changing the track orientation in space so that the measured and calculated drift times fit to each other. The relation between drift time and position is taken from GARFIELD simulations. For each orientation of the track with respect to the drift cell in terms of minimum distance to the wire and impact angle to the cell there is a calculated value of the drift time with corresponding error. Furthermore during the track fitting procedure a filtering mechanism is applied which decides whether the found set of wires (cluster or track candidate) from track finding is fake or not and removes wires from the cluster which do not belong to it.

For momentum reconstruction different methods have been developed:

- Method of kick plane
- Spline method
- Runge-Kutta method

The method of kick plane uses tabulated trajectories created using simulated data in order to define the momentum of the particle from the momentum kick. The method of spline uses a cubic spline track model inside the magnetic field for estimation of the track points together with the derivatives at several points inside the field region. The momentum is derived by solving the equation of motion of the charged particle through the field by forcing the particle to travel along the model assumed. The momentum is a parameter of the method which means that there is no need to provide an initial value of the momentum. In the Runge-Kutta Method the equations of motion which are the second order differential equations, are solved by using iterative Runge-Kutta methods taking all initial conditions from spline (momentum) and track fitting (angles and directions).

3.3 Track finder

The information obtained from the MDCs are the hardware addresses of fired wires² which are converted into the wire numbers using lookup tables. If one tries to solve the problem by taking all possible combinations of fired wires which might belong to one track, the resulting number of combinations per chamber can be very high. Therefore one needs a filtering mechanism to decrease the number of combinations.

As it was mentioned before, each module is composed of six layers of signal and potential wires under different angles with respect to the bases of the MDC module and seven layers of cathode wires oriented under 90^0 with respect to the bases. The existence of six planes of sense wires with high efficiency allows one to reconstruct track pieces (segments) in each MDC separately. This mode of track finding we will call "chamber mode" track finding, because information from one chamber is used to obtain a track segment.

²The wire which gave a signal above threshold. In the text we will refer to these wires as fired wires.

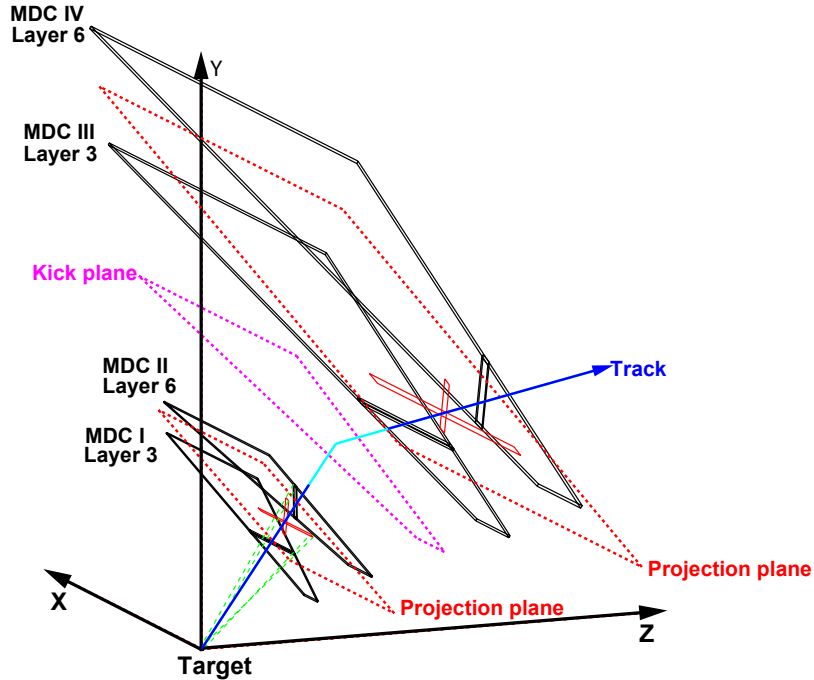


Figure 3.3: Projection of fired wires onto the plane for the combined mode of cluster finding.

The stray magnetic field inside the MDCs was neglected in first approximation, thus allowing to assume a straight track model before and after the magnetic field. Owing to this, it is possible to use information from MDCI-MDCII and MDCIII-MDCIV sets simultaneously, the mode of cluster finder being called a "combined mode" in this case.

The main idea of the method is to project the images of drift cells corresponding to each wire onto one virtual plane as shown in Figure 3.3 [41, 42, 43]. Due to the extended structure of the target, the projection for each wire is done with respect to the first point (in beam direction) and the last one of the target the net "shadow" being assumed as a projection of the wire cells on the projection plane (transverse size of the target is neglected). This procedure can be visualized by putting a screen instead of projection plane and illuminating the drift cells of the wire with a linear source of light with the dimensions of the target placed in its position.

The projection plane is selected between MDCI and MDCII so that the transverse sizes

of projected wires from both MDCs onto the plane have approximately the same value³.

Having projected all fired wires from both MDC's onto the projection plane, one looks for their intersection regions as shown in Figure 3.4. (Wires belonging to the same track coming from the vertex will give an intersection regions on the projection plane). A two dimensional histogram is created⁴ and the bins corresponding to the projection of the wire in the projection plane are increased by 1 for each layer⁵, so that in the intersection regions we have peaks.

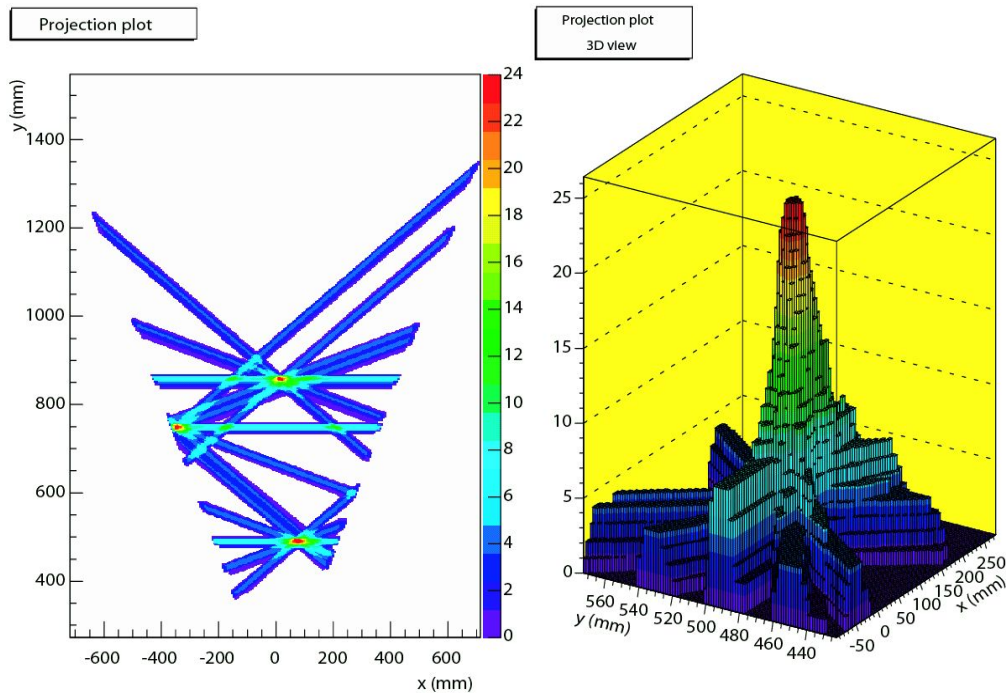


Figure 3.4: Two dimensional (left) and 3 dimensional(right) views of the projected wires

As a peak we consider the set of neighboring bins with a value more or equal to the defined value of H_{min} which is called the level of the cluster finder. The next important step is to set the value for H_{min} to be considered as a candidate for a track. The smaller

³Here we describe in general how the track finder works. Depending on the mode of the cluster finding, the projection plane is selected. For example in "chamber mode" the projection plane is selected in the middle of each MDC while in combined and mixed mode it is selected between two corresponding MDC chambers.

⁴The bin size in X direction is 2.7 times bigger than in Y direction due to the better resolution in Y direction coming from the orientations of wires in layers.

⁵If there are two fired wires belonging to the same layer, the bin content is increased by only 1.

the peak level, the more fake track contributions one has. Furthermore the probability of combining of two peaks into one peak is also high in this case. The larger its value, the smaller the efficiency. The optimal choice depends on 3 parameters: occupancy of MDC, efficiency of MDC and minimal number of fired wires for track reconstruction. In our case the minimum number of fired wires for track reconstruction is 4. So in this case it is not reasonable to search peaks of height less than 8 (four from each chamber).

The position of the projection plane being known, it is possible to define the spatial coordinates of the cluster with corresponding errors.

In order to define the position each bin is assigned a weight; $w_i = H_i - H_{min} + 1$. One can now use the standard way of position and resolution finding of the cluster.

$$\begin{aligned}\bar{x} &= \frac{\sum_{i=1}^n (x_i W_i)}{\sum_{i=1}^n W_i} \\ \bar{y} &= \frac{\sum_{i=1}^n (y_i W_i)}{\sum_{i=1}^n W_i} \\ \Delta\bar{x} &= \sqrt{\frac{\sum (x_i^2 W_i)}{\sum W_i} - \bar{x}^2 + \left(\frac{s_x}{2}\right)^2} \\ \Delta\bar{y} &= \sqrt{\frac{\sum (y_i^2 W_i)}{\sum W_i} - \bar{y}^2 + \left(\frac{s_y}{2}\right)^2}\end{aligned}\tag{3.5}$$

Here s_x and s_y are corresponding bin sizes in x and y direction⁶.

After calculation of \bar{x} and \bar{y} of the cluster with the corresponding errors one can calculate the z position of the cluster from the known position of the projection plane; therefore the output information from the track finder are:

- The list of wires with corresponding numbers belonging to the cluster
- The spatial position of the cluster with corresponding errors

The position of the cluster is assumed in first approximation as point on the particle trajectory, the second one being the center of the target.

Sometimes it is necessary to combine different clusters into one. This is done, for example, if there are two close clusters with contributing wires close to each other.

So far we were discussing the method of cluster finding in inner MDCs (before the magnet). The basic idea of cluster finding in the outer MDCs is the same. Nevertheless there are some differences in terms of reference point and the fact that the outer MDCs are parallel to each other.

After reconstruction of the inner segment, its intersection as well as intersection errors with a kick plane (the definition of the kick plane is described in the following sections)

⁶Note that the square of the bin half is added for Δx and Δy because, for example, if only one bin was taken then the errors would be equal to zero.

are calculated. The region in kick plane which is defined as the point of intersection with the errors are taken as a reference point for performing the projection for the outer MDCs. From here on the procedure of cluster finding is similar to that for inner MDCs with kick plane region substituting the target and the projection plane selected between MDC3 and MDC4 being parallel to them. There are some technical differences as well due to the parallel arrangement of the outer MDCs.

One of the important features of the cluster finder is that the rough matching between inner and outer segments is done intrinsically. The outer clusters are looked for within the region on the kick plane defined as the intersection of inner segment with its corresponding errors. This procedure can also be illustrated as an illumination of the outer clusters with the source of light positioned on the intersection point of an inner segment with the kick plane with its dimensions equal to the corresponding errors of the interaction point. This so-called on-fly matching is working quite well if all four MDC chambers are present in the sector. In case of 3 MDC chambers, the matching quality is bad because of the short lever arm and fewer contributing wires. Therefore the number of fake tracks in terms of not matched inner and outer segments is larger as well.

The mode of cluster finder to be used depends on the aim of the analysis, e.g for alignment purposes of the MDC chambers relative to each other the "chamber mode" should be used. For physics analysis it is preferable to use the "combined mode" in order to achieve higher resolution. Unfortunately this choice sometimes can be inefficient because of some problems with working layers and layer efficiencies in the setup; therefore in combined mode the requirement of at least 8 wires (4 from each MDC) can decrease the efficiency of the track finder. A third mode for the cluster finder, the "mixed mode" was developed which projects the wires from both MDCs onto the plane like in combined mode. The condition of at least 4 tracks is put only to the number of wires contributing to found cluster from one MDC chamber. As soon as this condition is fulfilled for any of the chambers there is no such conditions put on the number of wires from another chamber. Nevertheless, in order to increase the resolution obtained, one can put a lower limit on the number of wires from another MDC as well, not necessarily to be 4 as in combined mode, but for example 2.

For the data without magnetic field, it is also foreseen to use for track finding all four MDCs simultaneously. In this case the fired wires from all four MDCs are projected onto one projection plane. This mode of cluster finder was used several times during data taking without magnetic field in order to reconstruct the target position online.

3.4 Track fitter

The information available for track fitting is the number of wires contributing to the cluster with the position of the cluster.

Using this information it is possible to reconstruct a straight line (the second point be-

ing the middle of the target) and calculate the minimum distance between the fired wire and the track with the impact angle to the cell to which there is a corresponding calculated drift time from simulation. In addition the error of the drift cell is also available as a function of minimum distance from the wire and the impact angle which is generated using GARFIELD simulations. Due to the fact that the time offset calculation was based on the fastest particle arrival time, which is set to zero, the measured drift times will be defined with respect to the fastest particle arrival time. Therefore this additional parameter t_{offset} should be added to the calculated drift time (or subtracted from the measured one). During the minimization procedure, this parameter is calculated by forcing the minimization function to be centered at zero. This parameter is not coming only from the fact that the drift time is measured with respect to the fastest particles arrival time. There can be some other reasons which can generate an offset in time, e.g, electronic noise and so on. Therefore we will use a t_{shift} parameter which is equal to t_{offset} plus other components for time shift.

From a mathematical point of view the purpose of the track fitting is to minimize the function [44, 45]:

$$\chi^2 = \sum \frac{(t_i + t_{shift} - T_i)^2}{(\Delta T_i)^2} w_i \quad (3.6)$$

where t_i is the calculated drift time according to the orientation of the reconstructed segment with respect to a given drift cell in terms of distance from the wire and impact angle to the cell, T_i is the measured drift time after time offset subtraction, t_{shift} is the parameter which was described before and w_i are weights

In general the residuals in Equation 3.6 should follow a Gauss distribution if all the wires contributing to the cluster are fired by the track under investigation. These wires we will call "true" ones, while to the wires contributing from other tracks or the noisy wires in the cluster we will refer to as a "fake" ones. The contribution of fake wires to the cluster flattens the residual distributions, this in turn makes trouble for traditional least square fitting.

Straightforward application of the maximum likelihood method improves the situation significantly, but this procedure is quite slow and complicated. Therefore we use a weighted least squares fitting [42, 43, 44, 46].

Using the maximum likelihood method for the χ^2 function defined in Equation 3.6 it is easy to show that the obtained weights can be approximated via the functions:

$$w = \begin{cases} \left[1 - \left(\frac{\chi_i^2}{c_4 \sigma} \right)^4 \right]^2 & |\chi_i| \leq c_w \sigma \\ \left[1 - \left(\frac{\chi_i^2}{c_2 \sigma} \right)^2 \right]^2 & c_w \sigma \leq |\chi_i| \leq c_2 \sigma \\ 0 & |\chi_i| > c_2 \sigma \end{cases} \quad (3.7)$$

with $c_w = 2.54$, $c_4 = 3.26$ and $c_2=4.19$. The second function in 3.7 corresponds to the well known bi-weight of Tukey. The use of the first function is motivated with the fact that

the Tukey bi-weights do not fit the optimal weights obtained from the maximum likelihood method in all regions of the χ^2 . The distribution of the weights as a function of χ^2 ⁷ is shown in Figure 3.5, for a $\sigma = 2.5$ ⁸.

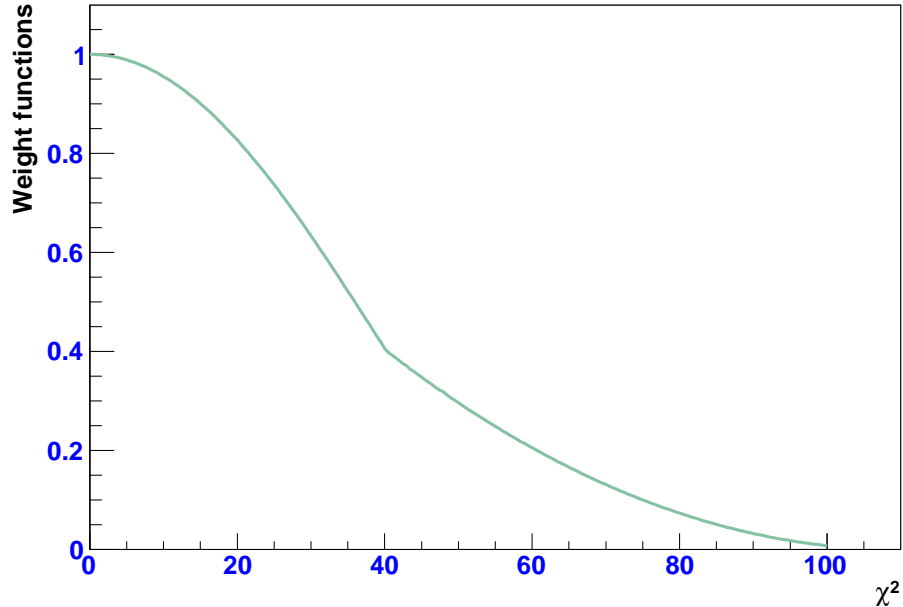


Figure 3.5: The value of the weight as a function of χ^2 .

The described weights are used in order to weight each term in Equation 3.6 during the minimization procedure and to filter out the contributing fake wires. In our case we stop filtering if $\sigma < 2.5$.

The first weighting is done without any fit, just by taking the track approximation found by the cluster finder and taking the corresponding calculated times and errors. After assigning a weight in this way the fitting is starting and after each three iterations the new weights are calculated. After filtering out the fake wires from the cluster, the last iteration of fitting is done by setting all weights to 1 for the remaining wires.

We have defined two planes⁹ being the first plane of first MDC and the last plane of the second MDC. The intersection points of the reconstructed segments with these planes define the orientation of the track in space¹⁰; therefore the function χ^2 (See Equation 3.6) depends on four parameters. The offset parameter is calculated each time numerically. We can rewrite Equation 3.6 as:

⁷With χ^2 defined in Equation 3.6.

⁸ σ is the width of the weight distribution as shown in Figure 3.5

⁹In "chamber mode", the planes are the first and last planes of each MDC.

¹⁰As the z positions of the planes are known, one needs only x and y coordinates of the intersection points. Therefore the track is defined with four parameters.

$$\chi^2 = \sum \frac{(T_i - f_i(x1, y1, x2, y2, t_{shift}))^2}{(\Delta T_i)^2} w_i \quad (3.8)$$

where $x1, y1, x2, y2$ are the intersection points of the track with the corresponding planes, with T_i, t_{shift} and w_i defined in Equation 3.6.

In the minimization procedure the gradient downhill method is used where all the parameters of the function are incremented simultaneously with relative magnitudes so that the resultant direction of travel in parameter space is along the gradient of the minimization function.

The gradient $\nabla\chi^2$ is a vector that points in the direction in which the function χ^2 increases most rapidly and has components in parameter space equal to the rate of change of the function along each axis:

$$\nabla\chi^2 = \sum \frac{\partial\chi^2}{\partial x_k} n_k \quad (3.9)$$

with n_k being a unit vector in the direction of the x_k coordinate axis.

The search starts by changing all parameters simultaneously as:

$$\vec{x}_{k+1} = \vec{x}_k - \frac{\nabla\chi^2}{|\nabla\chi^2|} \Delta R \quad (3.10)$$

where ΔR is an iteration step.

For each changed parameter sets the χ^2 is calculated until after the k-th iteration the function starts to rise. Using $\chi_k^2, \nabla\chi^2$ and χ_{k+1}^2 it is possible to approximate the function χ^2 with a parabola, whose minimum can be found easily. Finally the minimum is found as:

$$\vec{x}_{k+1} = \vec{x}_k - \frac{\nabla\chi^2}{|\nabla\chi^2|} \Delta R_1 \quad (3.11)$$

Where ΔR_1 is the increment of the parameter corresponding to the minimum of the parabola.

The main disadvantage of this approach is that it needs a lot of iterations. Therefore the following scaling has been used in order to speed up the minimization procedure: the gradient has both magnitude and dimensions and, furthermore usually the components of the gradient do not have the same dimensions, giving for the contour plot of a χ^2 an ellipse. Furthermore, if there is a correlation between parameters, the ellipse is tilted with respect to axis along the given parameters. As an example we can take a function of the form:

$$f = Ax^2 + By^2 \quad (3.12)$$

which depends only on two parameters. The path of the minimization follows the zigzag way as shown in Figure 3.6(a) that is why the method is slow. By making a substitution

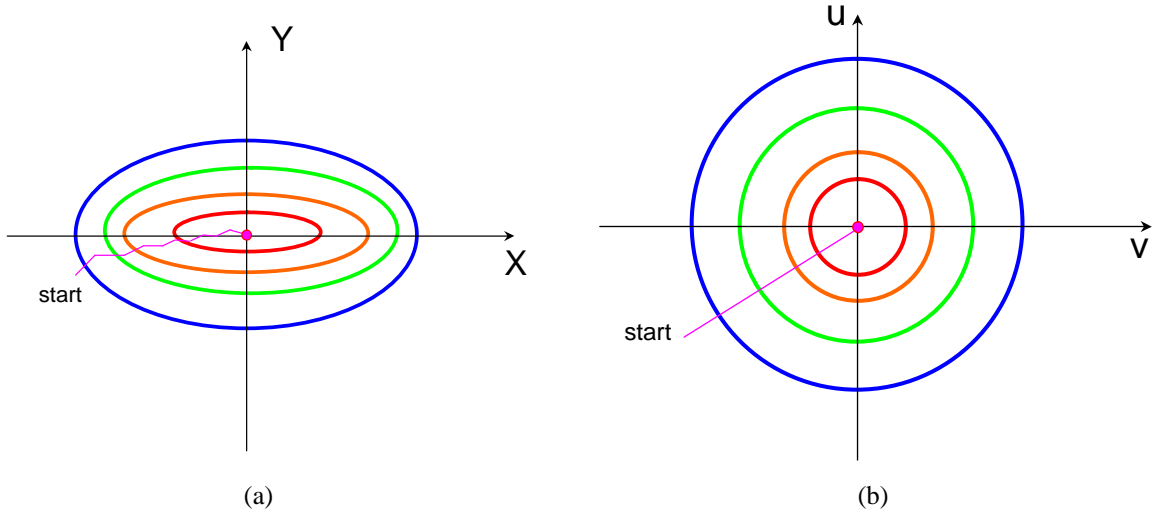


Figure 3.6: Scaling of the fit parameters in order to speed up the minimization procedure.

$$u = x\sqrt{A} \quad (3.13)$$

$$v = y\sqrt{B}$$

one can write write the Equation 3.12 as

$$f = u^2 + v^2 \quad (3.14)$$

which is the equation of a circle. In this case the the gradient is passing through the exact minimum (see Figure 3.6(b)).

The gradient method will not asymptotically approach the minimum because around the minimum the gradient will be equal to 0. A more sophisticated approach is used near the minimum by using the second order partial derivatives:

$$\frac{\partial \chi_{k+1}^2}{\partial x_j} = \frac{\partial \chi_k^2}{\partial x_j} + \sum \frac{\partial^2 \chi_k^2}{\partial x_j \partial x_l} \Delta x_l \quad (3.15)$$

giving a system of linear equations

$$\sum \frac{\partial^2 \chi_k^2}{\partial x_j \partial x_l} \Delta x_l = -\frac{\partial \chi_k^2}{\partial x_j} \quad (3.16)$$

which can be solved against Δx .

The error propagation is done using the standard error propagation procedure.

3.5 Alignment

Both track finder and track fitter need geometrical positions of detectors and detector parts, e.g. chamber position, layer position, wire position, target position and so on. During the mounting process components can be shifted from their ideal positions, and this will affect the precision of reconstruction. The main task of the alignment is to define possible shifts and/or rotations of detector components and to correct for them.

The alignment procedure used in the HADES experiment is based on photometric measurements and cosmic-ray data for the inner chambers, and on straight track reconstruction in runs without magnetic field for the outer ones [47].

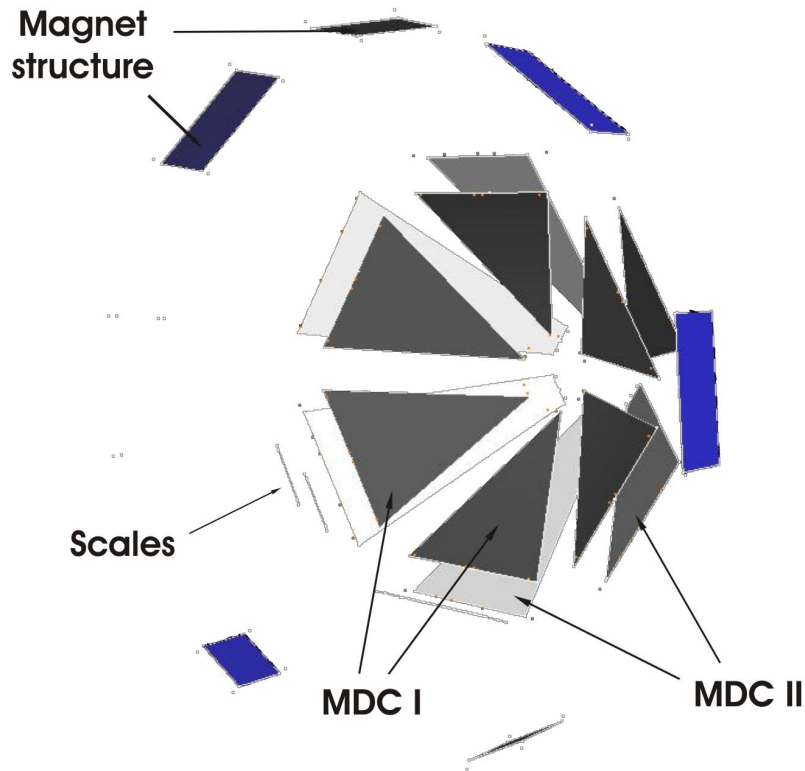


Figure 3.7: 3D view of measured MDCI and MDCII points

Photometry is a photo-camera based method to survey objects in three dimensions. For this purpose 8 Mega pixel mirror reflex camera with a special 20 mm USM wide angle lens was used to take high-resolution pictures of large areas from short distances. The analysis of these pictures was done with the software PhotoModeler 5.0.

First, the camera was calibrated by photographing a special array with fixed positions.

We used special markers which have a typical size of 2-3 cm and were glued directly to the detectors. The software applies a fit to the marker pattern and then calculates the center

of gravity in sub-pixel precision.

First, the photos were taken from MDCII chambers and the magnet support structure and then, after moving the MDCI chambers to measuring position, the same procedure was done for MDC I. After processing in the PhotoModeler software and merging of two projects a 3D-view of the measured points of MDCI,II was obtained as shown in Figure 3.7.

As for the experiment, the MDCI chambers were moved into their nominal positions their relative alignment with respect to MDCII planes was done using cosmic rays which are mainly high-energetic muons at sea level ¹¹.

The cosmic rays were taken with an opposite-sector (Tof/Tofino) trigger with a mean data rate of 80Hz.

The track reconstruction method has been optimized for reconstruction of cosmic rays, as they do not come from the target. The reconstruction procedure stays the same with the only difference that as a starting point the META hit is taken.

We start from the point where the position of the MDCI chambers relative to MDCII chambers are fixed by the PhotoModeler survey as described before. Furthermore MDCII chambers are aligned relative to the magnet. From the reconstructed hit and the direction the straight line is constructed and its intersection with the MDCII plane is calculated. The position and inclination of the MDCI chamber is changed until the distance between the reconstructed hit in the MDCII and the intersection point with it reaches a minimum.

The alignment of the outer chambers was done with straight tracks from the target using no-magnetic field data. Since we have an alignment of the inner chambers, as described before, we can use the straight tracks after track reconstruction from these runs to align the outer chambers. MDCI and II are fixed now in position. The positions and inclinations of the outer chambers are varied until the minimum distance between the line, constructed by the reconstructed hits from two inner chambers, and the hits reconstructed in outer chambers reaches its minimum value.

3.6 Matching of hits

The main purpose of the matching algorithm is to find out which of the reconstructed hits from different detector systems corresponds to a given track. As it was mentioned in the previous section, the matching between inner and outer segments is roughly done during track finding.

Here we will discuss the matching procedure of track candidates with the META and RICH detectors. Moreover, the more precise matching between inner and outer segments will be discussed as well.

¹¹The relative alignment of the MDCI to MDCII chambers were also done using PhotoModeler software which is assumed as a first approximation for the alignment with comics.

The matching algorithm with the META detectors described here is for the case when there is at least one existing MDC chamber after the magnet in the setup, therefore one has reconstructed outer MDC segments.¹² From the reconstructed outer MDC segment one can construct a straight line in space. At this point we have an information from the META detectors, as well in terms of reconstructed hit (its coordinates), as of module number where the signal was created. Using the module geometry we find the intersection of the line corresponding to the reconstructed outer segment with the module of the META detector.

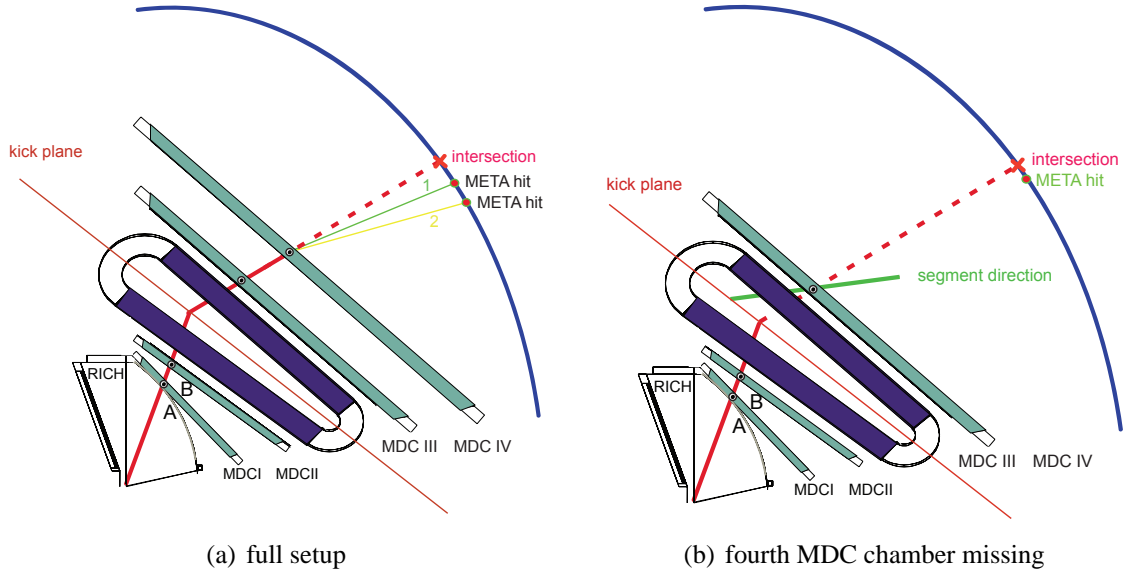


Figure 3.8: Matching of track candidates with META hits in case of (a) four MDC chambers and (b) three MDC chambers.

Having this information we can define quality parameters as:

$$qTof = \sqrt{\left(\frac{xTof - xInt - x_{offset}}{\sigma_x}\right)^2 + \left(\frac{yTof - yInt - y_{offset}}{\sigma_y}\right)^2} \quad (3.17)$$

where $xTof$ and $yTof$ are the coordinates of reconstructed TOF hits, $xInt$ and $yInt$ are the intersection points of the outer MDC segments with the TOF module, σ_x and σ_y are corresponding TOF hit resolutions, while x_{shift} and y_{shift} are introduced so that the residuals in Equation 3.17 are centered at 0.

In a similar way we define the quality parameter for matching with SHOWER hits:

¹²Even in this case different approaches have been used to match the detectors depending whether there are two or one existing MDC chambers after the magnet.

$$qSh = \sqrt{\left(\frac{xSh - xInt - x_{offset}}{\sigma_x}\right)^2 + \left(\frac{ySh - yInt - y_{offset}}{\sigma_y}\right)^2} \quad (3.18)$$

If the value of the quality parameters calculated via Equations 3.17 and 3.18 are smaller than pre-defined values of this parameters (called quality cuts) the object of matching is created ¹³.

In order to define the quality cut, the distribution of the residuals entering into Equations 3.17 and 3.18 were plotted first and the cuts were applied around the peak of the distributions. In addition to that the shift of the distributions are calculated as well by making the residual distribution to be centered at zero. We have used quite large cut windows in order not to lose statistics at this point.

Each track candidate (matched inner and outer segments) is matched with every META hit in the event satisfying the quality condition described above. The situation is even more complicated because one track candidate can match with several META hits as shown in the Figure 3.8(a).

Therefore there will be some fake combinations which should be removed afterwards. This kind of fake candidates we will call "meta fakes". Furthermore there can be the case when one inner segment matches with two outer ones or one outer segment is matched with several inner segments, these fakes being called the "track fakes". All these situations can be manipulated with the functions provided in the software (For details see Appendix F).

Matching of the RICH rings with the MDC segments is done by defining two quality parameters:

$$qPhi = \frac{(\varphi_{rich} - \varphi_{mdc} - \varphi_{offset}) * \sin(\theta_{mdc})}{\sigma_{rich}} \quad (3.19)$$

$$\Delta\theta = \theta_{rich} - \theta_{mdc}$$

The matching is done if $qPhi$ and $\Delta\theta$ defined in 3.19 satisfy the conditions:

$$qPhi < qPhi_{max} \quad (3.20)$$

$$\theta_{min} < \Delta\theta < \theta_{max}$$

where the $qPhi_{max}$, θ_{max} and θ_{min} are defined beforehand by plotting the distributions defined in 3.19.

If there are several rings matching with the same inner segment the corresponding ring candidates are stored in an array of defined size (3 in our case), the first one being the best one in terms of quality parameters.

¹³The matching object is also created if none of the META hits are matched with a given track candidate. In this case the value of quality parameters are set to -1.

The matching procedure of the outer segments with the META hits are done in a little different way in case of only one existing outer MDC chamber. In this case the reconstructed angles for outer segments can be wrong. This may happen because of the short lever arm and because of less contributing wires. In this case, during the track fitting, the segment can freely be rotated thus giving the wrong angles at the end. Even if the angular information might not be satisfactory in this case, the hit position which is nothing but the intersection of the segment with the middle plane of the chamber will still be reasonable. Therefore, as one of the reference points we take this hit position. In order to reconstruct the straight line we need another point because we are not using the angular information. This point is taken as the intersection point of the inner segment with the kick plane as shown in Figure 3.8(b). From these two points (point on kick plane and the hit position) we construct a straight line and find its intersection with the META module, the rest of the procedure being analogous to the case of matching with four MDC chambers.

When a particle interacts with the sensitive volume of the TOF detector it can hit several scintillator rods which can be misinterpreted by the TOF hit finder as a series of hits caused by several incident particles and leads in general to overestimation of the event multiplicity. For the set of hits located in the TOF detector the name *TOF cluster* will be used. In order to cluster the hits caused by one particle and to do not cluster the hits caused by multiple particles a special algorithm was created the output of which contains the found clusters with the number of TOF hits entering the cluster (cluster size). On the matching level the candidates are created for TOF cluster and two TOF hits entering the cluster¹⁴. The situation is more complicated here because the same TOF cluster and/or the hits entering to cluster can match with different track candidates. The conclusion whether the TOF cluster of the hits should be used in the analysis is done with separate algorithm. Currently it was decided to use only cluster information in case of cluster size two and not to use hit information.

Another double counting of META hits can come from a hardware overlap on TOF and SHOWER detectors. In this case, two hits in the META detector will be reconstructed from one track, one of them coming from the TOF detector and another one coming from the SHOWER detector. In this case two matching objects are created, one corresponding to the matching with the TOF hit and another one corresponding to the SHOWER hit. One of these candidates is excluded by an overlap checking algorithm. At the moment the matching only with the TOF hit is taken while matching with the SHOWER hit is excluded because of better resolution of the TOF hit.

On the META matching level broad matching windows are used in order not to lose a tracks on this level. It is foreseen that track cleaning algorithms should be developed in order to remove the fake combinations created on the matching level. This procedure will be discussed in the analysis part of this thesis.

In general there can be several outer segments matching with a given inner segment,

¹⁴Only the cluster size of two is considered in the matching algorithm.

or several inner segments can match with one outer segment. This matching is done during track finding. In order to remove fake tracks created on this level one can introduce matching qualities of inner segments with outer ones. The quality parameter is introduced as:

$$q = \sqrt{\frac{(X_{in} - X_{out})^2}{\sigma_{X_{in}}^2 + \sigma_{X_{out}}^2} + \frac{(Y_{in} - Y_{out})^2}{\sigma_{Y_{in}}^2 + \sigma_{Y_{out}}^2}} \quad (3.21)$$

where $X_{in}, Y_{in}, X_{out}, Y_{out}$ are corresponding intersection points of inner and outer segments with the kick plane and $\sigma_{X_{in}}, \sigma_{Y_{in}}, \sigma_{X_{out}}, \sigma_{Y_{out}}$ stand for corresponding errors of the intersection points.

Another alternative would be to calculate the minimum distance between the inner and outer segments, and cut on the distance between that point and the kick plane.

3.7 Kick plane algorithm

As it was already mentioned in previous sections the track segments before and after the the magnetic field can be expressed in a first approximation as straight lines. Because of the toroidal magnetic field in the HADES experiment the tracks are mainly bent in one plane; the inner and outer segments belonging to the same track should meet at some point. In fact, because of the resolution, these segments do not cross exactly, therefore one uses a minimum distance between them in space i.e the vertex defined by these segments. The interesting observation is that if one makes a 3D plot of the coordinates of those vertex points one discovers that they lay in a surface which is called a *kick surface* [48]¹⁵.

¹⁵Sometimes in the text the kick surface is referred to as kick plane.

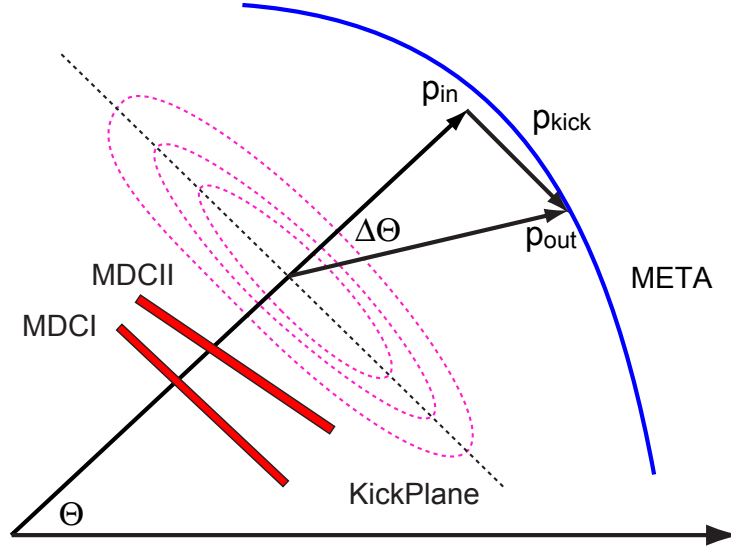


Figure 3.9: Illustration of the kick plane algorithm.

It is clear that a particle with given direction will always hit one spot on the *kick surface* independent of the momentum it has. It can be shown that the momentum of the particle can be calculated using:

$$p = \frac{p_{kick}}{2 \sin(\Delta\theta/2)} \quad (3.22)$$

where p_{kick} is the momentum kick and $\Delta\theta$ is the deflection angle as shown in Figure 3.9. p_{kick} depends on the geometry of the field and can be parameterized as function of θ , ϕ and $\Delta\theta$. In order to obtain p_{kick} , simulations were performed where for each point in the kick plane and the deflection angle, the momentum kick was stored in multi dimensional tables (See [48] for details).

This method for momentum determination is used for those sectors where only two MDC chambers existed in the set up; therefore the direction before the magnetic field was provided by MDCI and MDCII, while the direction after the magnetic field was taken from the META hit and the intersection point of the inner segment with the kick plane. The resolution of this method ranges between 7% – 20% as a function of the momentum of the particle ranging from 100MeV to 1500MeV.

For the sectors where 4 or 3 MDC chambers were mounted the method of spline and Runge Kutta are used to obtain the particle momentum. They are discussed in the next sections.

3.8 Method of spline

A particle's momentum is obtained from its deflection in the magnetic field. In order to define the momentum of the particle by solving a field equations either the trajectory of the particle or the initial momentum should be known with good precision. As there are no detectors in the field region of the HADES spectrometer and the method of kick plane does provide a low precision initial momentum, the model of cubic spline for the trajectory of the particle is assumed.

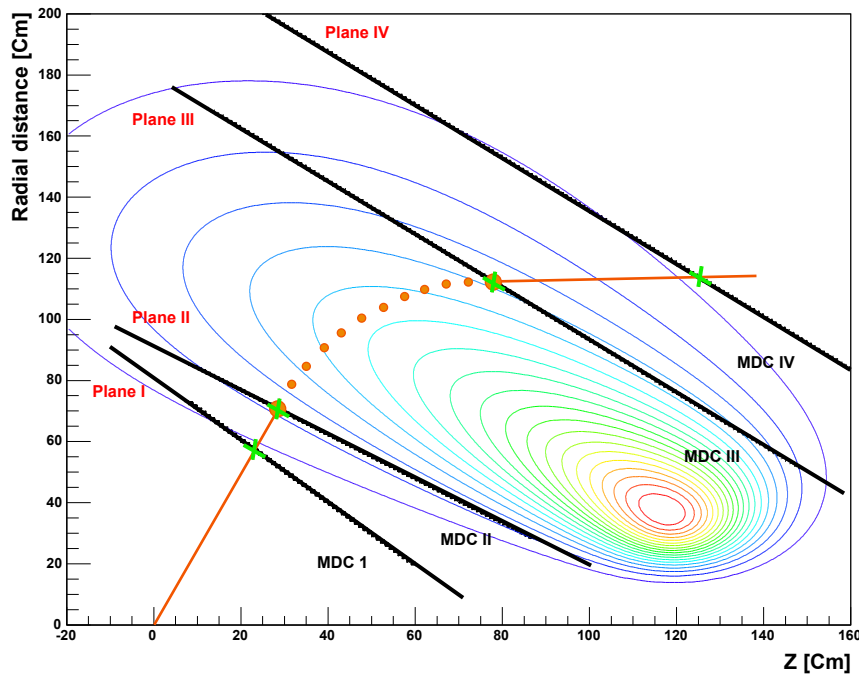


Figure 3.10: Positions of the fixed planes with respect to the main component lines of the magnetic field. The picture is obtained for the middle of the sector, $\phi = 90^0$. The radial distance means $\sqrt{X^2 + Y^2}$. Through intersection points of inner and outer segment with the corresponding planes (green crossings) the spline fit has been performed. The red points are selected from spline curve for which the equations of motion are solved.

3.8.1 Track model assumption

The algorithm described in this section consists of the following steps:

- Assumption of track model inside the magnetic field
- Solution of field equations

In principle we could use any track model which allows an explicit differentiation like a polynomial. If we attempt to represent by an n th-degree polynomial a function that is tabulated an $n+1$ points, we are apt to obtain disappointing results if n is large. The polynomial will necessarily coincide with the data points, but may exhibit large oscillations between points. In addition, if there are many data points, the calculation can become cumbersome. It is often better to make several low-order polynomial fits to separate regions of the function, and this procedure is usually satisfactory for simple interpolation in tables. However, if one wants a smooth function which passes through the data points the result may not be satisfactory [49].

A track model which is, therefore, practically suited is the cubic spline model. We go even one step further and assume a cubic spline method for the field or rather for the track's second derivative. The track model then becomes a quintic spline [50, 51].

A smooth curve that passes through the data points is obtained by requiring the first and second derivatives, as well as the function itself, to be continuous at the data points [52].

The input to the algorithm are reconstructed segments before and after the magnetic field and the field map. We calculate the intersection points of the reconstructed segments with the predefined planes (two before the magnet and the next two behind it) as shown in Figure 3.10. Through the found four intersection points in space we apply cubic spline curves in the YZ and XZ projections. In the next step we select equally distanced points from the obtained curves (X,Y,Z) in the space together with derivatives at those points. We then compute the magnetic field at the selected points using the field map to get three field components B_x, B_y and B_z .

In case of only one outer MDC chamber after the magnet the intersection points of the reconstructed segment from one outer MDC chamber with predefined planes are calculated giving back again four points in the space. However in this case the direction information from reconstructed segment is not used. The direction is calculated using two points the first being the intersection point of the inner segment with the kick plane and the second being the hit position found by tracking. The reason for this is explained in Section 3.6.

3.8.2 Field equations

Charged particle in the magnetic field experiences the Lorentz force which causes it to bend. In the LAB system of the HADES experiment we can write the equation of motion of a particle as:

$$\frac{d^2x}{dt^2} \equiv \ddot{x} = \frac{\dot{y}B_z - \dot{z}B_y}{m} \quad (a)$$

$$\frac{d^2y}{dt^2} \equiv \ddot{y} = \frac{\dot{z}B_x - \dot{x}B_z}{m} \quad (b) \quad (3.23)$$

$$\frac{d^2z}{dt^2} \equiv \ddot{z} = \frac{\dot{x}B_y - \dot{y}B_x}{m} \quad (c)$$

As we use a cubic spline approximation for the second derivative on coordinates as well, it is better to write the field equations in terms of second derivatives on coordinates rather than on time. For this we use the expressions¹⁶

$$\begin{aligned}\frac{\dot{y}}{\dot{z}} &= \frac{dy}{dz} \quad \text{and} \quad \frac{\dot{x}}{\dot{z}} = \frac{dx}{dz} \\ \frac{d^2y}{dz^2} &= (\dot{y}\dot{z} - \ddot{y})/\dot{z}^3\end{aligned}\tag{3.30}$$

By substituting in 3.30 the expression for \dot{y} and \dot{z} from 3.23 we obtain:

$$\frac{d^2y}{dz^2} = \frac{\dot{z}^2 B_x - \dot{x}\dot{z} B_z - \dot{x}\dot{y} B_y + \dot{y}^2 B_x}{\dot{z}^3 m}\tag{3.31}$$

Finally, using the first line of 3.30 together with

$$p = \dot{z} m \sqrt{1 + \left(\frac{dx}{dz}\right)^2 + \left(\frac{dy}{dz}\right)^2}\tag{3.32}$$

we write the field equation in the YZ plane in the following way¹⁷

¹⁶By writing

$$\frac{dy}{dt} \equiv \dot{y} = \frac{dy}{dz} \frac{dz}{dt} = \frac{dy}{dz} \dot{z}\tag{3.24}$$

we can obtain

$$\frac{\dot{y}}{\dot{z}} = \frac{dy}{dz}\tag{3.25}$$

and

$$\frac{\dot{x}}{\dot{z}} = \frac{dx}{dz}\tag{3.26}$$

In a similar way using

$$\ddot{y} = \frac{d^2y}{dt^2} = \frac{d}{dt} \left(\frac{dy}{dz} \frac{dz}{dt} \right) = \frac{d^2y}{dz^2} \dot{z}^2 + \frac{dy}{dz} \ddot{z}\tag{3.27}$$

together with

$$\frac{dy}{dz} = \frac{\dot{y}}{\dot{z}}\tag{3.28}$$

we obtain

$$\frac{d^2y}{dz^2} = \frac{1}{\dot{z}^3} (\dot{y}\dot{z} - \ddot{y})\tag{3.29}$$

¹⁷Note that in order to get the momentum in MeV/c , the right-hand side of the equation should be multiplied by $2.99[MeV/c]T^{-1}cm^{-1}$.

$$p \frac{d^2 y}{dz^2} = k(z) \left(B_x \left(1 + \left(\frac{dy}{dz} \right)^2 \right) - B_y \frac{dx}{dz} \frac{dy}{dz} - B_z \frac{dx}{dz} \right) \quad (3.33)$$

where $k(z)$ is defined as:

$$k(z) = \sqrt{1 + \left(\frac{dx}{dz} \right)^2 + \left(\frac{dy}{dz} \right)^2} \quad (3.34)$$

In an analogous way we can write the field equations in the XZ plane

$$p \frac{d^2 x}{dz^2} = k(z) \left(B_x \frac{dy}{dz} \frac{dx}{dz} - B_y \left(1 + \left(\frac{dx}{dz} \right)^2 \right) + B_z \frac{dy}{dz} \right) \quad (3.35)$$

with $k(z)$ defined in 3.34.

3.8.3 Solution of field equations

Our main goal in this section is to solve the equations 3.33 and 3.35 obtained in the previous section. The right-hand side of these equations can be evaluated at the selected points from the spline fit. Using the spline interpolation on this evaluated expressions we can determine the double integrals. If we denote by $A(z)$ and $C(z)$ the right-hand sides of the corresponding expressions we can evaluate the integrals:

$$Y_i = \int_{u=z_0}^{u=z_i} \left[\int_{v=z_0}^{v=u} A(v) dv \right] du \quad (3.36)$$

$$X_i = \int_{u=z_0}^{u=z_i} \left[\int_{v=z_0}^{v=u} C(v) dv \right] du$$

The right hand sides of 3.33 and 3.34 are the expressions for momentum times the second derivatives. Therefore the obtained solutions will be momentum times the corresponding coordinates. Furthermore we will have two integration constants from double integration. Therefore the solution of the equations 3.33 and 3.35 divided by momentum can be written as

$$\begin{aligned} Y_{equation_i} &= A_1 + A_2(z_i - z_0) + Y_i/P \\ X_{equation_i} &= B_1 + B_2(z_i - z_0) + X_i/P \end{aligned} \quad (3.37)$$

As we can see from 3.37 the momentum of the particle enters as a parameter to the solutions which can be found by minizing the function

$$(X_{spline_i} - X_{equation_i})^2 + (Y_{spline_i} - Y_{equation_i})^2 \quad (3.38)$$

where X_{spline_i} and Y_{spline_i} are the points taken from the first spline fit.

In the HADES experiment, due to the toroidal field, the bending of the particle is happening mainly in one plane which is the new YZ plane after rotation of the coordinate system around the Z axis by an azimuthal angle ϕ of the track. In this new coordinate system the momentum of the particle can be obtained by minimizing the simplified function which leads to 3X3 matrices instead of 5X5 in 3.38.

$$(Y_{spline_i} - Y_{equation_i})^2 \quad (3.39)$$

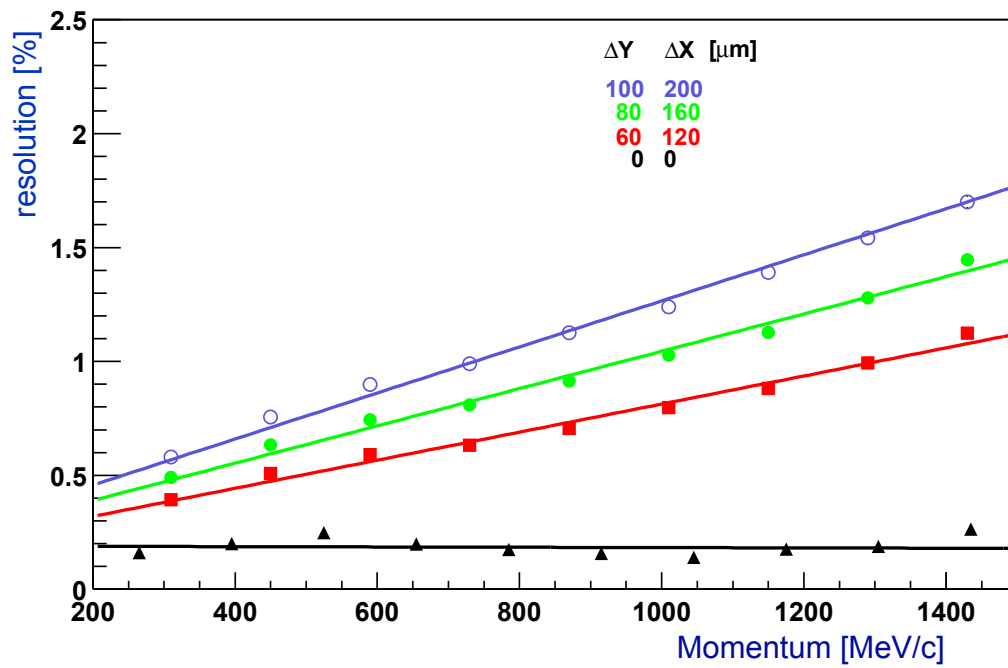
The method finds out the momentum of the particle which would move along the assumed track model. This means if the track model is far from the real trajectory of the particle, the found momentum will not be the true one. Most of the deviation from the real trajectory of the particle takes place near the magnetic coils. Therefore the reconstructed momentum differs from the real one as well. For this reason correction parameters have been calculated using simulated data. The correction parameters are created for each bin of the polar and azimuthal angles of the track. In order not to produce the correction parameters for each beam time and new version of the alignment, we introduced fixed planes as discussed at the beginning of this section.

In order to obtain the intrinsic resolution of the method, different simulation files have been generated by shooting single electrons and positrons per event into the spectrometer. The hit points were taken from Geant simulations in order to have pure momentum resolution coming from the method without influence of reconstruction resolution of the hits. In the next step hits were smeared with different resolutions from $60\mu m$ to $100\mu m$ in Y direction and from $120\mu m$ to $200\mu m$ in X direction. The obtained momentum resolution

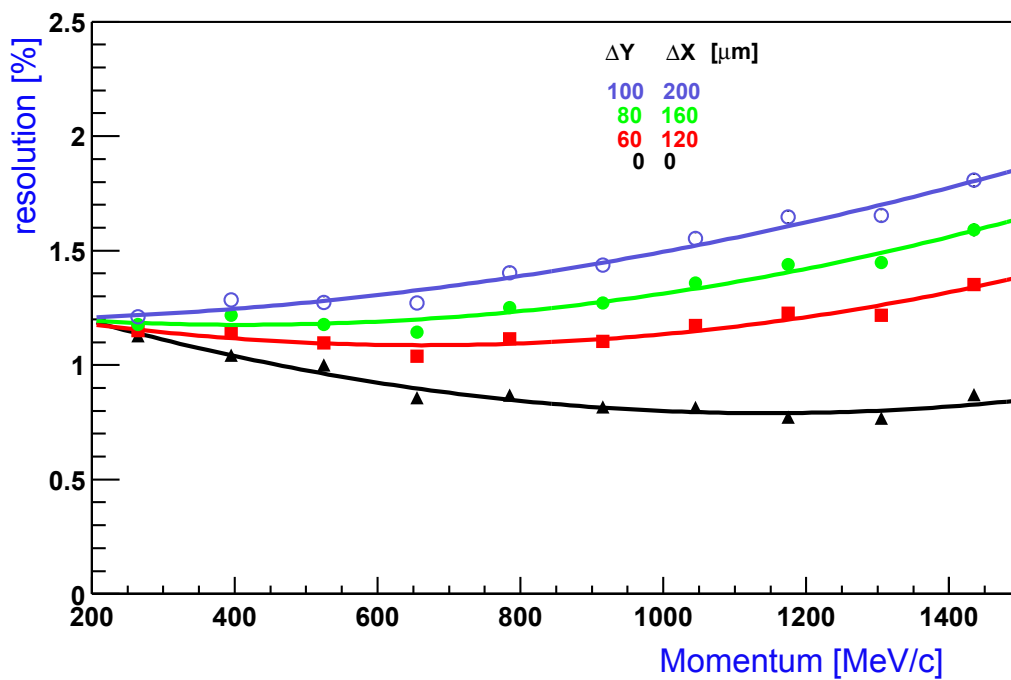
$$\frac{\frac{1}{p_{Rec}} - \frac{1}{p_{Geant}}}{\frac{1}{p_{Geant}}} \quad (3.40)$$

as a function of the momentum is presented in Figure 3.11(a). For the case where the hit points are taken without any smearing from the Geant simulation the dependance as expected is flat. When one smears the hit points the resolution is much affected for high momenta. This is because the curvature is very small for the high momenta. On the other hand, the curvature is quite high for small momenta and the change of the curvature coming from hit smearing is small compared to it.

The momentum resolution obtained is 0.2% in case of ideal hits. It changes from 0.4% to 1% as a function of momentum ranging from 200MeV to 1500MeV for the hits smeared by $60\mu m$ and $120\mu m$ in Y and X directions correspondingly.



(a) without multiple scattering



(b) with multiple scattering

Figure 3.11: Momentum resolution as a function of momentum for different resolutions of GEANT hits.

The momentum resolution in case of multiple scattering switched on for different hit resolutions is shown in Figure 3.11(b). As it is seen from the Figure the resolution ranges from 1.2% to 1.4% as the momentum changes from 200MeV to 1500MeV for the hits smeared by $60\mu m$ and $120\mu m$ in Y and X directions correspondingly. The reconstruction for the low-momentum part can still be improved if one takes into account the multiple scattering effect in the method.

3.9 Method of Runge Kutta

As was mentioned in section 3.8 for the determination of particle's momentum either the trajectory of the particle or the initial parameters should be known with high precision. In general one needs to solve a second-order field equations for the particle movement in the field. These equations can be solved using fourth order Runge-Kutta method of Nystrom in recursive way, which means each new solution is obtained from the previous one via some relations [53]. In this sense we can speak about a realistic track model along which the particle is moving.

It is clear that for solution of the second order differential equations one needs initial conditions, on the function itself and its first derivatives. All these conditions are provided by the spline method (momentum and polarity) and the track fitter (angles).

From a mathematical point of view the method searches the parameters corresponding to the minimum of the function

$$F = (m - u(\alpha))^T W^{-1} (m - u(\alpha)) \quad (3.41)$$

where m is the measured hits in the MDC chambers, $u(\alpha)$ are the intersection points of the model with the corresponding chambers (with the middle plane where the hit is defined) and α is the matrix of parameters (angles and momentum).

In our case we neglected the correlation between the parameters so the diagonal form of the error matrix was taken.

The minimization procedure is based on least squares fitting, which means solving the linear equations obtained by setting to zero the partial derivatives of the minimization function with respect to the parameters.

Although the Runge-Kutta method is exact one, it is much slower than the spline method.

Part II

Proton-proton data at 2.2GeV

In this part of this thesis the analysis procedure of the proton-proton data, and the discussion of obtained results are presented.

The first proton-proton production run was taken in January 2004. During this run a proton beam of 2.2 GeV kinetic energy with an intensity of around 10^7 particles per second was hitting the liquid hydrogen target of 5cm length. The main goal of the experiment was to investigate η meson production and its decay via two electromagnetic decay channels, $\eta \rightarrow \pi^+\pi^-\pi^0$ and $\eta \rightarrow e^+e^-\gamma$, the branching ratios of which are well known. It was also foreseen to collect data on elastic proton-proton scattering in order to investigate the spectrometer in terms of reconstruction resolution and alignment of different detector systems.

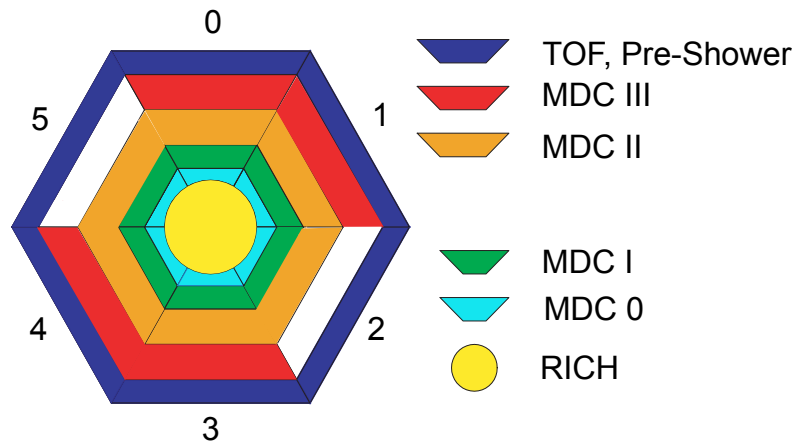


Figure 3.12: Schematic view of participating detector parts during the run. The parts with full colors correspond to operational detectors (some of them are not fully operational, for details see text), while white boxes show the missing detectors.

It was the first time when the spectrometer was fully set up in four sectors out of six. In the remaining two sectors there was one missing MDC chamber. Furthermore there were non-operational layers of the existing MDCs as well due to some problems with high voltage; two out of six layers were switched off in MDC0 sector0¹⁸, in MDC0 sector2 one layer was switched off. In sectors 2 and 5 there were only 3 MDCs existing (0,I,II). Furthermore in MDCII sector 2 two layers were switched off. Therefore the reconstruction of outer segments in this sector were made using information only from four layers which led to not fitted segments from this sector (See section 3.4). Hence the reconstruction resolution from this sector is much worse (As it is shown in the next chapter) and the background contribution is higher. In addition, during the experimental run there were several broken motherboards of MDCs which also affected the reconstruction resolution.

¹⁸In this thesis, the counting of detector parts starts from 0 in accordance with the analysis software.

The schematic picture of participating detectors during this run is shown in Figure 3.12. All the operational sub detectors are indicated with full color, while the missing parts are indicated with white boxes.

In order to enhance the reaction of interest, several 1 level trigger schemes were used for proton-proton elastic and the η decay processes. The main feature for enhancing the events from elastic scattering was the condition coming from kinematics of this process, namely the fact that outgoing protons should be in one plane (complanarity condition). Thus the condition was to require at least two charged particles in the META detectors from opposite sectors.

The first condition for the η meson was to require at least four charged particles in the META detectors, the trigger being called the MULT4 trigger. Additional conditions were set based on simulated data. Simulations show that protons are focused at small polar angles going mainly to the TOFINO detector. So, an additional condition of at least two hits in the TOFINO detector can be applied. The difference in azimuthal angles between the two outgoing protons for both decay channels of the η meson peaks at 180° showing, like in the elastic scattering channel, that the outgoing protons hit mostly opposite sectors. This additional condition on opposite sectors of the META detectors has been used. Summarizing, the 1 level trigger for the η meson reconstruction was based on at least four charged particles in the META detector, two of them being in the TOFINO region, and in addition, the opposite sector condition was required in the META detectors, called MULT4SMART trigger.

To enhance the Dalitz decay of the η meson the second level trigger (LVL2) has been used which selects the events with at least one lepton candidate according to the information from the Image Processing Units.

Not all MULT4SMART triggered events were written to the files. The triggered events were sent to the matching unit board where the decision was taken separately by two different systems which operate independently; the downscaling box and the second level trigger. All second level triggered events were written to file with the corresponding flag stored in the event header. The downscaling box scaled down the events regardless whether they contained lepton pair or not, which are called downscaled events according to the value of downscaling factor which corresponds to the number of events to be discarded between two accepted events. Later in the analysis, according to the information stored in the event header, it was possible to check whether the event was downscaled or not with a corresponding downscaling factor. The analyzed events have to be corrected for this factor in the analysis. More detailed information about downscaling and triggers is given in section 2.5.

This part of the thesis consists of three chapters:

In the first chapter the results from the elastic scattering channel will be presented. At the same time the comparison of different reconstruction methods will be shown as well, using the elastic scattering channel.

In the second chapter the results on exclusive η meson reconstruction from its two

electromagnetic decay channels, $\eta \rightarrow \pi^+\pi^-\pi^0$ and $\eta \rightarrow e^+e^-\gamma$, will be shown. The main emphasis of this analysis will be put on the estimation of the dilepton identification efficiency of the HADES spectrometer, on the investigation of η meson production and on a test of the Vector meson Dominance Model for describing the decays of the mesons.

The third chapter is devoted to the discussions of the results obtained.

Chapter 4

Elastic scattering channel

4.1 Introduction

In general, two body reactions, where two initial particles (a_{01} and a_{02}) do a transition into two final states (a_1 and a_2), are fully described by the 4-momenta of the corresponding particles (p_{01}, p_{02}, p_1, p_2), and the probability of transition can only depend on those momenta.

$$a_{01} + a_{02} \rightarrow a_1 + a_2 \quad (4.1)$$

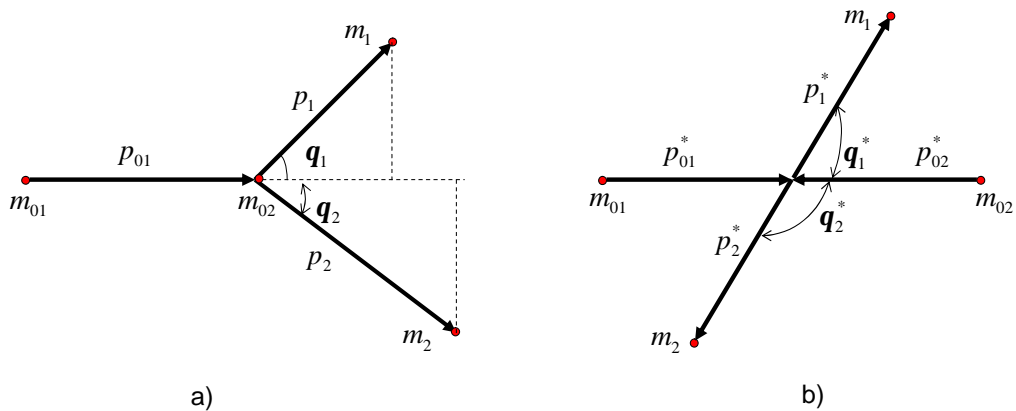


Figure 4.1: Kinematics of elastic scattering in (a) LAB system and (b) center-of-mass system of protons.

Since a transition probability is itself an invariant quantity we should take only invariant combinations made of the above-mentioned 4 momenta. From four 4-momenta one can construct 10 invariant quantities; four of them being squares of the momenta which can be

fixed as they are just masses of the particles. The remaining six parameters are reduced to two by imposing four energy-momentum conservation laws, therefore two body processes are fully described by two independent variables. One can choose these variables to be e.g. the momentum of the incoming particle and the polar angle of one of the outgoing particles.

Using kinematics of elastic scattering (see appendix B) one can obtain a tracking resolution from experimental data and test the alignment of the detector systems.

One should mention that in kinematic calculations sometimes it is convenient to represent the reaction 4.1 as going in two steps; creation and later decay of some compound particle a_0 :

$$a_{01} + a_{02} \rightarrow a_0 \rightarrow a_1 + a_2 \quad (4.2)$$

It is clear that a compound particle is at rest in the CM frame with its mass being equal to \sqrt{s} . The advantage of this notation is that it describes both the two-body decays (in this case $\sqrt{s} = E_{CM} = M$ is the total energy in the CM frame or effective mass) and the decay of unstable particle or a resonance into two particles (in this case $\sqrt{s} = m^0$ is the mass of a decaying particle with γ_{cm} being its Lorentz factor).

4.2 Results from elastic scattering

The analysis of the elastic scattering channel is started with a reaction selection based on the kinematics of the elastic scattering which imposes a restriction on polar and azimuthal angles of the outgoing protons ¹; as it is shown in Appendix B, in order to fulfill the momentum conservation, the momentum vectors of two outgoing protons should be in the same plane. Thus the distribution of the absolute value of the azimuthal angle differences should be centered at 180° as shown in Figure 4.2(a) (integrated over all sectors). As a first selection criterium the 3 sigma cut around this peak, which is fitted with a Gauss distribution, is applied. Another restriction on the polar angles can also be extracted from the kinematics of elastic scattering; the product of tangents of the polar angles of two outgoing protons should be equal to the inverse squared γ_{cm} of the center-of-mass system with respect to the laboratory system.

$$\tan \theta_1 * \tan \theta_2 = \frac{1}{\gamma_{cm}^2} \quad (4.3)$$

where γ_{cm} is the Lorentz factor of the center-of-mass system with respect to the laboratory system defined as:

$$\gamma_{cm} = \sqrt{\frac{E_{01} + m}{2m}} \quad (4.4)$$

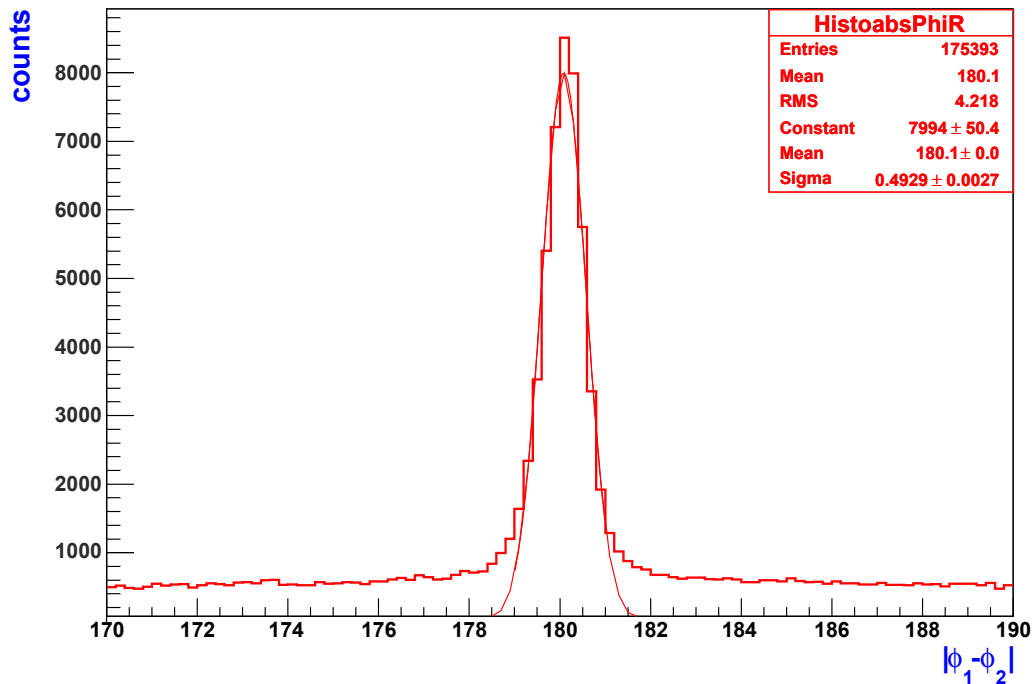
¹Only the events with opposite sector trigger have been used for elastic analysis.

with E_{01} being the total energy of the incoming proton and m stands for its mass.

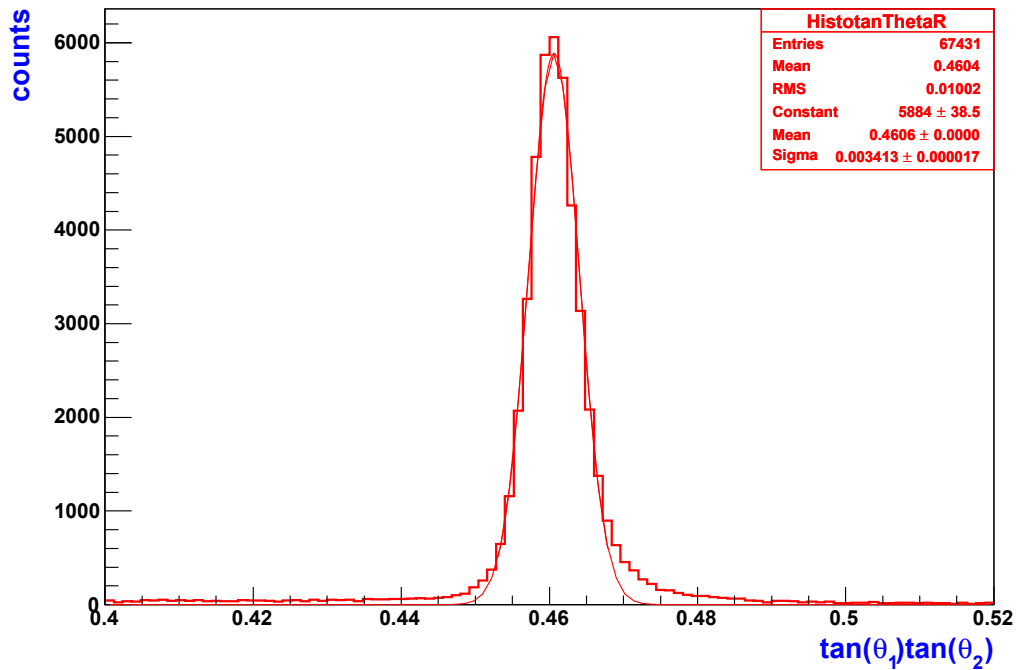
Having the beam kinetic energy of 2.2 GeV the γ_{cm} calculated with formula 4.4 equals 1.4739; therefore $1/\gamma_{cm}^2=0.4603$. The distribution of tangent product of two outgoing protons integrated over all sectors is shown in Figure 4.2(b) which is centered at the calculated value of $1/\gamma_{cm}^2$.² In order to look on how the applied cuts select the elastic scattering channel, the distribution of azimuthal angle of one proton as a function of the azimuthal angle of the second proton is plotted in Figure 4.3(a) after applying the cuts discussed before, while Figure 4.3(b) shows the reconstructed energy of one of the protons in the center-of-mass system of two protons as a function of the center-of-mass energy of the second proton. Both distributions show that the selection of elastic scattering channel is quite good. The value of the center-of-mass energy of each proton should be equal to half of the total center-of-mass energy of two protons, which is just the invariant mass of two protons being equal to 2765.83 MeV, at beam kinetic energy of 2.2 GeV.

In order to investigate possible systematics due to a misalignment of the MDC chambers, the distributions of polar and azimuthal angles are plotted for each pairs of sectors separately in Figures 4.4 and 4.5, where the green distribution is obtained using directly the values from track fitting, while the red distributions are obtained after applying the Runge Kutta algorithm for momentum reconstruction which modifies the angles as well. Systematic deviations can be seen in all pairs of sectors, both for the track fitting and after application of the Runge Kutta method, but in all sectors there is an improvement of widths with respect to the track fitting after application of the Runge Kutta method. The main discrepancy between track fitting and Runge Kutta method is for sector pairs 0-3, as is seen from Figures 4.4 and 4.5, which is mainly connected to the fact that in this sectors there were several not-operational layers of MDCs. In sectors 1-4 the distributions are systematically shifted, both for Runge Kutta and track fitting, while the widths of the distributions are improved for the Runge Kutta case.

²note that this distribution is plotted after applying a cut of 3 sigma around the peak in the distribution of the differences of absolute values of the azimuthal angles of the two protons.

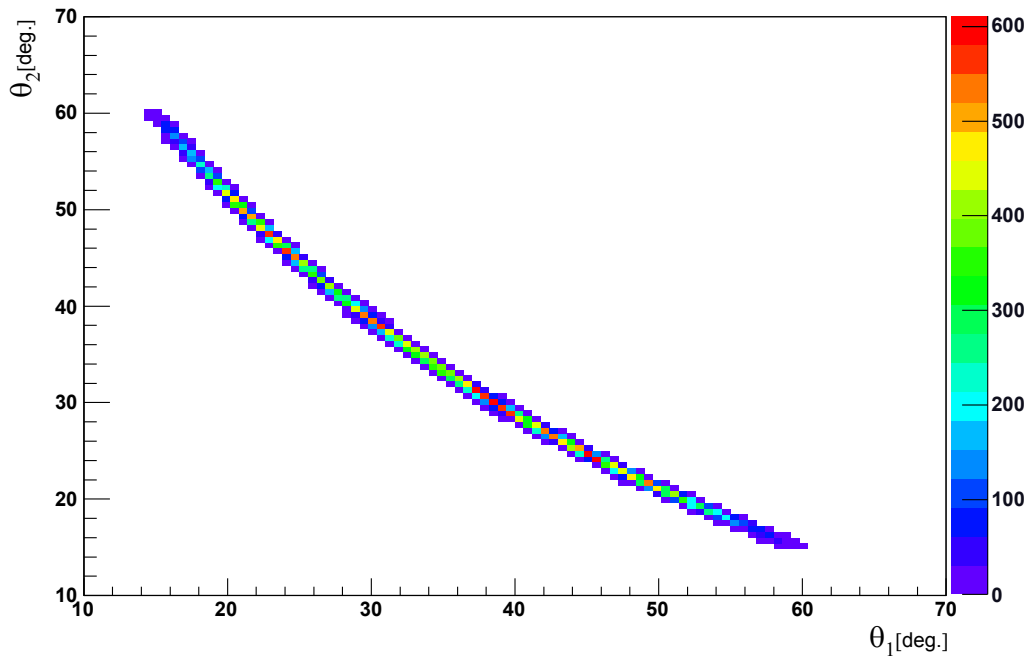


(a) Distribution of the absolute value of azimuthal angle differences of the outgoing protons

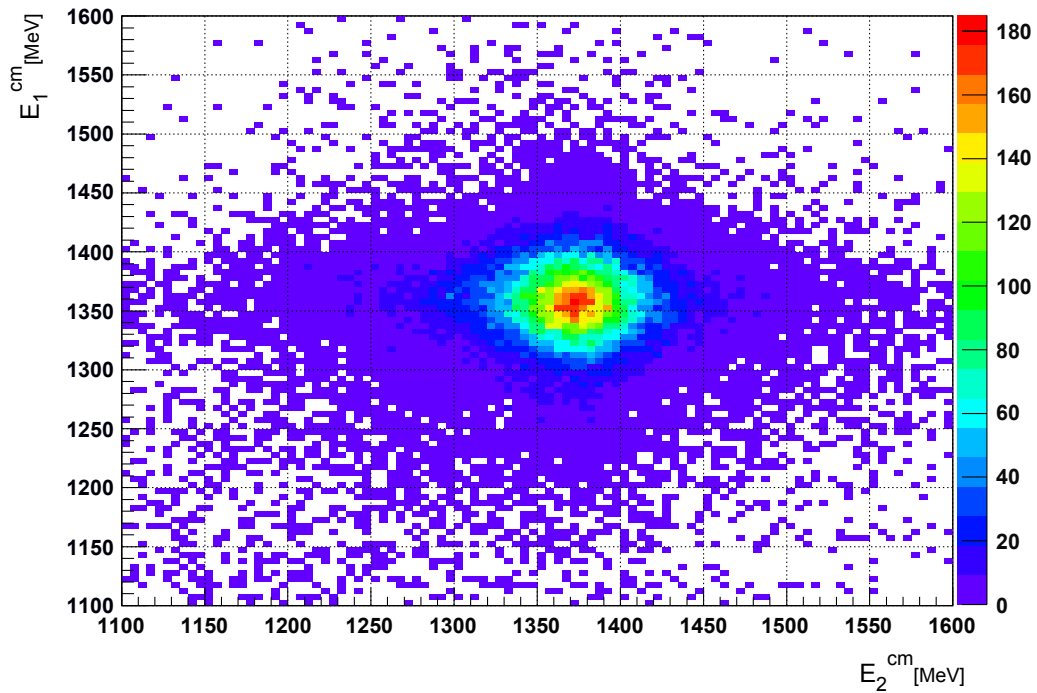


(b) the distribution of products of tangents of polar angles of two outgoing protons

Figure 4.2: The distributions used to select the elastic scattering channel. $3 * \sigma$ cuts around peaks in (a) and (b) have been used.



(a) The polar angle of one of the outgoing protons as a function of another one



(b) Center of mass energy of one of the outgoing protons as a function of another one. Both protons should have the same values of the energy being equal to the half of the total center of mass energy

Figure 4.3: The distributions showing the quality of elastic channel selection.

For the sectors with 3 MDC chambers (2-5) there is no improvement after application of the Runge Kutta method and both distributions are systematically shifted (See Figure 4.5).

The width and the systematic shift of angular distributions will affect the momentum resolution as well; as the spline method uses the angular information from the track fitter, the systematic shifts as well as the broad width of the angular distributions from track fitting will affect the reconstructed momentum in terms of resolution and systematic shifts as well.

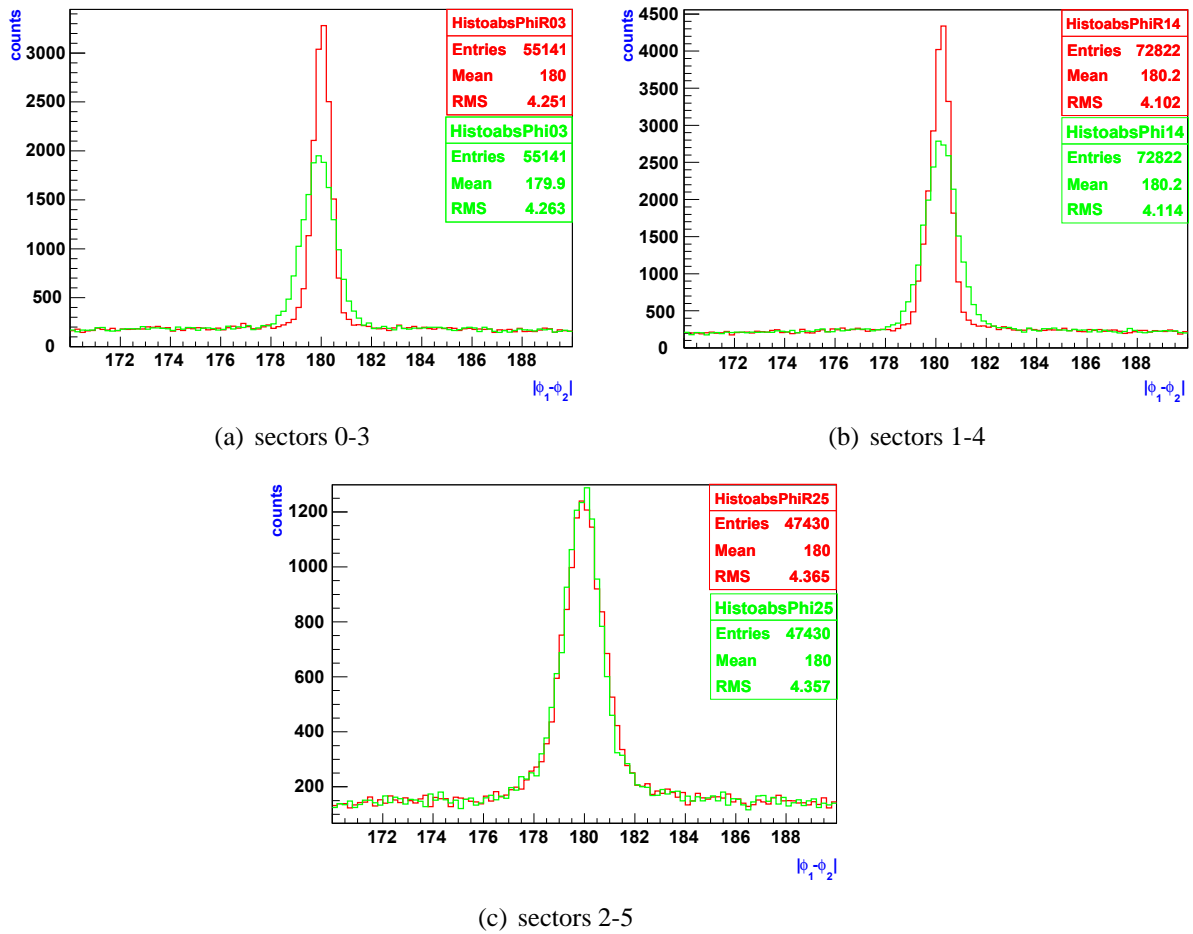


Figure 4.4: Distribution of the absolute value of azimuthal angle differences of protons for each pair of opposite sectors.

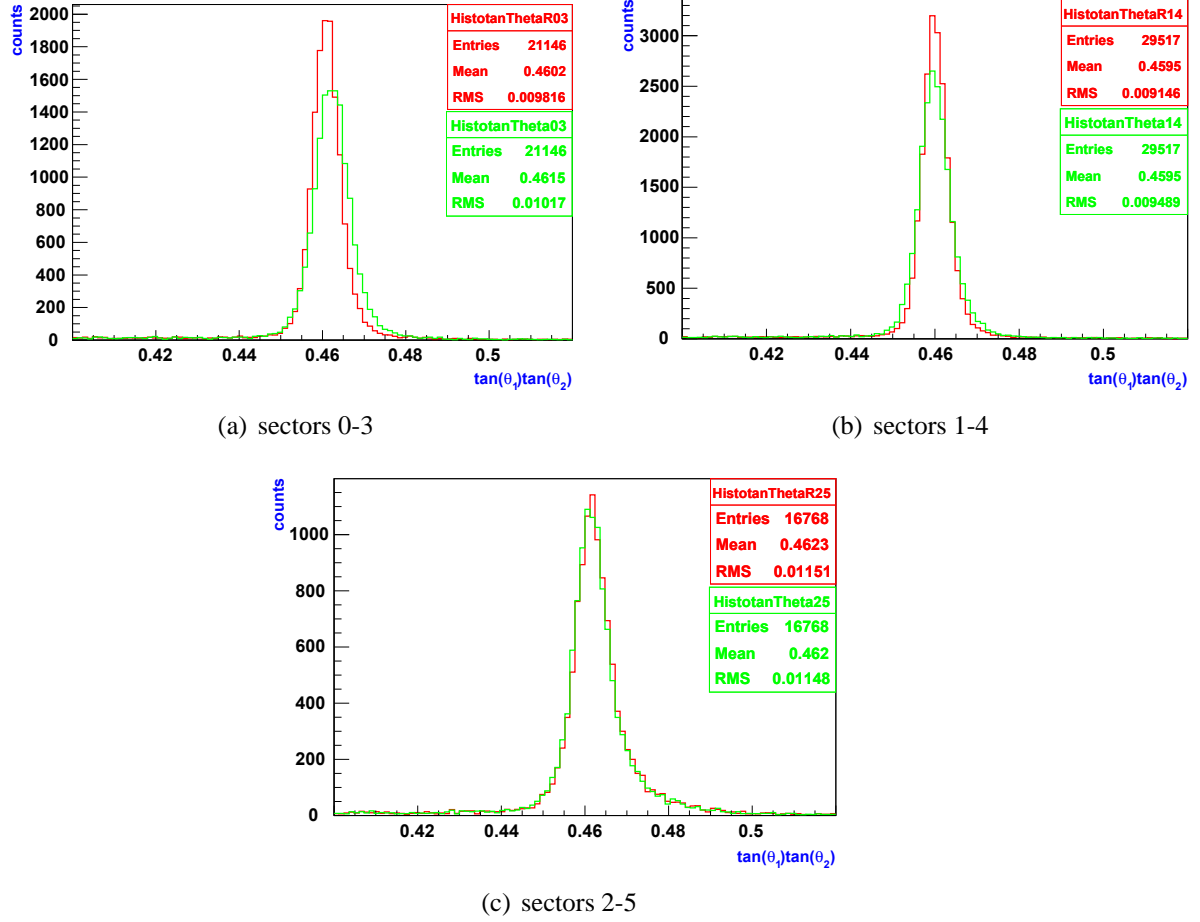


Figure 4.5: Distribution of polar angle products of two protons for each pair of opposite sectors.

The momentum of the track in elastic scattering can be calculated by measuring the polar angle of the track by:

$$p_{\text{calculated}} = \frac{p_{\text{beam}}}{\cos(\theta) [1 + \tan^2(\theta) \gamma_{cm}^2]} \quad (4.5)$$

with γ_{cm} defined in formula 4.4

Figure 4.6 shows the resolution of the momentum reconstruction for each sector defined as:

$$\text{resolution} = \frac{\frac{1}{p_{\text{reconstructed}}} - \frac{1}{p_{\text{calculated}}}}{\frac{1}{p_{\text{calculated}}}} \quad (4.6)$$

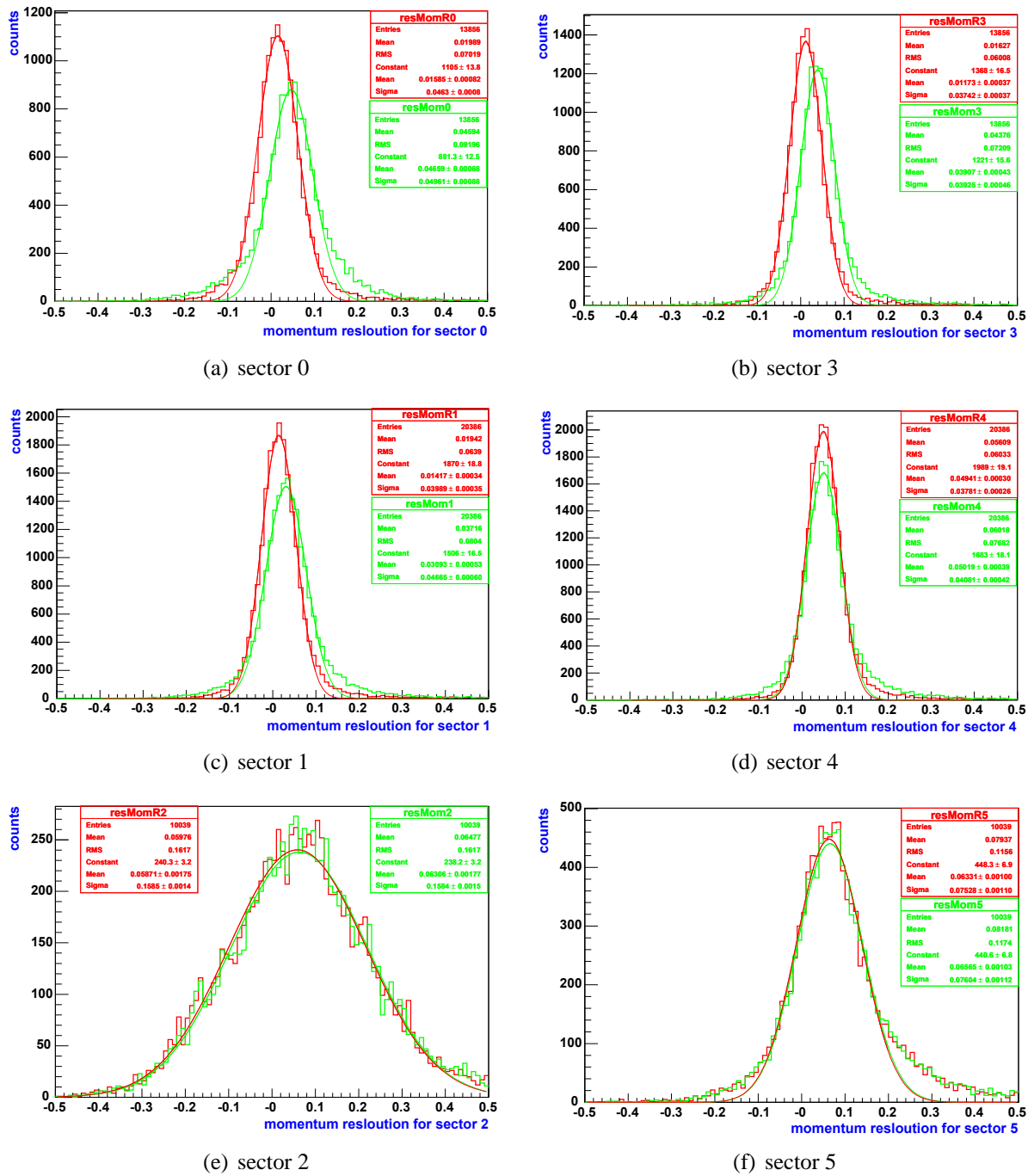


Figure 4.6: The momentum resolution obtained for each sector using elastic scattering for spline(green) and Runge Kutta (red) methods. The resolution is defined as

$$\frac{\frac{1}{P_{\text{reconstructed}}} - \frac{1}{P_{\text{calculated}}}}{\frac{1}{P_{\text{calculated}}}}$$

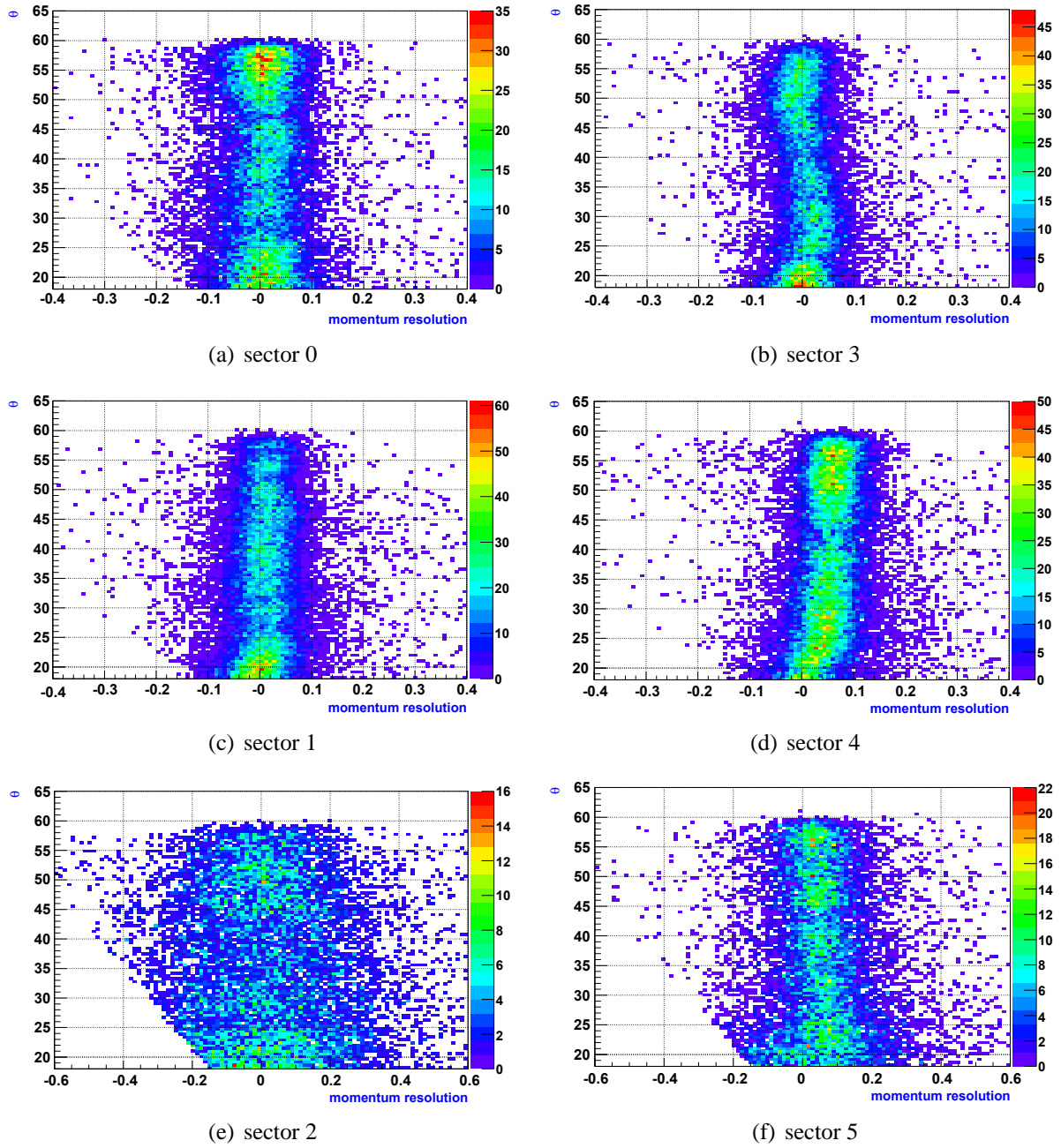


Figure 4.7: The momentum resolution as a function of polar angle obtained for each sector using elastic scattering for the Runge Kutta method. The resolution is defined as

$$\frac{1}{p_{\text{calculated}}} \left(\frac{1}{p_{\text{preconstructed}}} - \frac{1}{p_{\text{calculated}}} \right)$$

Tables 4.1 and 4.2 summarizes the obtained momentum reconstruction resolutions and systematic shifts from the spline and Runge Kutta methods ³.

momentum reconstruction resolutions σ [%]						
	sector 0	sector 1	sector 2	sector 3	sector 4	sector 5
spline	5	4.7	16	3.9	4	7.6
Runge Kutta	4.6	4	16	3.7	3.8	7.6

Table 4.1: Momentum resolution from spline and Runge Kutta, obtained for each sector using elastic scattering.

systematic shifts in momentum reconstructions [%]						
	sector 0	sector 1	sector 2	sector 3	sector 4	sector 5
spline	4.6	3	6.3	3.9	5	6.5
Runge Kutta	1.6	1.4	6.3	1.1	5	6.5

Table 4.2: Systematic shifts in momentum reconstruction for spline and Runge Kutta for each sector.

The observed large systematic shift for the spline is connected to the systematic shift for angles plotted in Figures 4.4 and 4.5. In sector 4 there is a systematic shift of 5%, both for spline and Runge Kutta methods correlated with the systematic shifts of angles which is not improved for Runge Kutta method as well (Figures 4.4 and 4.5).

For the sectors with 3 MDC chambers there is no improvement after applying a Runge Kutta method. The overall systematic shift of the momentum resolution is partly connected with the fact that the reconstructed momenta are not corrected for energy loss. It is clear that the obtained resolution is not pure momentum resolution but is affected with angular resolution as well since the theoretical momentum is calculated by measuring a polar angle.

Figure 4.7 shows the momentum resolution as a function of polar angles for each sector.

As it is seen from the distributions for momentum resolutions (Figures 4.6 and 4.7) there are still some problems connected to probably with misalignment, as it depends on sectors.

³It should be noted that all momentum resolutions are plotted for the momentum regions below 2.5 GeV because of systematic shift in this region of momentum as well as its broadening due to the problems with low polar angles as for the high momentum protons in elastic scattering the corresponding polar angles are small. In general the momentum resolution should be estimated as a function of momentum.

Chapter 5

Exclusive η meson reconstruction

5.0.1 Introduction

In the quark model all mesons are bound states of quark and anti- quark [54, 55, 56]. When we combine two particles with isospin $I = \frac{1}{2}$, we obtain an iso-triplet ¹

$$\begin{aligned} |1 \ 1\rangle &= -u\bar{d} \\ |1 \ 0\rangle &= (u\bar{u} - d\bar{d}) / \sqrt{2} \\ |1 \ -1\rangle &= d\bar{u} \end{aligned} \quad (5.1)$$

and iso-singlet.

$$|00\rangle = (u\bar{u} + d\bar{d}) / \sqrt{2} \quad (5.2)$$

In the language of group theory we can say that u and d quarks form the fundamental representation of SU(2) isospin symmetry [54]. It is a mathematical copy of spin in that the isospin generators satisfy the same algebra like spin. The triplet 5.1 and singlet 5.2 decomposition in this language can be written us:

$$2 \otimes \bar{2} = 3 \oplus 1 \quad (5.3)$$

In case of pseudoscalar mesons (when quarks spins are anti- parallel) the triplet is the pion; for vector mesons (spins are parallel) it is the ρ meson. By combining a third quark s (therefore introducing the second additive quantum number S, in addition to I_3) it was natural to enlarge isospin symmetry to a larger group, namely, a SU(3) group (with rank 2). With the analogy to 5.3 we can decompose now the product of fundamental representation and a conjugate one of SU(3) as a sum of octet and singlet representations [56, 57]:

¹We use a "ket" notation where $|I \ I_3\rangle$ means that the particle is in a state with isospin I and its third component is equal to I_3 . In general the product of two states $|j_1 \ m_1\rangle \times |j_2 \ m_2\rangle$ can be constructed according to $|JM\rangle = \sum \langle j_1 m_1 j_2 m_2 | JM \rangle |j_1 m_1\rangle |j_2 m_2\rangle$ where $\langle j_1 m_1 j_2 m_2 | JM \rangle$ are called Clebsch-Gordan coefficients.

$$3 \otimes \bar{3} = 8 \oplus 1 \quad (5.4)$$

The illustration of the pseudoscalar nonet (an octet plus a singlet) is shown in Figure 5.1

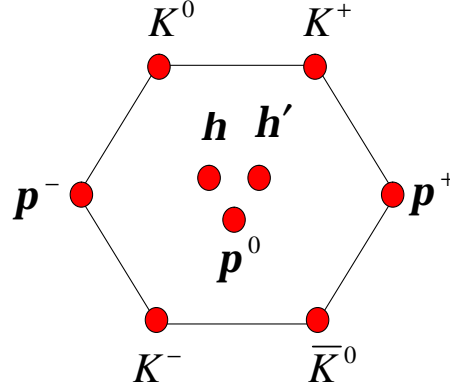


Figure 5.1: A nonet of pseudoscalar mesons.

As we have two isospin 0 states, the iso-singlet combination 5.2 and the $s\bar{s}$, their superposition should correspond to an η_8 and η_0 (or φ_8 and φ_0):

$$\begin{aligned} \eta_8 &= \frac{u\bar{u} + d\bar{d} - 2s\bar{s}}{\sqrt{6}} \\ \eta_0 &= \frac{u\bar{u} + d\bar{d} + s\bar{s}}{\sqrt{3}} \end{aligned} \quad (5.5)$$

where η_8 and η_0 are octet and singlet states.

From the last equation it can be seen that η_0 treats u, d, and s quarks symmetrically and is unaffected under SU(3) transformations while the η_8 transforms as a part of the SU(3) octet whose other members are pions and kaons. As these two states have the same quantum numbers, in practice they tend to mix. In fact the observed pseudoscalar mesons η and η' are linear combinations of the octet and the singlet pseudoscalar η_0 and η_8 states.

$$\begin{aligned} \eta &= \cos(\Theta)\eta_8 - \sin(\Theta)\eta_0 \\ \eta' &= \sin(\Theta)\eta_8 + \cos(\Theta)\eta_0 \end{aligned} \quad (5.6)$$

where the Θ is the mixing angle.

The mixing angle can be calculated using the Gell-Mann-Okubo mass formula for the pseudoscalar meson multiplet [56]

$$m_\eta^2 = \frac{4}{3}m_K^2 - \frac{1}{3}m_\pi^2 \quad (5.7)$$

together with 5.6 which gives $\theta = -11^\circ$. However there are other approaches for calculating this angle giving slightly different values [58, 59, 60]. Consequently the mixing angle is known with low precision and ranges between -10° and -23° .

One should mention that in case of ideal mixing the η meson would consist of non strange quarks only and η' would just be the $s\bar{s}$ combination.²

The η meson has only electromagnetic decay channels, and even not all of them are possible [1]³⁴.

In this chapter the reconstruction procedure of the η meson from its two decay channels $\eta \rightarrow \pi^+\pi^-\pi^0$ and $\eta \rightarrow e^+e^-\gamma$, the branching ratios of which are well known, will be presented.⁵

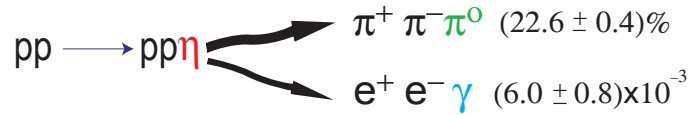


Figure 5.2: Decay channels of the η meson with well known branching ratios studied in this work.

This investigation can schematically be divided into several steps [61]:

- Estimation of the dilepton identification efficiency of the HADES spectrometer.
- Study of the η meson production.

²In case of vector mesons the mixing angle is known more precisely and it is close to ideal mixing, therefore the observed ϕ and ω states are just $s\bar{s}$ and $(u\bar{u}+d\bar{d})/\sqrt{2}$ combinations correspondingly.

³The electromagnetic channel $\eta \rightarrow \pi^0 e^+ e^- (\pi^0 \gamma)$ is forbidden by C parity.

⁴The decay channel $\eta \rightarrow \pi^+\pi^-\pi^0$ could look like strong decay, but it is forbidden by G parity conservation.

⁵Decay modes of the η [$I^G (J^{PC}) = 0^+ (0^{-+})$] meson

decay mode	$\frac{\Gamma_i}{\Gamma}$
2γ	$(39.43 \pm 0.26)\%$
$3 \pi^0$	$(32.51 \pm 0.29)\%$
$\pi^0 2\gamma$	$(7.2 \pm 1.4) \times 10^{-4}$
$\pi^+\pi^-\pi^0$	$(22.6 \pm 0.4)\%$
$\pi^+\pi^-\gamma$	$(4.68 \pm 0.11)\%$
$e^+e^-\gamma$	$(6.0 \pm 0.8) \times 10^{-3}$
$\mu^+\mu^-\gamma$	$(3.1 \pm 0.4) \times 10^{-4}$
e^+e^-	$< 7.7 \times 10^{-5}$
$\mu^+\mu^-$	$(5.8 \pm 0.8) \times 10^{-6}$
$e^+e^-e^+e^-$	$< 6.9 \times 10^{-5}$
$\pi^+\pi^-e^+e^-$	$(4.0_{-2.7}^{+14.0}) \times 10^{-4}$
$\pi^+\pi^-2\gamma$	$< 2.0 \times 10^{-3}$
$\pi^+\pi^-\pi^0\gamma$	$< 5. \times 10^{-4}$
$\pi^0\mu^+\mu^-\gamma$	$< 3. \times 10^{-6}$

- Test of the Vector meson Dominance Model for meson decays.

For the dilepton identification efficiency the following procedure is used:

1. Reconstruction of η mesons from the 3-pion and the Dalitz decays for simulation and experiment, respectively, thus obtaining the numbers: N_{had}^{sim} , N_{Dalitz}^{sim} , N_{had}^{exp} , N_{Dalitz}^{exp} .
2. Having done the first step we can now calculate

$$Ratio = \frac{R_{Exp}}{R_{Sim}} \quad (5.8)$$

where

$$R_{Exp} = \frac{N_{had}^{Exp}}{N_{Dalitz}^{Exp}} \quad (5.9)$$

$$R_{Sim} = \frac{N_{had}^{Sim}}{N_{Dalitz}^{Sim}}$$

are the ratios of reconstructed η mesons from the 3-pion and Dalitz decays correspondingly for experimental data and simulation.

3. From equation 5.8 we can estimate the dilepton identification efficiency of the HADES spectrometer.

Note that we can not directly compare the obtained ratio from experimental data R_{Exp} (Equation 5.9) to the known relative branching ratios. The reason for this is that the branching ratios are obtained in full phase space. Because the two decay channels have a different phase space distribution, they will be cut in different ways inside the HADES acceptance, consequently the relative branching ratios will be different from those listed in Figure 5.2.

In order to investigate the production mechanism of the η meson the reconstructed experimental angular distributions will be compared with those obtained from simulation.

For testing of the Vector meson Dominance Model the reconstructed invariant mass of e^+e^- pairs from the η Dalitz decay will be compared with that obtained from model calculations.

5.1 Meson production in NN collisions

There is a general consensus in theory that in NN collisions the η meson is produced in a two step process, where, in the first stage, pseudoscalar or vector mesons exchanged between the colliding nucleons excites them.

Excited states of the nucleon are called nucleon resonances. States with isospin $I = 3/2$ are called Δ resonances, states with isospin $I = 1/2$ are called N^* states.

The states are characterized in the following nomenclature: $L_{2I2J}(W)$ where L is the orbital angular momentum of the nucleon-pion (or other pseudoscalar meson) pair from the decay of the resonance in spectroscopical notation. I and J are isospin and total angular momentum of the resonance and W stands for its pole mass.

All nucleon resonances can decay to the nucleon ground state via the strong interaction by emission of mesons. The usual spin-isospin selection rules apply, so e.g. the Δ resonance ($I = 3/2$) can decay to the nucleon ground state ($I = 1/2$) via the emission of pions ($I = 1$), but not via the emission of η mesons ($I=0$), while both decays are possible for the S_{11} ($I=1/2$) state.

In the framework of the constituent quark model the simplest excitations of the nucleon are described by a spin-flip or an orbital excitation of one quark. The wave functions are composed of space, spin, flavor and color parts. In the simplest model, the constituent quarks are put in a harmonic oscillator potential with additional spin-spin and spin-orbital dependent interactions. Figure 5.3 shows the ground state of the nucleon in such a model.

The $P_{33}(1232)$ is produced via the parallel alignment of all three quark spins as shown in Figure 5.4(a). This state would be degenerate with the nucleon ground state if only the oscillator potential is considered but the two states are split by the spin-spin interaction. The other resonances arise from the excitation of one quark into the $L = 1$, p shell, as shown in Figure 5.4(b).

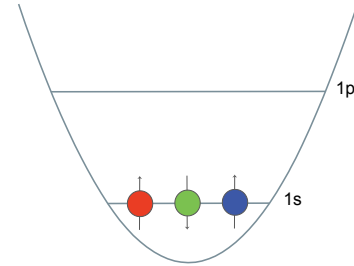


Figure 5.3: Ground state of a nucleon.

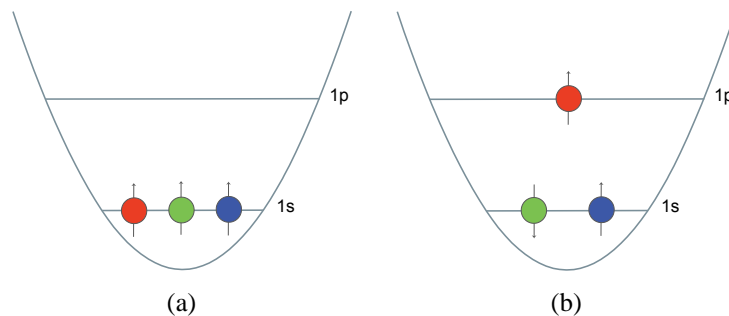


Figure 5.4: Excited state of a nucleon, via spin flip (a) corresponding to P_{33} and orbital excitation (b) corresponding to S_{11} or D_{13} .

The $S_{11}(1535)$ resonance seems to play an important role as an intermediate state for the $pp \rightarrow pp\eta$ reaction [62]. This behavior is not yet understood and gave rise to many discussions about the structure of this state. Apart from the resonance currents, different models take into account the production via other mechanisms like nucleonic currents [63, 64], direct production [65, 66] or mesonic currents [64] (See Figure 5.5).

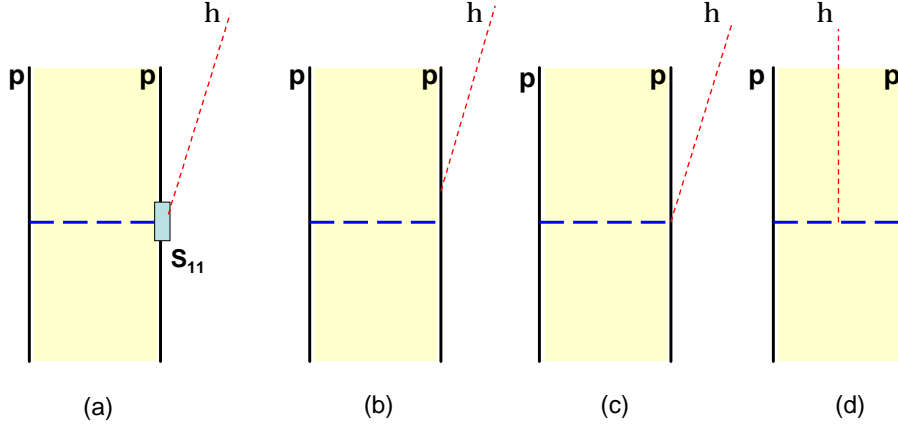


Figure 5.5: Production mechanisms of η mesons in NN collisions a)resonance decay b)hadronic current c)direct decay d)mesonic fusion.

However, there are some ambiguities regarding the particular contribution from the individual mesons. While in the references [67, 68] the largest contribution is due to a virtual ρ meson exchange, the authors of [69] predict the highest amplitude for the π meson exchange.

5.2 Simulation

As was mentioned at the beginning of this chapter, in order to estimate the dilepton identification efficiency of the HADES spectrometer and investigate the production and decay mechanisms of the η mesons we need a simulation. Different types of simulated data have been generated: a full cocktail simulation and simulations containing only η mesons with its subsequent 3-pion or Dalitz decay.

Simulations are an integral part of experimental programs associated with scattering experiments and particle accelerators. Such studies are required both in order to understand the properties of experimental setups, as well as to gain insight into the processes of interest, so that relevant experiments may be optimized and experimental spectra may be interpreted. The simulation procedure starts with an event generation. For proton-proton simulations a full cocktail was generated according to most of the known physical processes using the PLUTO software [70, 71]. PLUTO is a collection of C++ classes, added up to the framework of a simulation package for hadronic-physics reactions. The output can be analyzed online or further processed with HGEANT [72]. The package includes models for resonance and Dalitz decays. A decay-manager interface enables multi-step (cocktail) calculations. The branching ratios and decay channels are set by the user, according to values known from experiment or from theoretical calculations. Table 5.1 shows the processes included for proton proton simulations.

reaction	cross section [μb]
$pp \rightarrow pp$ (elastic)	18.0
$pp \rightarrow n\Delta^{++}$	10.8
$pp \rightarrow p\Delta^+$	3.6
$pp \rightarrow pN(1440)$	2.8
$pp \rightarrow pp\pi^0$	0.15
$pp \rightarrow pn\pi^+$	1.0
$pp \rightarrow p\Delta^+\pi^0$	0.48
$pp \rightarrow n\Delta^{++}\pi^0$	2.0
$pp \rightarrow pN(1440)\pi^0$	2.36
$pp \rightarrow pp\pi^0\pi^0\pi^0$	0.15
$pp \rightarrow p\pi^+\pi^-\pi^0$	0.33
$pp \rightarrow pn\pi^+\pi^+\pi^-$	0.6
$pp \rightarrow pN^*(1535)$ (inclusive)	0.31

Table 5.1: Processes included in cocktail simulation.

For the 3-pion decay of the η meson only phase space production was assumed, while for the Dalitz decay the Vector Dominance Model was used. The production of the η meson was assumed through nucleon excitation to the $N^*(1535)$ state and its subsequent decay to the nucleon with emission of the η meson. For pure η simulations the matrix element of η production measured by the DISTO experiment was taken [10, 11].

After event generation the events are read by the HGeant [72] package based upon the GEANT [73] program from CERN, which tracks the particles through the spectrometer. It is possible to describe the experimental setup by a structure of geometrical volumes and the corresponding material composition. This is implemented in HGeant, which in turn uses it to simulate the different effects affecting particles passing through detector volumes. In the next step Geant hits are digitized i.e. hit positions are converted into observables similar to what is obtained in experimental runs. The hit digitization consists of several algorithms which simulate the electronic response of each detector component, by taking into account resolution smearing, electronic noise, and most of the effects which play a role in the analogue-to-digital conversion procedure. The digitizer's output looks exactly like a calibrated signals from the detector which can be analyzed with the standard algorithms used to analyze experimental data.

5.2.1 Reaction parametrization

In general for the full description of the three particle system after particle identification and four momentum conservation we are left with 5 parameters ($12-4-3=5$). The square of invariant masses of the proton- η system $p_1\eta$ and $p_2\eta$, respectively, (the Dalitz parameters) constitute a natural choice for the study of the interaction within the $pp\eta$ system. This is

because by investigating the population of the surface defined by these two variables one can study the interaction mechanism between those particles.

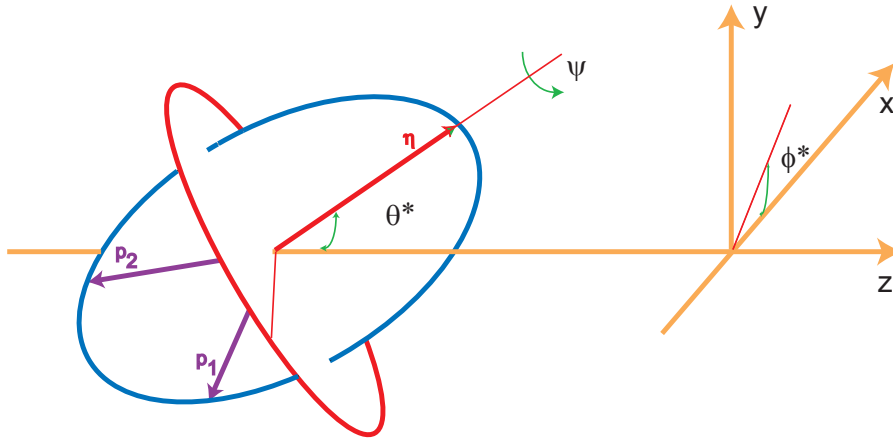


Figure 5.6: Parameters describing η meson production.

Due to the momentum conservation law, the momentum vectors of the particles are lying in one plane, as shown in Figure 5.6, often referred to as the emission, reaction or decay plane. The remaining 3 parameters must define an absolute orientation of the emission plane. This may be realized for example by defining the orientation (θ^*, ϕ^*) for the momentum of the arbitrarily chosen particle in the center-of-mass frame e.g. the η meson and the angle which describes the rotation ψ around the direction fixed by that particle as shown in Figure 5.6.

For our purpose the angles have been chosen as polar and azimuthal angles of the η meson in the center-of-mass frame of protons as shown in Figure 5.6, while the third angle was chosen in a different way describing the orientation of the two proton plane θ_p in the center-off-mass frame of two outgoing protons. Taking into account rotational symmetry of the beam axis one can integrate over the ϕ^* angle and be left with only two angles. It has been checked with simulation that the remaining two angles are almost independent, thus allowing us to compare 1 dimensional distributions without having to create a multi-dimensional acceptance correction.

5.3 Analysis Strategy

The usual way of resonance identification consists of several steps [74]:

- Identification of background events.
- Reconstruction of invariant mass of decay products after excluding the background events.

Because of the fact that we are unable to detect all decay products (there are neutral particles among them) we will follow the indirect way of resonance identification based on the missing-mass distributions.

The reaction channels studied here contained at most one unmeasured particle in the final state, thus measured events with four tracks were kinematically complete. The reconstruction procedure consists of the following steps:

1. Event selection and particle identification.
2. Removal of fake tracks.
3. Reaction selection.

5.3.1 Event selection and particle identification

As a first selection criterium only the events with at least one negative and three positive tracks were taken. In this step every track is marked with the corresponding flags according to a fake removal strategy described in the next section.

The negative particle was assumed to be an e^- if there was a matching with the signal from the *RICH* detector or π^- in the other case. As we do not know beforehand which of the positively charged tracks corresponds to a proton and a π^+ or e^+ , we create different candidates taking each time one of the positively charged tracks to be a π^+ or e^+ as shown in Figure 5.7. In this Figure each row is taken as a candidate for the next analysis steps. The combinations presented in Figure 5.7 correspond to the case when there are exactly three positive and one negative particles. In general, there can be of course more tracks coming from physics processes and fake tracks as well.

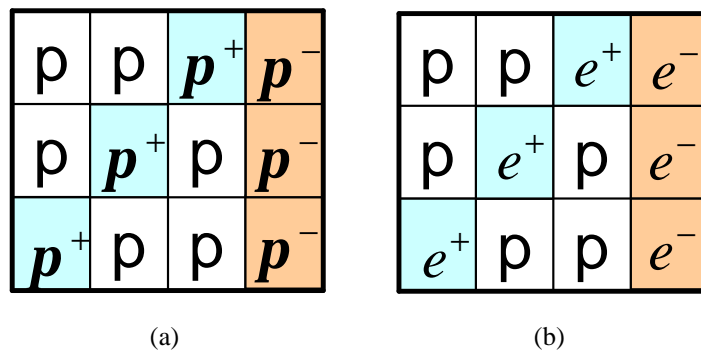


Figure 5.7: Candidates created from an event in the case of exactly 3 positive and one negative particles (a) for the 3 pion final state (negative particle is assumed to be π^-) and (b) for the Dalitz decay (the negative particle is assumed to be e^-).

As it is seen from Figure 5.7, we have created 3 candidates corresponding to each row. Obviously only one of them is correct where the assumption made on particles corresponds to reality. In other words, in order to remove two of the three combinations we need a particle identification.

For hadron identification the correlation between momentum and β of the track was used. The left side of Figure 5.8 shows the momentum times polarity as a function of velocity of a particle in experimental data, for events where the start time was reconstructed from a negative pion ⁶, while the right side shows the same correlation with the negative particle being identified as an electron this time. Each combination created above should fulfill the condition based on graphical cut as shown in Figure 5.8, e.g. for the first candidate from Figure 5.7 the protons and pions should be inside the corresponding graphical cut presented in Figure 5.8, otherwise that candidate is removed from the list. The used cuts are taken quite broad in order not to lose statistics and furthermore the lepton identification was done without imposing conditions on the ring quality in the *RICH* detector and without detecting electromagnetic showers in the *SHOWER* detector. Most of the misidentified particles will be removed by a kinematic condition applied afterwards.

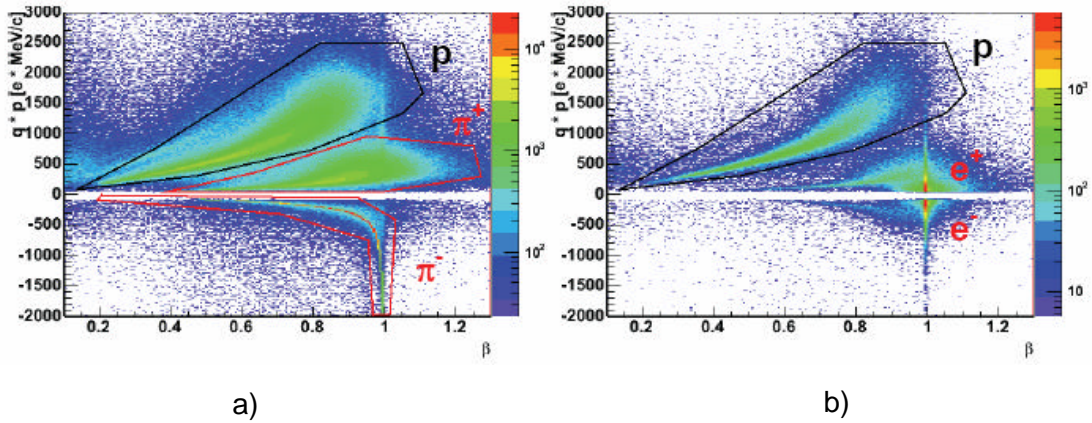


Figure 5.8: Graphical cuts used for particle identification: a) for 3 pion final state and b) for the Dalitz decay of the η meson.

⁶As this data was taken without start detector, the start time of the reaction was reconstructed using an algorithm based on assigning a theoretically calculated time of flight to the identified particle (See Section 2.1).

5.3.2 Removal of fake tracks

Due to the broad matching windows fake tracks can contribute to the list of created tracks which are schematically shown in Figure 5.9.

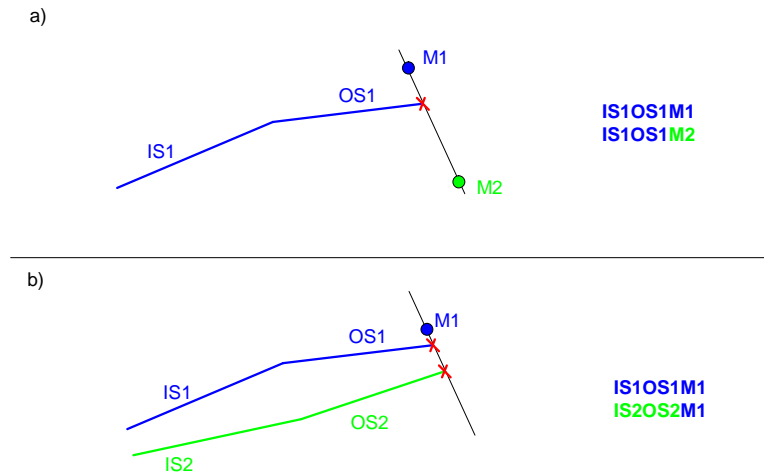


Figure 5.9: Strategy for removing fake META candidates when (a) one track candidate is matched with two different META hits and (b) two track candidates are matched with the same META hit (See text for details).

Examples of the fake candidates:

- a) The same track candidate is matched with two different *META* hits. The blue and green circles are reconstructed *META* hits while the red crossing is the intersection point of the outer track segment with the *META* detector. In this case we have 2 fully reconstructed tracks, denoted as IS1OS1M1 and IS1OS1M2 instead of one. The track which has a minimum matching quality parameter (See section 3.6) is marked as a "good" one, while the other is marked as a "meta fake".
- b) Two different track candidates are matched with the same *META* hit. Like in case (a) the track with the minimum value of the matching quality parameter is marked as a "good" one, while the other is kept with a "meta fake" flag.

Apart from the "meta fakes" described above, there can also be fake tracks coming from mismatching between inner and outer tracks reconstructed in the corresponding MDCs before and after the *MAGNET*. Figure 5.10 schematically shows this phenomenon. These fakes we call "track fakes" and the procedure of selecting the "good" tracks is based on quality parameters, as in case of "meta fakes", describing the corresponding matching.

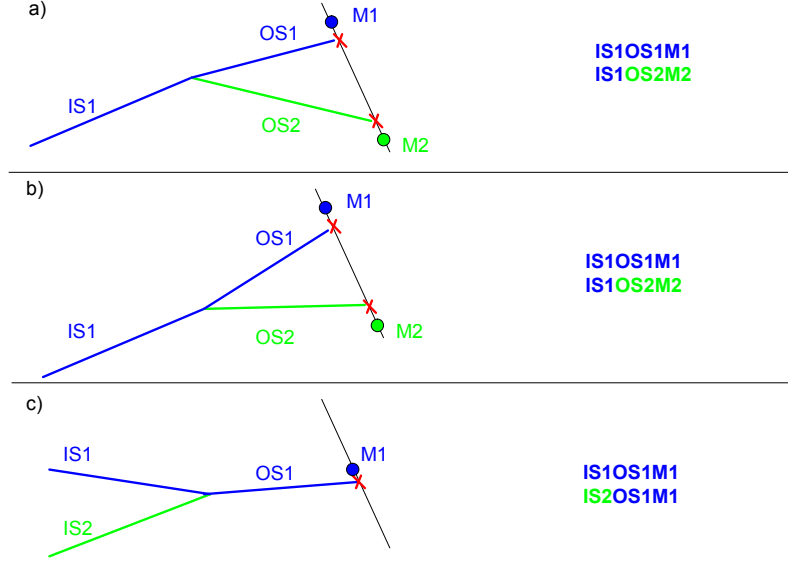


Figure 5.10: Strategy for removing fake track candidates when (a) one inner segment is matched with two outer ones, (b) like in case (a), but tracks have different polarity and (c) two inner segments are matched with one outer segment.

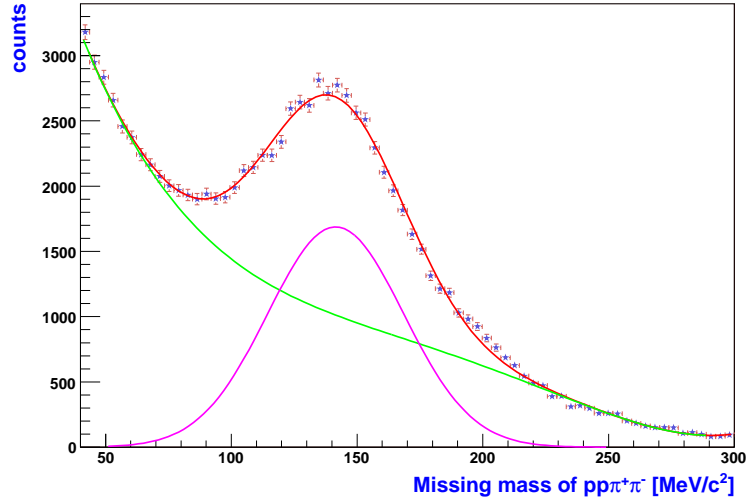
5.3.3 Reaction selection

After the first step of particle identification there is still one unidentified particle: the neutral pion in the 3-pion final state decay and the photon in the Dalitz decay. Missing-mass analysis was used to determine the rest mass of an unobserved particle. In the LAB system, the missing mass (M_{miss}) is given by the following formula:

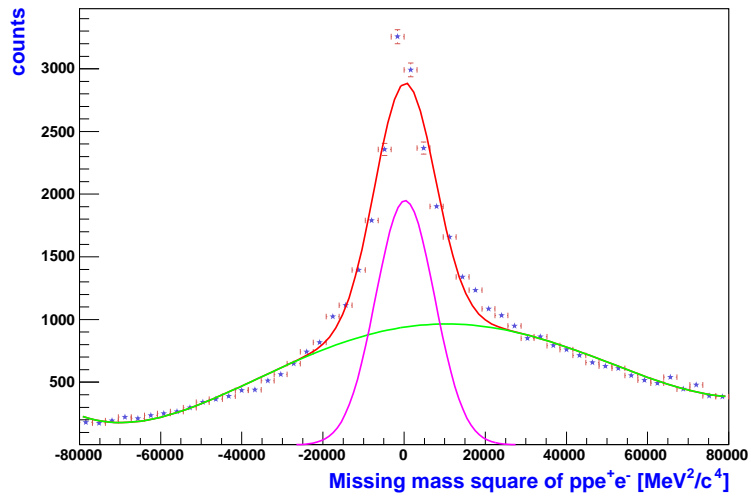
$$(M_{miss})^2 c^4 = \left(E_{beam} + M_p c^2 - \sum E_i \right)^2 - c^2 \left(\vec{p}_{beam} - \sum \vec{p}_i \right)^2 \quad (5.10)$$

where the index i runs over all observed particles in the exit channel, E_{beam} is the total energy of the incoming proton, M_p is the mass of the proton, and p_{beam} is the momentum of the incoming proton.

The missing-mass distribution of four particles ($pp\pi^+\pi^-$), from 3-pion decay of the η meson is shown in Figure 5.11(a). The distribution shows a prominent peak around π^0 mass which is fitted with Gauss function plus a polynomial fit for the background. By putting a cut around the peak one can select the events with missing π^0 (we have used a quite large window between $50 MeV/c^2 - 250 MeV/c^2$ which corresponds to more than 3σ cut in order not to lose statistics).



(a) 3-pion decay



(b) The Dalitz decay

Figure 5.11: Missing-mass distributions of (a) $pp\pi^+\pi^-$ and (b) ppe^+e^- . Both (a) and (b) are fitted with Gaussian for a signal plus polynomial for background. 3.5σ cut around signal peak is used in order to select the reactions with missing π^0 and missing γ , correspondingly.

There is a big contribution from events with no missing particle ($pp \rightarrow pp\pi^+\pi^-$), which gives a peak around zero in the missing-mass distribution of four particles (see Figure 5.11(a)), in which we are not interested. This contribution is less pronounced in the simulation due to the much better track resolution.

Figure 5.11(b) shows the corresponding missing-mass distribution of four particles, $pp e^+ e^-$, for the Dalitz decay of the η meson with the prominent missing γ peak centered at zero. Like in the case of 3-pion final state the peak is fitted with the Gauss distribution plus a polynomial fit for the background. Only the events corresponding to the 3σ cut around the peak were selected.

5.4 η meson reconstruction

The main idea of doing the analysis steps described in the previous sections were to select reactions with missing π^0 corresponding to the decay of η meson into 3-pion final state ($\eta \rightarrow \pi^+\pi^-\pi^0$) and with missing γ corresponding to the Dalitz decay of the η meson ($\eta \rightarrow e^+e^-\gamma$).

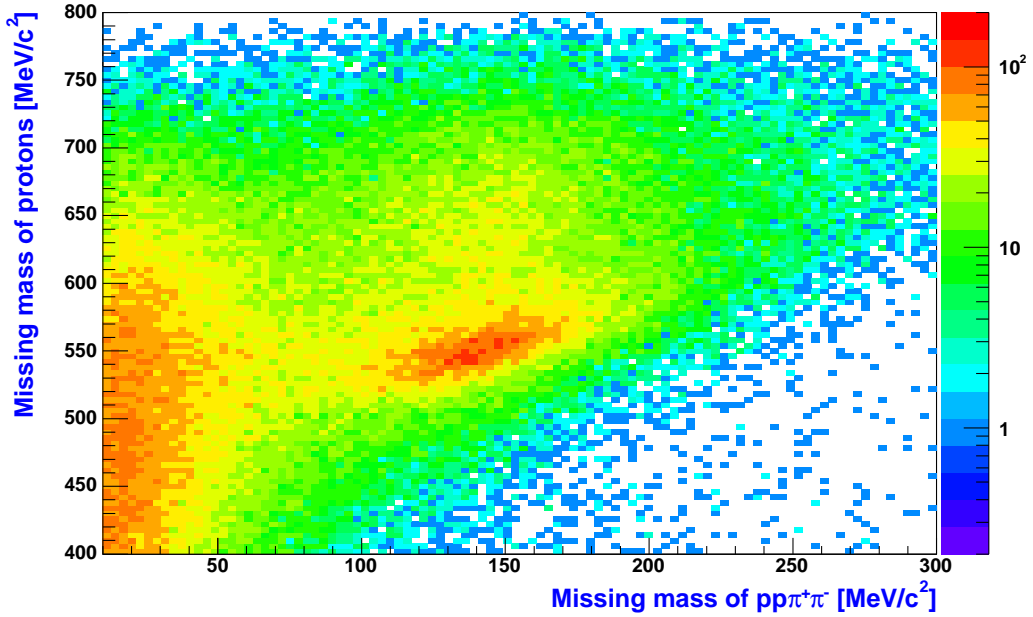


Figure 5.12: Missing mass distribution of $pp\pi^+\pi^-$ as a function of missing mass distribution of two protons for the experimental data, the η peak is seen in the region where the missing mass of four particles is located near the missing pion mass.

Figure 5.12 shows two-dimensional distribution of missing masses of four particles as a function of missing masses of two particles for the 3-pion final state for the experimental

data. One can easily see the η peak corresponding to the events where the missing mass of four particles is centered around the π^0 peak. Figure 5.13 shows similar distribution for the Dalitz decay where the evident peak of the η meson is seen for the missing mass of four particles centered at zero (γ peak).

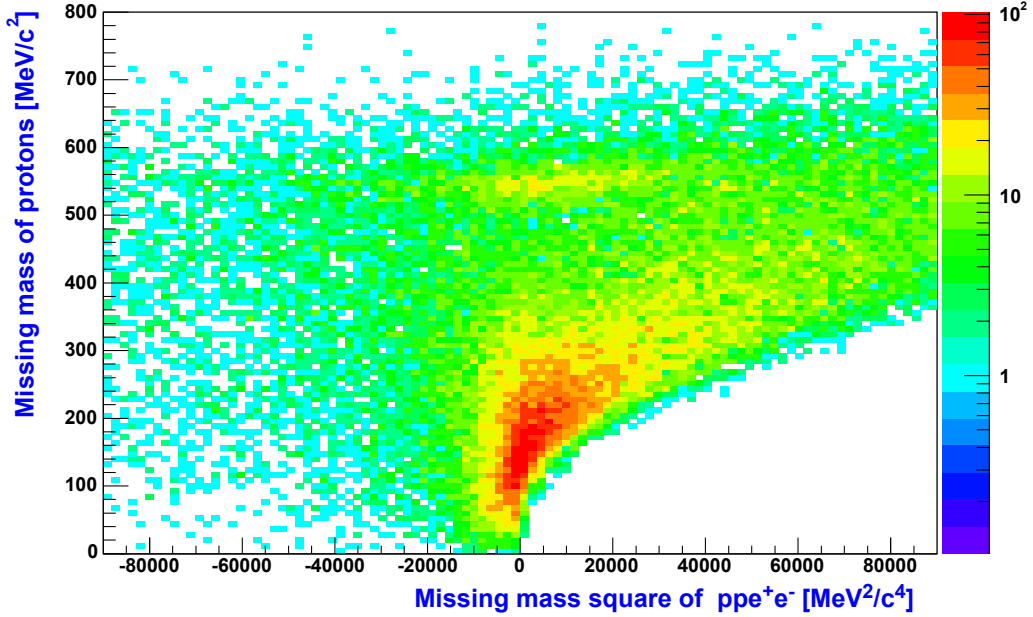


Figure 5.13: Square of missing mass distribution of ppe^+e^- as a function of missing mass distribution of two protons for the experimental data, the η peak is seen in the region where the missing mass of four particles is located at zero (γ peak).

We can reconstruct now η mesons from its 3-pion decay channel by plotting a missing-mass distributions of two protons by imposing a cut around π^0 peak in the missing mass distribution of four particles ($pp\pi^+\pi^-$). In the same way we can plot the missing mass of two protons by imposing a cut around zero on the missing mass distributions of ppe^+e^- . It is also possible to reconstruct missing momentum of π^0 (γ) and plot an invariant mass of $\pi^+\pi^-\pi^0$ ($e^+e^-\gamma$).

By putting a cut around the π^0 peak we get rid of the events where no missing particles appear ($pp \rightarrow pp\pi^+\pi^-$), giving a peak in the distribution of four particle missing masses around zero. There are background events as well where missing π^0 comes not only from the decay of η mesons (pions coming from Δ resonances and non resonant pion production).

Below we present the analysis results, both for simulation and experimental data. The applied selection cuts described in the previous sections are the same for both data samples.

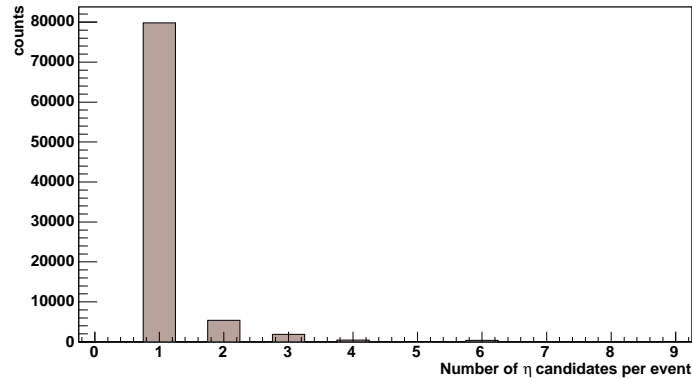


Figure 5.14: Multiplicity of η candidates per event left after all applied cuts. Only the events with one η candidate have been kept.

In order to prevent double counting of the η mesons per event, which can happen due to the fact that there was no cut applied on the number of tracks contributing to the event, the multiplicity cut was applied as well. Figure 5.14 shows the remaining eta candidates per event after performing all previously described cuts. Only the events which have one η meson candidate are selected for the next steps of the analysis.

Table 5.2 shows the number of events analyzed in experimental data and simulation after each condition on the multiplicity of the tracks per event or the events with a given multiplicity of corresponding particles.

Condition	Experiment	simulation
All	309.614.399	
MULT4 triggered	225.727.469	155.745.031
At least three positive and one negative	11.250.690	4.668.294
Three positive and one negative	6.999.624	3.169.480
At least two protons and one dilepton	241.690	89.208
Two protons and one dilepton	134.451	59.138
At least two protons and two pions	3.132.557	2.115.663
Two protons and two pions	2.303.219	1.631.337

Table 5.2: Number of events left under corresponding conditions.

5.4.1 Results for the simulation

The numbers of analyzed events are shown in Table 5.2. The η meson was produced through $N^*(1535)$ (isotropic angular distributions) while a phase space production for the case of the 3- pion final state decay and the Vector Dominance Model for the Dalitz decay have been used.

In this step of the analysis only the tracks with a "meta fake" marks have been removed from the sample, keeping all "track fakes" and using the not fitted tracks as well. The idea was to have a spectrum without imposing an opening angle cut on the pairs.⁷

Figure 5.15 shows the missing-mass distribution of two protons after selecting the events with missing π^0 by imposing a cut around the π^0 peak in the missing-mass distribution of four particles (See Figure 5.11(a)).

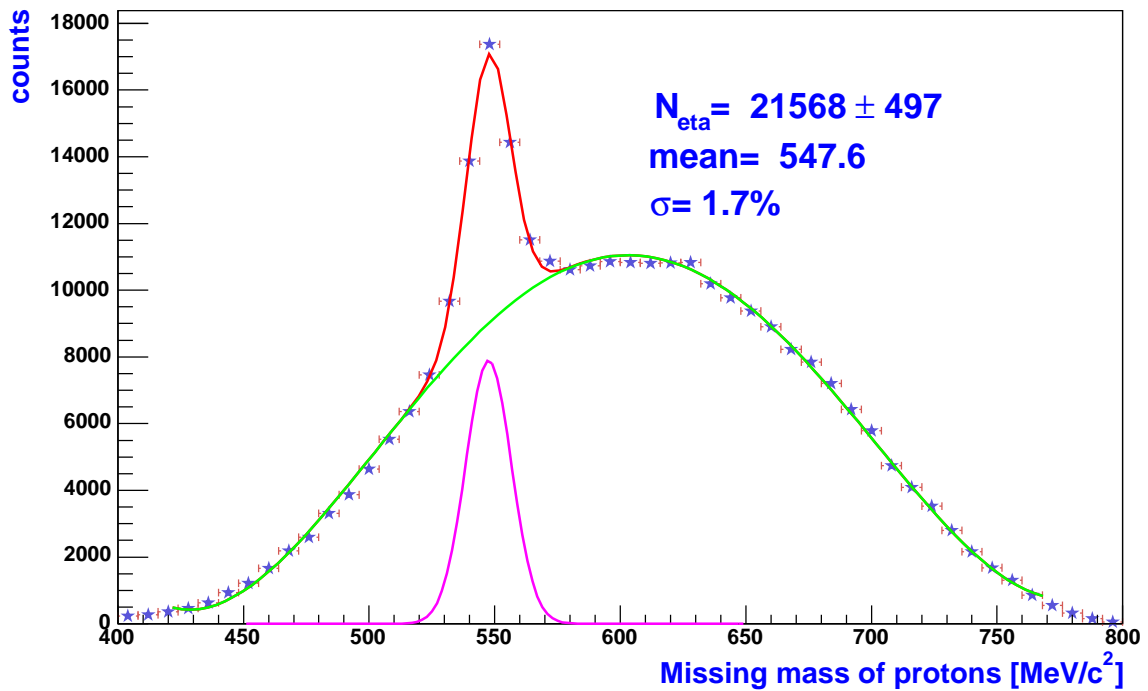


Figure 5.15: Missing-mass distribution of two protons after selecting the events with missing π^0 ; the distribution is fitted with a Gaussian for the signal plus a polynomial for background.

There is an evident peak at the pole mass of the η meson. The peak is fitted with a Gauss distribution plus a polynomial fit for the background. In order to extract the yield we have integrated the signal distribution in the Figure in the mass range between $500 \text{ MeV}/c^2$ and

⁷While removing the "track fakes" one indirectly applies an opening-angle cut between pairs as well.

$600 \text{ MeV}/c^2$. The number of reconstructed η mesons is equal to 21568 ± 497 . The errors on the yield were estimated by error propagation method using the parameters and errors of the fitting Gauss function. The signal is centered at $547 \text{ MeV}/c^2$ with the resolution 1.7%.

Figure 5.16 shows a missing-mass distribution of two protons by imposing a cut around the gamma peak in the distribution of the four-particle missing mass (See Figure 5.11(b)). The evident peak around the η meson mass corresponds to the reconstructed η mesons. As in the previous case the η signal is fitted with a Gauss distribution plus a polynomial fit for the background which is coming from multi-pion production. Besides of the Dalitz decay of the η meson, its 2γ decay is also contributing to the η peak. One of the photons from $\eta \rightarrow \gamma\gamma$ can convert into e^+e^- pairs by hitting some detector parts, thus giving a nice candidate of $e^+e^-\gamma$ which will also contribute to the η peak in the missing-mass distribution of two protons (See section 5.4.4).

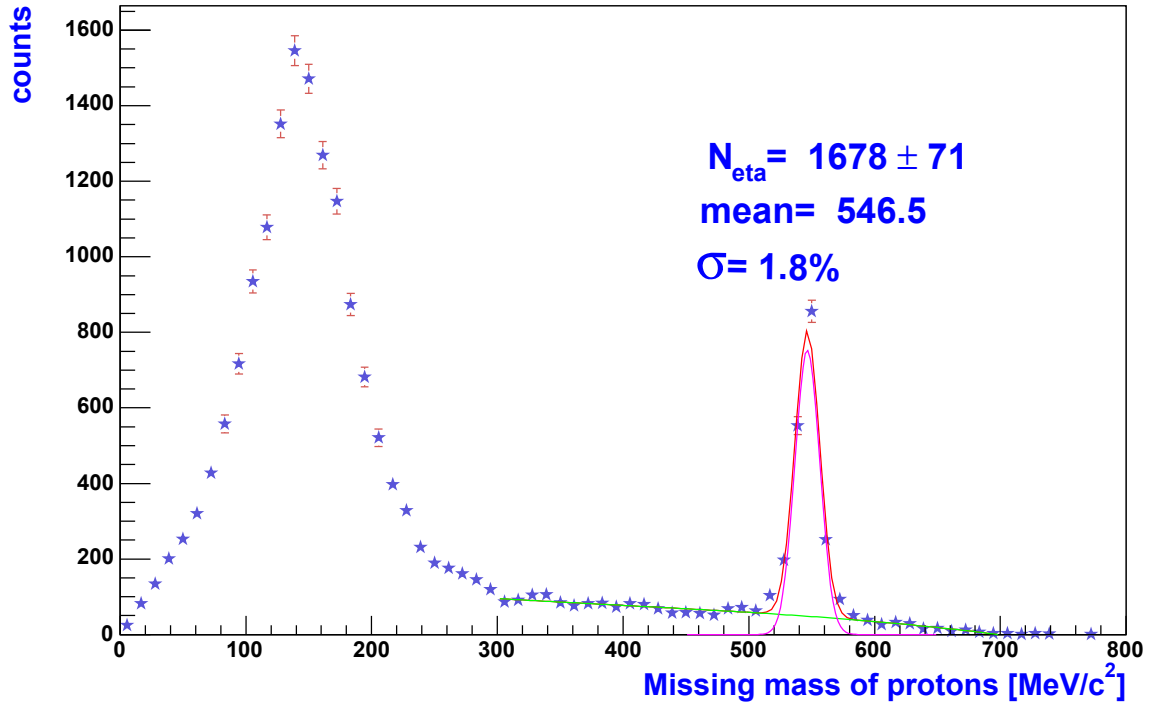


Figure 5.16: Missing-mass distribution of two protons after selecting events with missing γ ; the distribution is fitted with a Gaussian for the signal plus a polynomial for background.

One can also see the peak around the π^0 mass corresponding to the reconstructed pions. The number of reconstructed η mesons obtained in similar way as for 3-pion final state is equal to 1678 ± 71 . From these numbers one can calculate the ratio of reconstructed η mesons between the two decay channels.

5.4.2 Results for experimental data

The number of analyzed events in the experimental data, together with the events left after applying different conditions, are shown in Table 5.2.

Figure 5.17 shows the missing-mass distribution of two protons for the 3-pion final state (The procedure of plotting this picture is in detail explained in the previous section). The η peak has been fitted like for the simulation with a Gauss distribution plus a polynomial fit for the background.

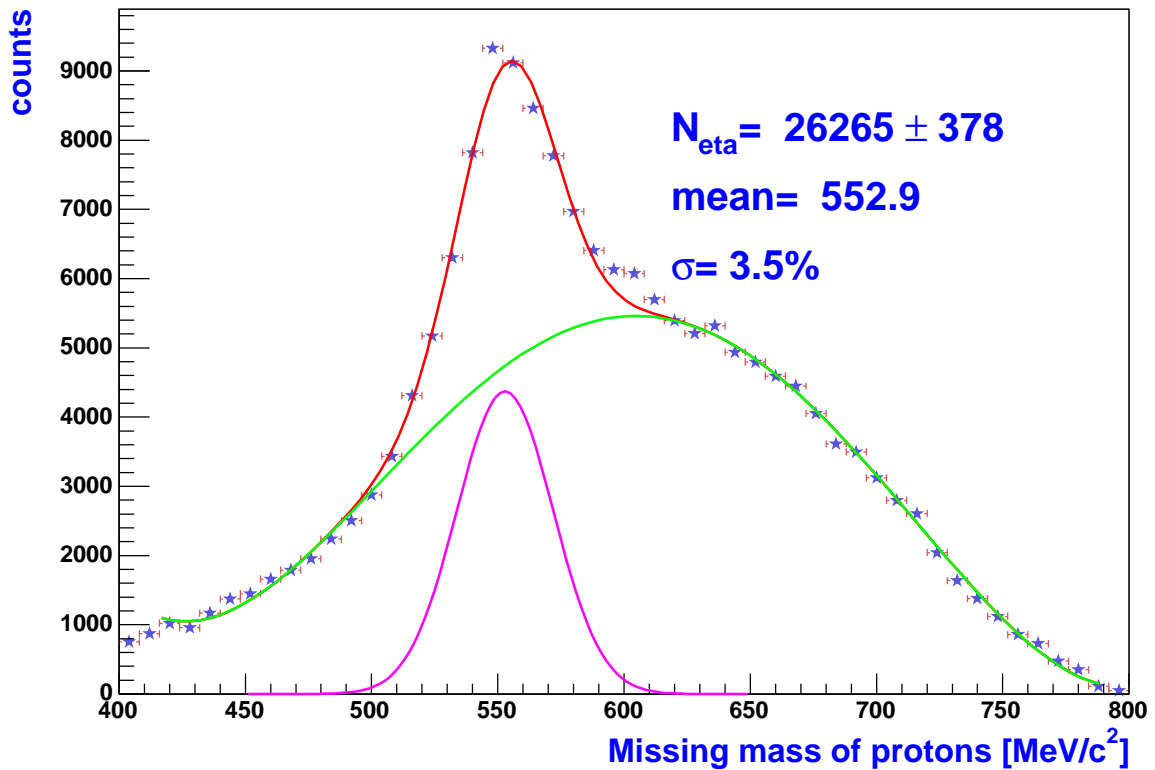


Figure 5.17: Missing-mass distribution of two protons after selecting events with missing π^0 ; the distribution is fitted with a Gaussian for the signal plus a polynomial for background. The yield was calculated by counting the histogram entries above the background due to small structure in the signal.

There is a small structure in the peak as it is shown in Figure 5.17 which is related to the fact that the spectrometer was not fully built during this run. Therefore in the sectors with 3 MDC chambers the resolution of the track reconstruction are worse. As a consequence one Gaussian fit does not describe the peak. Because of this fact, the number of the reconstructed η mesons were calculated by not integrating the signal peak, like in

case of simulation, but just counting the histogram entries above the background, thus taking into account the structure as well. The number of reconstructed η mesons is equal to 26265 ± 378 . The mass of the reconstructed η mesons are located at $553 \text{ MeV}/c^2$ with the width of $18 \text{ MeV}/c^2$ corresponding to 3.5% resolution in mass. In the lower mass region one can also see the contribution from $pp \rightarrow pp\pi^+\pi^-$.

The missing-mass distribution of two protons from η Dalitz decay is shown in Figure 5.18. In this case the reconstructed pion mass is shifted even more than in the simulation and furthermore the background coming from multi-pion production is shifted as well, therefore the calculated number of η mesons is overestimated (Because of the wrong approximation of the background).

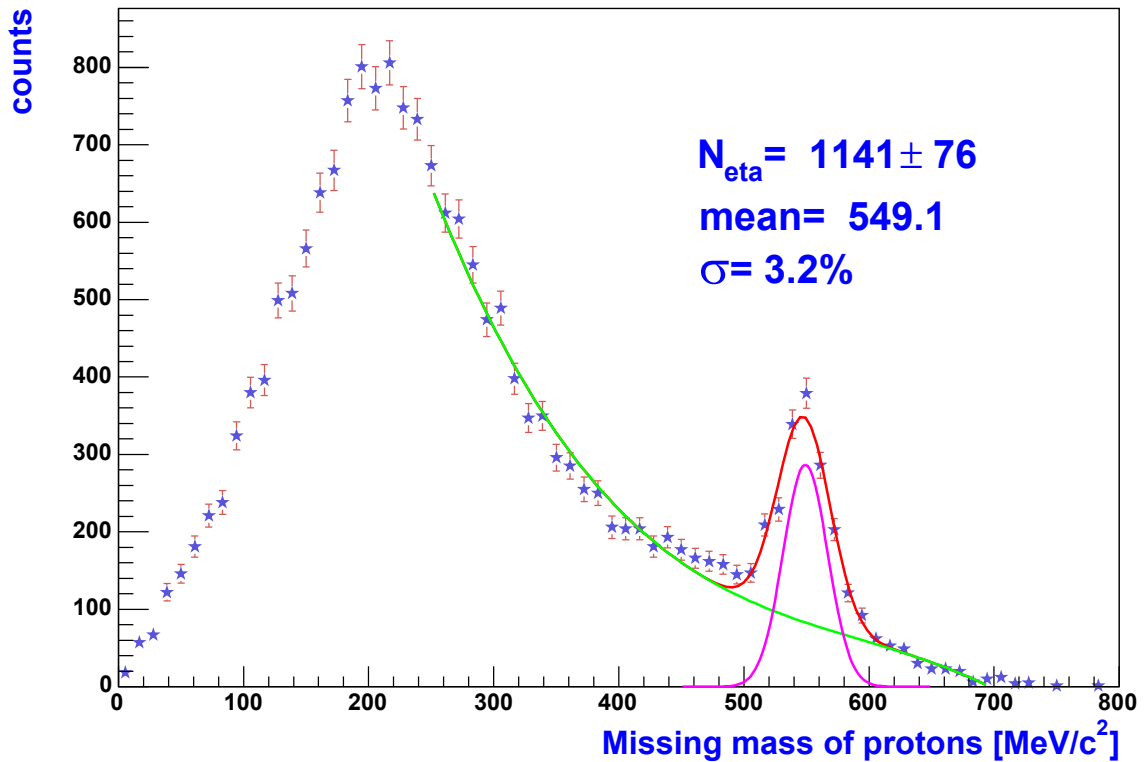


Figure 5.18: Missing-mass distribution of two protons after selecting events with missing γ ; the distribution is fitted with a Gaussian for the signal plus a polynomial for background.

5.4.3 Kinematic fit

Kinematic fit is a mathematical procedure that uses physical constraints, such as energy-momentum conservation, to improve measurements [75]. In general, one uses constraints

to impose "external knowledge" of a physical process to govern the behavior of the fit, thereby forcing the fit to conform to physical principles which are not known by the internal variables of the fit. When constraints are applied, the effective number of unknowns (degrees of freedom) in the fit is reduced by the number of constraints. The constraints are imposed using the well known Lagrange multiplier technique. It is important to choose "proper" track parametrization for kinematic fit. The word "proper" means, the parameters should have physical meaning and be kinematically complete, the errors of parameters should be close to gaussian. The following track parametrization was used for the algorithm:

$$\alpha_i = \begin{pmatrix} \frac{1}{p_i} \\ \theta_i \\ \phi_i \end{pmatrix} \quad (5.11)$$

where the index i runs over all 4 tracks.

From a mathematical point of view the procedure means finding a minimum of the function (For details see Appendix C):

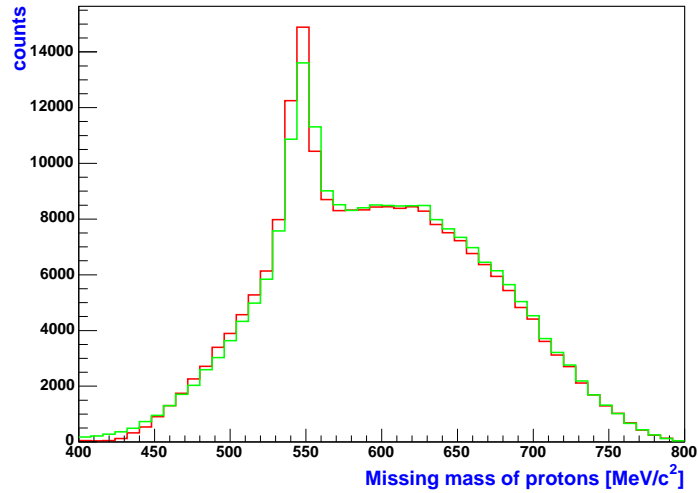
$$F = (\alpha - \tilde{\alpha})^T W^{-1} (\alpha - \tilde{\alpha}) + 2\lambda^T H(\tilde{\alpha}) \quad (5.12)$$

where λ is a matrix of Lagrange multipliers, H is a matrix of constrains, α is a matrix of track parameters, and $\tilde{\alpha}$ is a matrix of modified track parameters. The factor 2 before the Lagrange multipliers is introduced in order to simplify the calculations. The quality parameter for the fitting is the first part of 5.12, which approaches the well known χ^2 distribution with the degrees of freedom being equal to the number of constraints used.

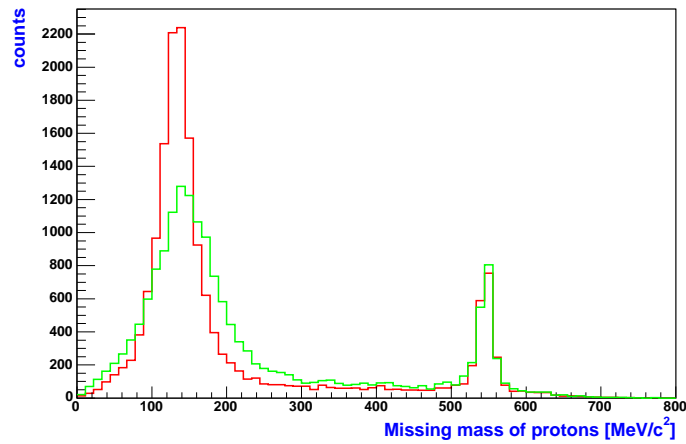
Only one constraint for each decay channels has been used:

- missing mass of $pp\pi^+\pi^- = m_{\pi^0}$ for the 3- pion final state
- missing mass of $ppe^+e^- = m_{\gamma} = 0$ for the Dalitz decay

The comparison of missing-mass distributions of two protons before and after the kinematic fit for the simulation in case of 3-pion final state and the Dalitz decay are shown in Figures 5.19(a) and 5.19(b) correspondingly. Similar distributions are shown for experimental data in Figures 5.20(a) and 5.20(b).



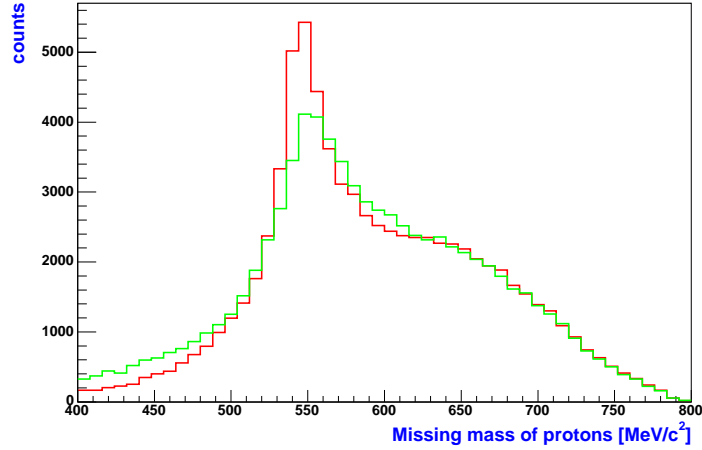
(a) 3-pion decay



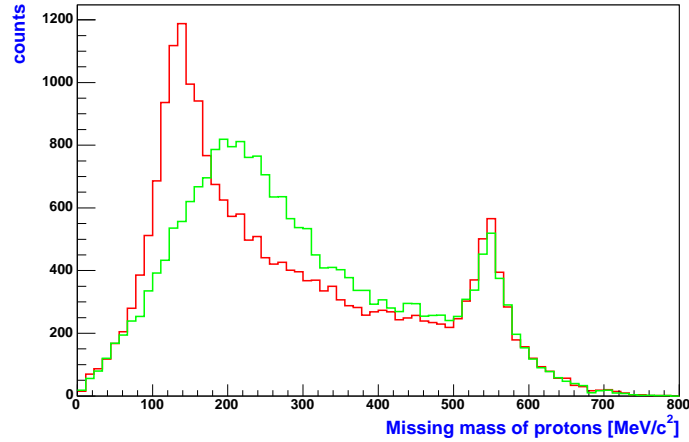
(b) Dalitz decay

Figure 5.19: Comparison of missing-mass distributions of two protons for simulation before (green) and after (red) the kinematic fit algorithm. (a) after selecting events with missing π^0 in missing mass distributions of $pp\pi^+\pi^-$ and (b) after selecting events with missing γ in missing-mass distributions of ppe^+e^- .

While there is no big improvement for simulation in the η region, connected to a quite good tracking resolution in this case, there is a significant improvement of the η mass resolution (almost factor of 1.5 for 3-pion decay and factor of 1.2 for the Dalitz decay) and signal to background ratio for experimental data.



(a) 3-pion decay



(b) Dalitz decay

Figure 5.20: Comparison of missing-mass distributions of two protons for experimental data before (green) and after (red) the kinematic fit algorithm. (a) after selecting events with missing π^0 in missing mass distributions of $pp\pi^+\pi^-$ and (b) after selecting events with missing γ in missing-mass distributions of ppe^+e^- .

Looking at the lower mass part of missing-mass distributions for 3-pion decay before and after the kinematic fit one can see the decrease of the contribution from the $pp\pi^+\pi^-$ channel (after applying a 5% significance level cut on χ^2 distribution of the kinematic fit) as well, moreover this decrease is more pronounced for experimental data. Furthermore

for the Dalitz decay, the pion mass both in simulation and experimental data is shifted into the correct place, and the background corresponding to the multi-pion production is more realistic.

Figures 5.21(a) and 5.21(b) show the kinematic fit χ^2 distributions compared with the theoretical one for the 3-pion final state and the Dalitz decay, correspondingly. One can see the nice agreement between the two distributions indicating the fact that the parameters were changed inside the errors.

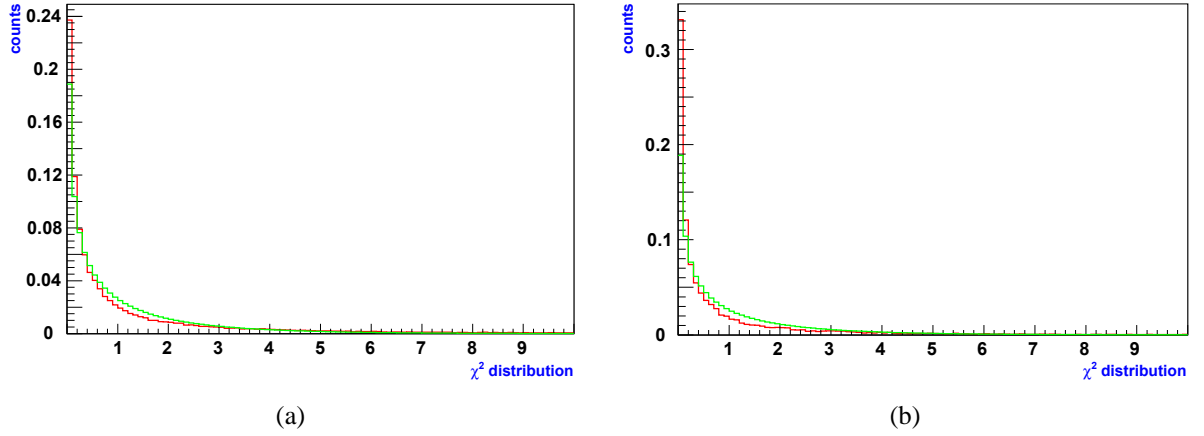


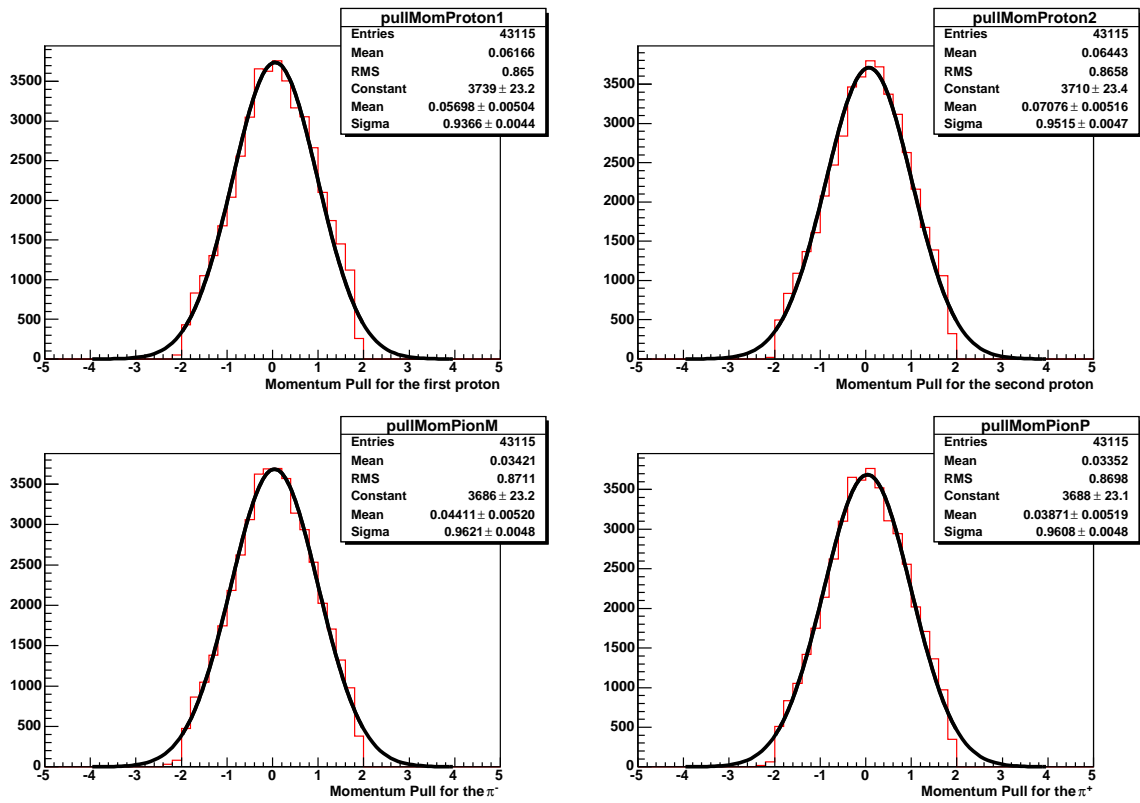
Figure 5.21: χ^2 distribution of the kinematic fit for 3-pion final state (a) and the Dalitz decay (b) for experimental data. The green distributions correspond to the calculated χ^2 function, while red distributions are obtained from the data.

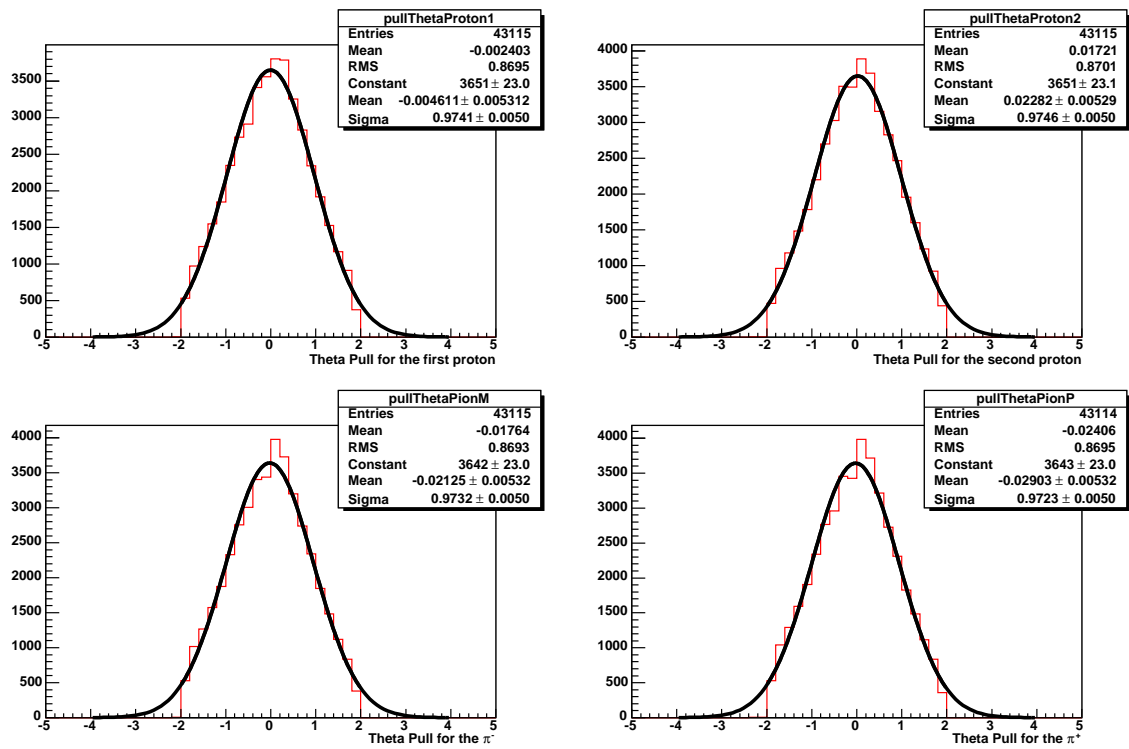
One should keep in mind that it is possible to parameterize the errors incorrectly, but still have a consistent χ^2 distribution or a flat Confidence Level distributions. The pull distributions provide a way to guard against this.

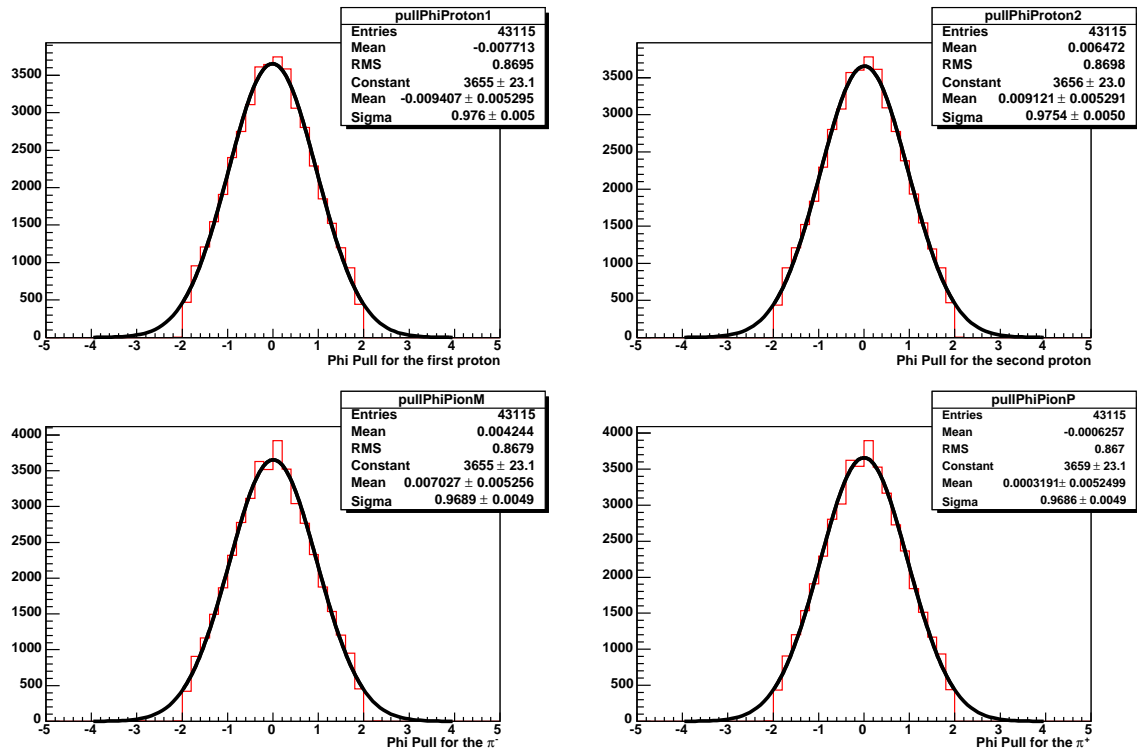
The pull of the i^{th} fit quantity is defined as,

$$pull_i = \frac{\alpha_i - \tilde{\alpha}_i}{\sqrt{\sigma^2(\alpha_i) - \sigma^2(\tilde{\alpha}_i)}} \quad (5.13)$$

The pulls should be normally distributed about zero with a $\sigma = 1$. A systematic error in one of the measured quantities, α_i , can be seen as an overall shift in the distribution of the corresponding $pull_i$ away from zero. Similarly, if the error of α_i has been (over-estimated) underestimated, then the corresponding pull distribution will be too (narrow) broad. Figures 5.22, 5.23 and 5.24 show the pull distributions of all parameters used in the kinematic fit for the 3-pion final state fitted by the Gauss distributions. The width of the pull distributions are equal to 1 only after re-scaling (increasing by a factor of 1.5) of the angular errors provided by a track fitter (Which are propagated from the errors of the drift times generated by the GARFIELD simulation). Similar distributions are obtained for the Dalitz decay as well.

Figure 5.22: Pull distributions for inverse momenta of p, p, π^- and π^+ .

Figure 5.23: Pull distributions for polar angles of p, p, π^- and π^+ .

Figure 5.24: Pull distributions for azimuthal angles of p, p, π^- and π^+ .

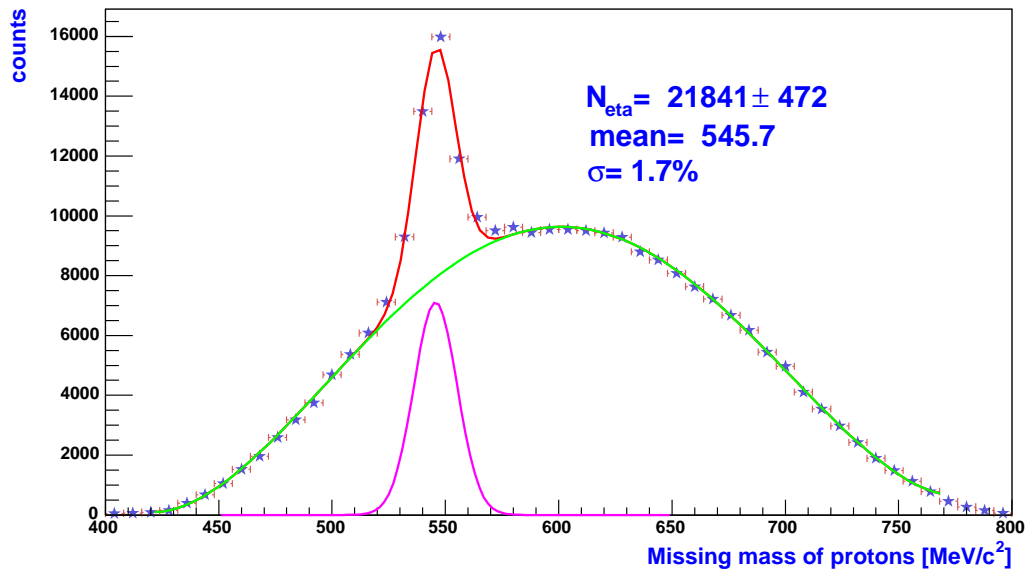


Figure 5.25: Missing mass distributions of two protons after selecting events with missing π^0 for simulation after the kinematic fit.

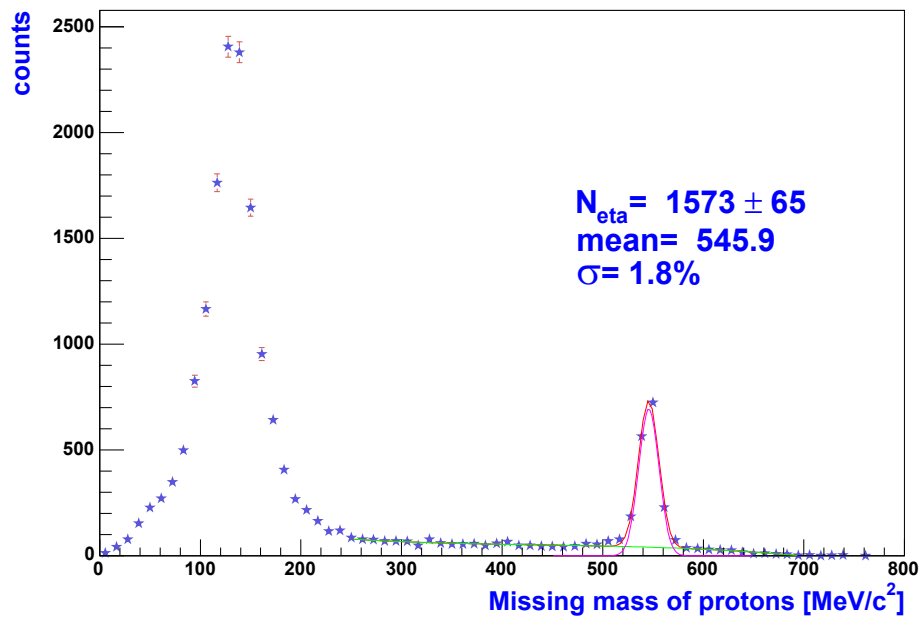


Figure 5.26: Missing mass distributions of two protons after selecting events with missing γ for simulation after the kinematic fit.

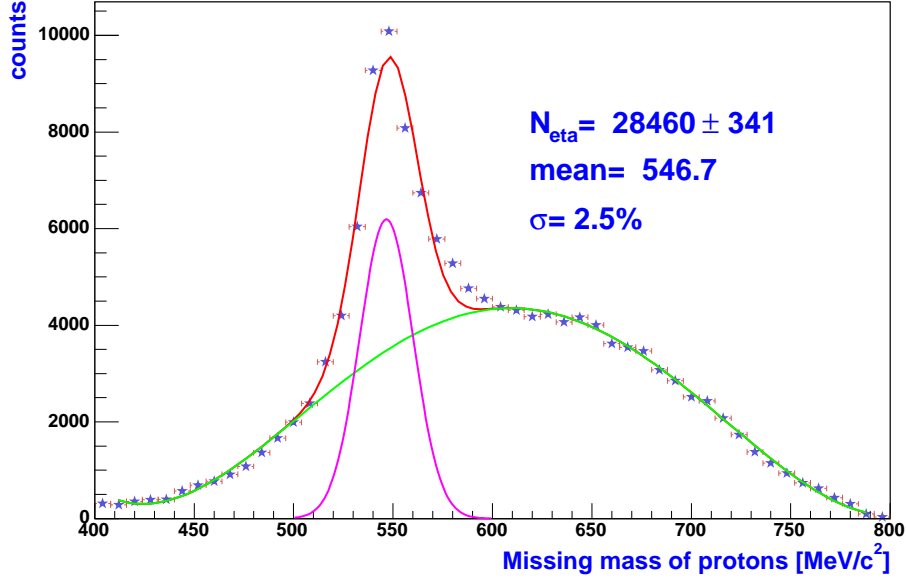


Figure 5.27: Missing-mass distributions of two protons after selecting events with missing π^0 for experimental data after the kinematic fit.

The missing-mass distributions of two protons for the 3-pion final state after application of the kinematic fit algorithm is shown in Figure 5.25 for the simulation. The η peak was fitted with a Gauss function plus a polynomial fit for the background. The reconstructed number of η mesons is equal to 21841 ± 472 . The peak is centered around $546 \text{ MeV}/c^2$ with the resolution of 1.7%. The missing mass distribution of two protons for the Dalitz decay of the η mesons is shown in Figure 5.26. As it is seen from the Figure the pion mass is shifted to the correct position with much narrow width. The number of reconstructed η mesons is equal to 1573 ± 65 . The η peak is centered around $546 \text{ MeV}/c^2$ with the resolution of 1.8 %.

Similar distributions for the experimental data are shown in Figures 5.27 and 5.28 for the 3-pion and the Dalitz decays the η meson, correspondingly. The number of reconstructed η mesons from the 3-pion final state, which was obtained by counting a histogram counts above the background in Figure 5.27 due to the small structure in the η yield, is equal to 28460 ± 341 . The η peak is centered around $547 \text{ MeV}/c^2$ with the resolution of 2.5%. We get a factor of 1.5 improvement in the mass resolution of the reconstructed η mesons after application of the kinematic fit algorithm. The reason for increasing of the reconstructed η meson yield from its 3-pion decay is partly connected to the background approximation accuracy. The systematic shift on the level of 5% can easily be obtained by changing the range and shape of the background function. The reconstructed number of η mesons after application of the kinematic fit from its Dalitz decay is equal to 1034 ± 64 . The η peak is centered around $548 \text{ MeV}/c^2$ with the resolution of 2.8 %. In this case we

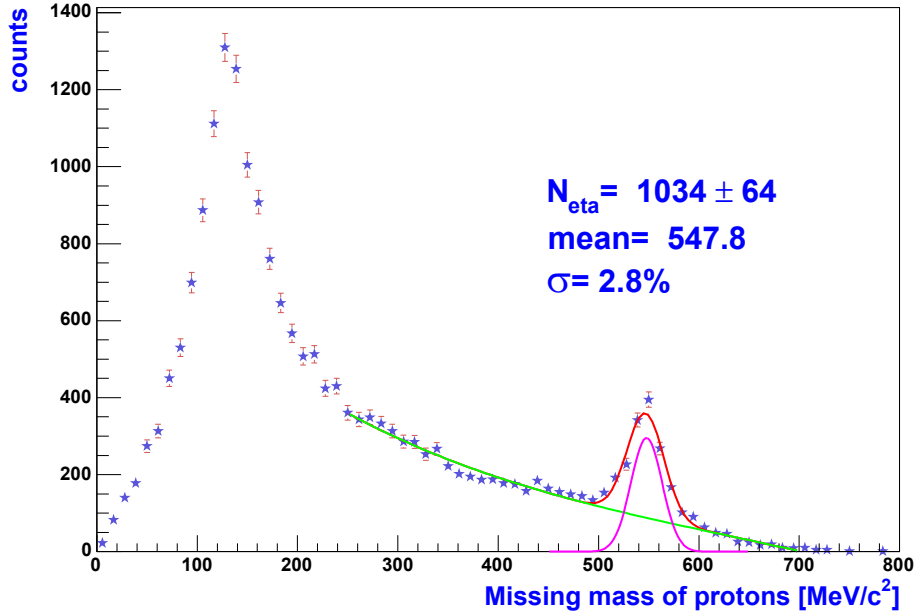


Figure 5.28: Missing-mass distributions of two protons after selecting events with missing γ for experimental data after the kinematic fit.

get an improvement by a factor of 1.2 in the mass resolution of the reconstructed η mesons compared with the results obtained without application of the kinematic fit algorithm. Furthermore as it is seen from Figure 5.28 the pion mass is shifted into its correct position with much improved width. The background corresponding to multi-pion production is also more realistic after application of the kinematic fit. The decrease in the number of η mesons from its Dalitz decay after application of the kinematic fit has several reasons. One of them is connected to the fact that before the kinematic fit the background is shifted as it is seen from Figure 5.18. As a consequence the background approximation is also wrong. Another reason is as in case of 3-pion final state the systematic shift in the background approximation.

5.4.4 Contribution from $\eta \rightarrow \gamma\gamma$

Besides the $\eta \rightarrow e^+ e^- \gamma$ decay there is a contribution from $\eta \rightarrow \gamma\gamma$ as well to the number of reconstructed η mesons. One of the photons may convert into $e^+ e^-$ pairs by hitting some detector part⁸.

⁸Pair production from a γ is not possible in vacuum due to the energy conservation law. Indeed if one assumes this decay to happen in e.g. the LAB system then there is an infinite number of frames moving with respect to LAB frame where this process can happen as well. In each of these systems the photon will be

Figure 5.29(a) shows the missing mass of two protons for all pairs (black) for the case where one of the leptons is coming from conversion (green) and whose both particles are coming either from pions or eta mesons (red) (Dalitz decay).

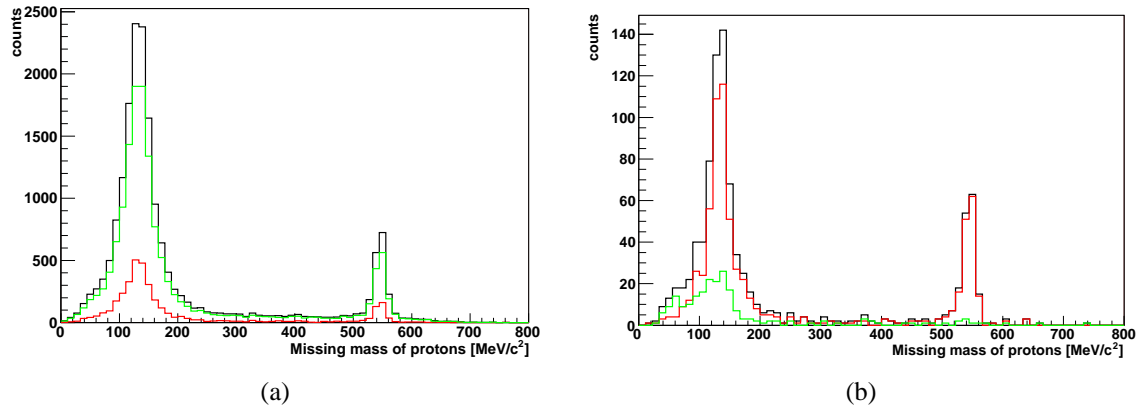


Figure 5.29: Missing-mass distribution of two protons for the Dalitz decay for all pairs (black), when at least one of the dileptons is coming from γ conversion (green) and when both leptons are parent particles (red), before applying the cuts (a) and after applying the cuts (b).

One can easily see that the main contribution is due to the conversion pairs. The characteristic feature of the conversion pairs is that the opening angle between leptons is very small. As a consequence these tracks will be close to each other in the Drift chambers thus will not be fitted by the track fitter. This will increase the number of fake tracks created. Therefore, in order to get rid of these events, several cuts described below have been applied:

- a) Removing fake track contributions
- b) Opening angle cut
- c) Using segment's χ^2 cut

After applying these cuts the distribution is plotted again in Figure 5.29(b); one has much smaller contribution from the conversion decay.

seen with a shift of its frequency ν due to the Doppler effect. One can choose a reference system where it is less than E_0/h , where E_0 is equal to $2m_e c^2$; therefore the energy of the photon $h\nu$ will not be enough for pair creation in this frame. Consequently this process can not happen in the LAB frame. On the other hand, in the presence of a nucleus or an electron this process can happen because the energy and momentum of the photon will be shared between 3 particles in this case.

5.5 Estimation of the dilepton identification efficiency

At this point we can estimate the dilepton identification efficiency of the HADES spectrometer by calculating a ratio (R) (See Section 5.0.1):

$$R = \frac{R_{exp}}{R_{sim}} \quad (5.14)$$

where R_{exp} and R_{sim} are the ratio of reconstructed η mesons from its 3-pion and Dalitz decays correspondingly for experimental data and simulation.

For estimation of R_{exp} two things should be taken into account. For the 3-pion final state only downscaled events have been analyzed. Therefore the downscaling factor should be taken into account for normalization (See section 2.5). The downscaling factor was taken into account on event-by-event basis⁹, therefore each bin of the missing mass distribution in case of 3-pion final state was filled downscaling factor times. For the Dalitz decay only the events with positive second level trigger decision have been taken. Therefore the efficiency of the second level trigger should be taken into account as well. This efficiency can be calculated using only downscaled events by evaluating the ratio of reconstructed η mesons with positive decision of the second level trigger to the reconstructed η mesons from the whole sample which amounts to almost 82%. Thus the ratio should be calculated with:

$$R_{exp} = \frac{N_{had}}{N_{Dalitz}/\varepsilon_{LVL2}} \quad (5.15)$$

where $\varepsilon_{LVL2} = 0.82$ is the efficiency of the second level trigger.

The obtained results are discussed in Chapter 6.

In simulation no downscaling were applied. The LVL2 trigger decision was not used as well in simulation.

5.6 η meson production

In order to investigate the production mechanism of the η mesons their angular distributions were reconstructed in the center- of-mass system of two protons. For this investigation only the 3- pion final state has been used because of the high statistics available in this case. In order to subtract a background the missing-mass distribution was plotted for 10 bins of the reconstructed angle thus allowing us to see how background changes as a function of the angle. The signal in each bin was fitted from a shape of the η mesons taken from simulation while for the background the polynomial fit has been used. After subtracting the

⁹Because of the fact that the downscaling factor was changing from file to file, this correction has been made on the event level.

background the one-dimensional picture for angular distributions is compared to the corresponding distribution obtained from simulation of pure η mesons by nucleon excitation to the $N^*(1535)$ state, as illustrated in Figure 5.30. As the orbital momentum of this excited state is equal to 0, the angular distributions should be flat (s wave decay). The nice agreement of the experimental distribution with simulated one (blue line in the Figure) confirms the s wave production of the η meson. This illustrates that the assumption of production of the η mesons through $N^*(1535)$ in simulation are in good agreement with the experimental data.

One should note that the discrepancy of the obtained distribution, as it is seen in Figure 5.30, from an isotropic one is due to the acceptance of the HADES spectrometer. After acceptance correction for the phase space we should have again the s wave distribution as it is assumed in event generation (before going to the HADES acceptance).

Obtained angular distributions of the η mesons is compared with the simulation where the anisotropy observed by the DISTO experiment was included (green line in Figure 5.30). On can see from the Figure that both simulations (with isotropic (blue) and anisotropic (green) angular distributions) describes the data quite well within error bars.

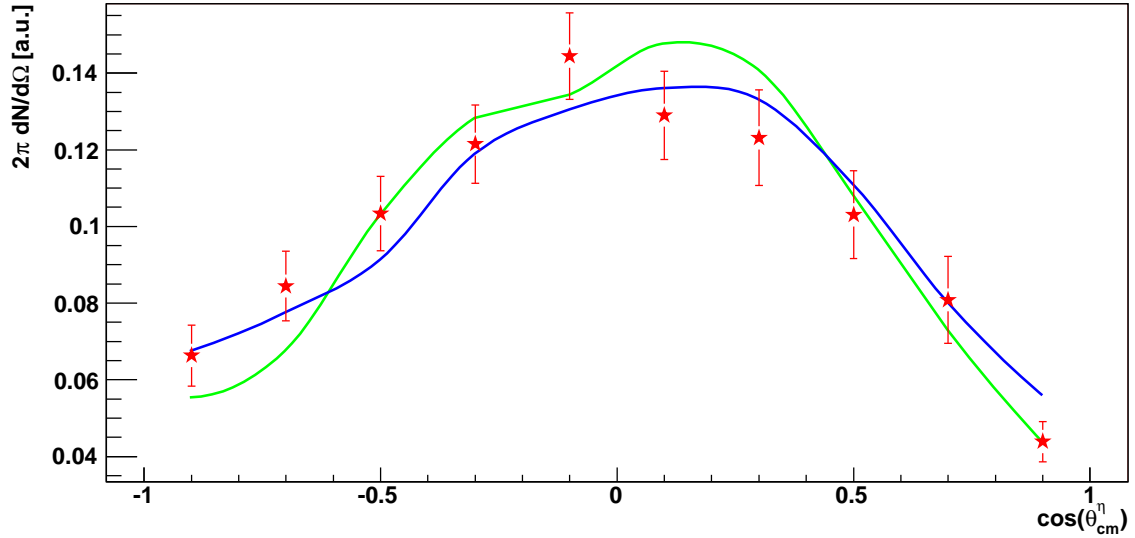


Figure 5.30: Angular distributions of the η mesons after background subtraction in the center-of-mass system of protons from experimental data (red points) compared with those obtained from simulation (blue line) generated isotropically through the N_{1535}^* resonance. The green line corresponds to the simulation where the anisotropy observed by the DISTO experiment has been included.

5.7 η meson decay

The Dalitz decay of the type $\eta \rightarrow e^+e^-\gamma$ can be reduced to a decay into a real photon plus a virtual photon and a subsequent decay of the virtual photon to e^+e^- pair [2, 6]. If there is a structure around the η meson, which is characterized by a transition form factor, this will affect the probability of emitting the virtual photon with a given momentum, consequently the invariant-mass distribution of e^+e^- pairs will be affected as well because the square of momentum of the photon is just equal to the invariant mass of the lepton pairs it decays to. The distribution will look different for a pure QED calculations where no structure around the meson is taken into account. In the Vector Dominance Model this effect is taken into account by the coupling of the virtual photon to a virtual vector mesons like ρ, ω or ϕ . Thus the virtual photon can interact with the hadron also after a transition to the virtual vector meson state. In order to investigate the validity of the Vector Dominance Model in describing this decay the experimentally reconstructed e^+e^- invariant mass distribution after background subtraction is compared to the VDM model calculation.

As the background in the pp missing-mass spectrum can nicely be described by a straight line one can construct 3 trapezoids as shown in Figure 5.31. The number of events inside the middle trapezoid will be equal to the arithmetic mean of the left and right ones (because the middle line of any trapezoid is defined as the arithmetic mean of its bases, the sum of the entries in each bin of the middle trapezoid will be equal to the averaged sum of the corresponding bins from the side trapezoids); therefore, in order to subtract a background, first three distributions of invariant masses are created corresponding to the region of missing masses covered by the corresponding trapezoids. The averaged mean of the invariant-mass distributions corresponding to the left and right side bands were subtracted from the central one. The distribution obtained in this way is plotted in Figure 5.32. The red solid line in the Figure corresponds to the calculations done with the Vector Dominance Model, while the blue line corresponds to pure QED calculations. Except the last bin the model describes the data quite well within error bars.

There can be several reasons responsible for the discrepancy of the last bin from the VDM calculations in the invariant-mass distribution of e^+e^- pairs, as shown in Figure 5.32:

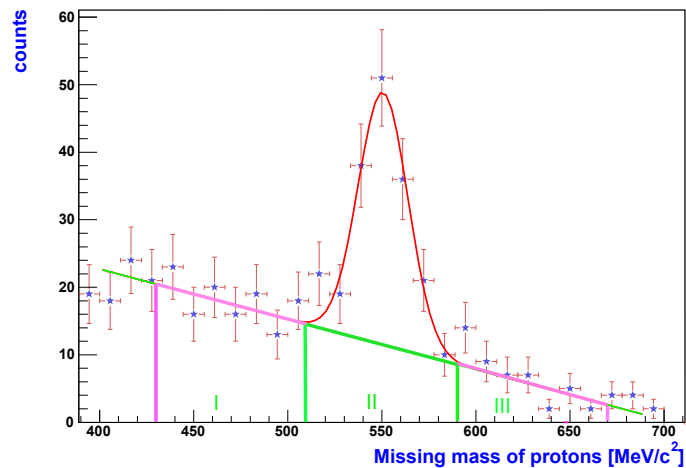


Figure 5.31: Illustration of the background subtraction. The background is estimated as the averaged mean from side bands.

this may come from physics, the method for background subtraction can be not applicable for this bin or this might be attributed by other processes, like contribution from multi-pion production, or contribution from fake combinations.

In order to test the background subtraction method, another method was tried, like in case of background subtraction for angular distributions. The missing mass distributions of two protons were plotted for several slices of e^+e^- invariant mass distribution. In this way it is possible to investigate the background behavior as a function of the invariant mass of e^+e^- pairs. The results of this method shows similar behavior for the last bin in the invariant mass distribution of e^+e^- pairs. It is not clear how the background behaves in this bin. The background can be estimated using simulated data with realistic physics processes.

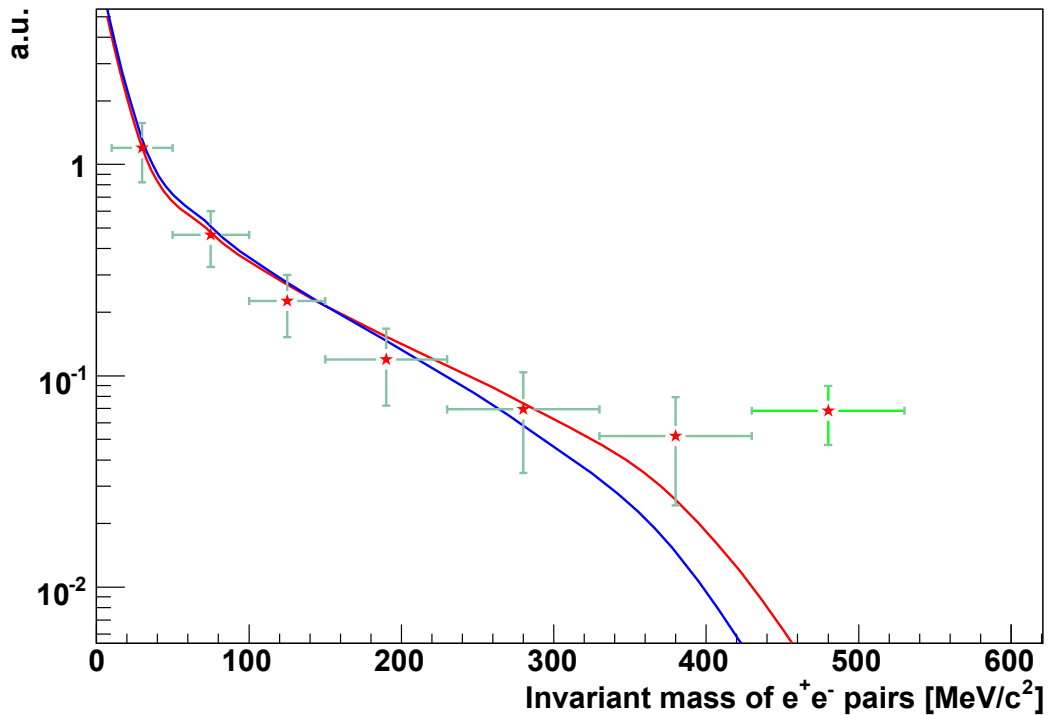


Figure 5.32: Invariant mass distributions of e^+e^- pairs, from experimental data, after acceptance correction compared with Vector Dominance Model calculations (red) and QED calculations (blue).

Since in our simulation the VDM model was used for the η meson Dalitz decay, it was obvious to reconstruct the invariant mass distributions of the e^+e^- pairs from simulation and compare with the VDM model calculations. The results of this analysis is shown in Figure 5.33. As it is seen from the Figure the problem exists also in simulation, but less pronounced. Therefore this might be connected to the estimation of the background in this

bin, and not to the VDM model itself. This might also be connected to the created fake combinations. We expect that fake track contributions from simulation is smaller, due to the better reconstruction resolutions in this case.

Another important thing can be seen by comparing the invariant mass distributions from simulation and experimental data. In case of simulation one can see entries in the e^+e^- distribution at the pole mass of the η meson, while this is not the case for the experimental data, the direct decay of the η meson to e^+e^- pairs. There exists a lower limit on branching ratio of this decay channel in [76], which was used in our simulation. On the other hand, as it is shown in the Table 5.2, the analyzed statistics is more for experimental data compared to the simulation. Therefore we can conclude that the lower limit presented in [76] for this decay channel is larger than it should be.

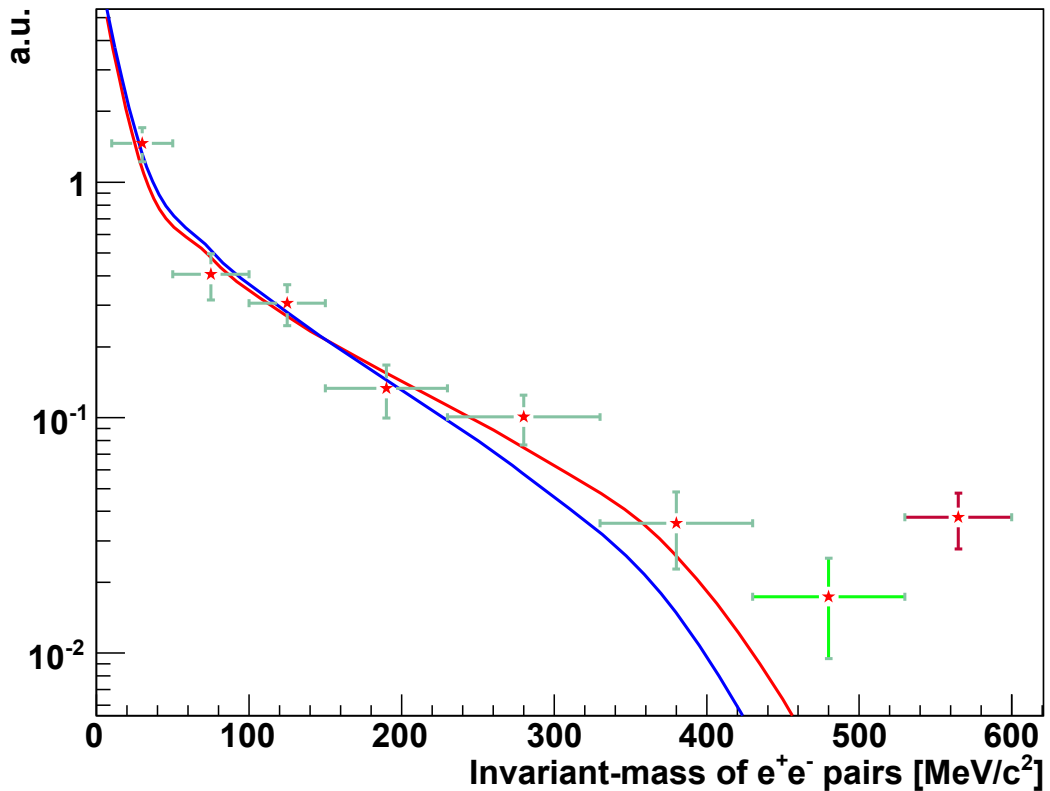


Figure 5.33: Invariant mass distributions of e^+e^- pairs, from simulation, after acceptance correction compared with Vector Dominance Model calculations (red) and QED calculations (blue).

Chapter 6

Discussion and Outlook

In this chapter the main obtained results are presented:

- Section 6.0.1: Estimation of the dilepton identification efficiency of the HADES spectrometer
- Section 6.0.2: Investigation of the η meson production
- Section 6.0.3: Test of the VDM model in describing the η meson decay

The first proton-proton production run at 2.2 GeV kinetic energy of incident proton beam was conducted successfully in January 2004. It was the first time when the spectrometer was fully set up in four sectors out of the six. The remaining two sectors had one missing MDC chamber; therefore it was necessary to develop a new algorithm for momentum reconstruction which uses information from all four (or three) MDC chambers in the setup in order to achieve high momentum resolution. Basically, one needs either the input momentum or some reference points inside the magnetic field on the trajectory of the particle. As this information is not available, the reconstruction procedure was based on assuming a cubic spline model for the track with the objective of estimating points from the model and derivatives at those points inside the magnetic field. In the next step the field equations were solved by imposing a particle to go through the points taken from the track model by fitting the momentum which satisfies this condition. As the method uses a model which sometimes differs from the real trajectory of the particle, especially in the low-momentum region and the regions close to the magnet coils, a correction table was created in order to take into account this effect. The obtained resolution of the method is in the order of 1 – 2%. The spline method provides the sign of the charge of the particle as well. The momentum reconstructed with the spline method, together with its sign, is then taken as an initial value for tracing the particle through the spectrometer by solving the equation of motion for the particle. The obtained second-order differential equations are solved using Runge Kutta methods where all initial conditions are fixed from track fitting

and an initial momentum is taken from the spline method. As there is a residual magnetic field inside the MDC chambers, the real trajectory of the particle differs from the straight line assumption made on track segments before and after the magnetic field in the track fitting; therefore in the method of Runge Kutta, not only the momentum, but also the angles are varied during the minimization procedure. However there are still some problems, especially for momenta below 70 MeV/c, due to the straight segment assumption.

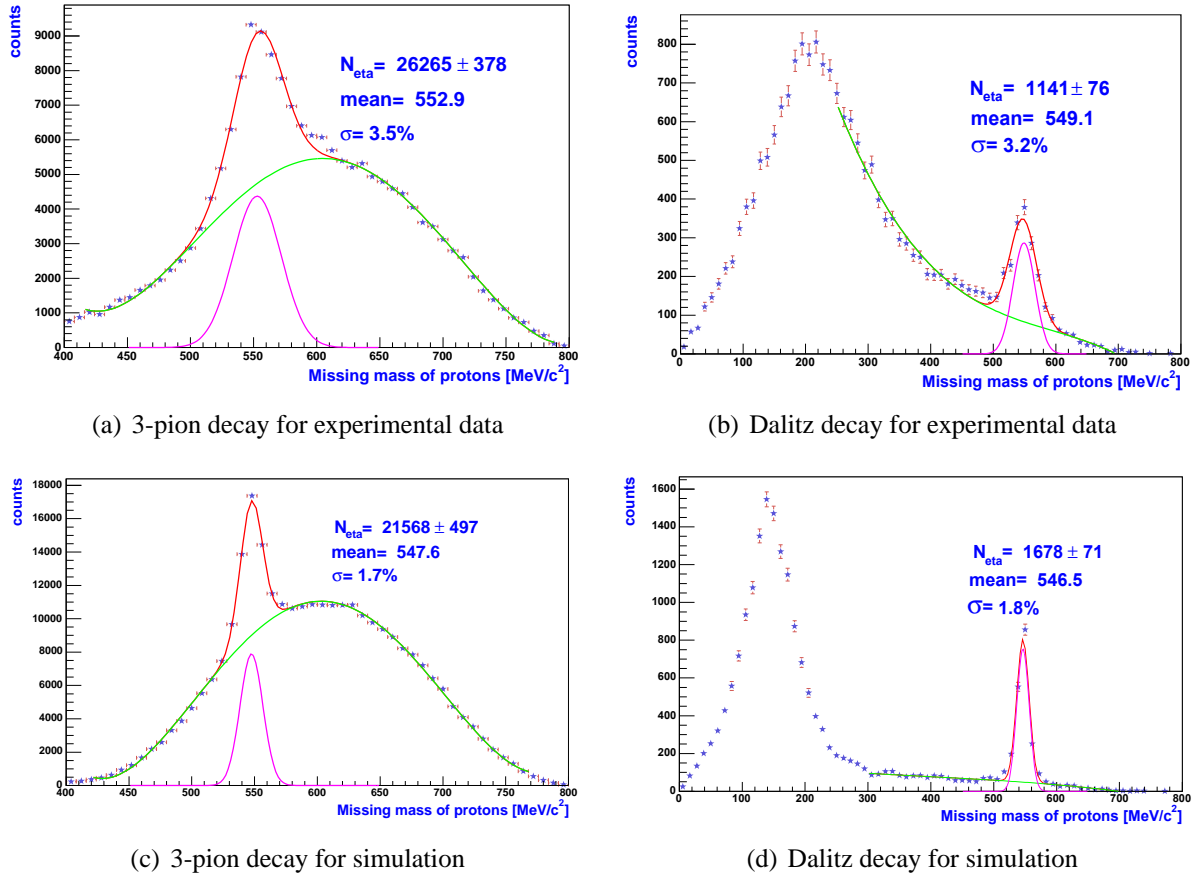


Figure 6.1: Missing-mass distributions of two protons before applying the kinematic fit algorithm; (a) for experimental data after applying a cut around π^0 peak in the missing-mass distributions of four particles, (b) for experimental data after applying a cut around γ peak in the missing mass distributions of four particles, (c) for simulation corresponding to the 3-pion decay of the η meson, and (d) for simulation corresponding to the Dalitz decay of the η meson.

The main goal of collecting these data was to investigate the spectrometer performance in terms of resolution, alignment and exclusively reconstruct the η mesons created well above the production threshold, in order to estimate the dilepton identification efficiency

of the HADES spectrometer. Besides these studies, the production mechanism of the eta mesons and its Dalitz decay were investigated as well.

6.0.1 Dilepton identification efficiency of the HADES spectrometer

The dilepton identification efficiency has been estimated by exclusive reconstruction of two decay channels of the η meson. In order to estimate the relative branching ratios of investigated decay channels inside the HADES acceptance a simulation has been done by taking into account all known processes at his energy. Furthermore different kinds of simulations containing pure η signal were performed in order to investigate the production mechanism of the η meson. In the simulation, we assumed resonant production of the η meson via $pp \rightarrow N^*(1535)p \rightarrow pp\eta$. For the Dalitz decay, the Vector Dominance Model (VDM) was assumed, while for the 3-pion decay phase space production has been assumed. In addition, a full cocktail of reaction channels based on measured proton-proton cross sections was produced.

Tables 6.1 and 6.2 summarizes the reconstructed numbers of η mesons for simulation and experimental data from its two decay channels, before and after the kinematic fit.

before kinematic fit		
	$N_{\eta \rightarrow \pi^+ \pi^- \pi^0}$	$N_{\eta \rightarrow e^+ e^- \gamma}$
Sim	21568 ± 497	1678 ± 71
Exp	26265 ± 378	1141 ± 76

Table 6.1: Number of reconstructed η mesons before the kinematic fit.

after kinematic fit		
	$N_{\eta \rightarrow \pi^+ \pi^- \pi^0}$	$N_{\eta \rightarrow e^+ e^- \gamma}$
Sim	21841 ± 472	1573 ± 65
Exp	28460 ± 341	1034 ± 64

Table 6.2: Number of reconstructed η mesons after the kinematic fit.

Using the results from table 6.2 we can estimate the relative ratio of reconstructed η mesons from its two decay channels for simulation and experimental data:

$$R_{sim} = 13.9 \pm 0.65 \quad (6.1)$$

and

$$R_{exp} = 22.6 \pm 1.44 \quad (6.2)$$

where R_{exp} was calculated using formula 5.15.

If we would reconstruct the dileptons with 100% efficiency from experimental data compared to the simulation the numbers in expressions 6.1 and 6.2 would be the same; therefore the relative ratio of these numbers can be an estimation of the dilepton identification efficiency of the spectrometer in the η region. From numbers in expressions 6.1 and 6.2 one can conclude that in experimental data we can reconstruct only 62% of the η mesons compared to simulation.

Similarly using the numbers from table 6.1 we obtain:

$$R_{sim} = 12.8 \pm 0.62 \quad (6.3)$$

and

$$R_{exp} = 18.9 \pm 1.3 \quad (6.4)$$

Using these numbers we obtain that in experimental data we can reconstruct only 68% of the η mesons compared to the simulation. The systematic shift of 6% between the results before and after the kinematic fit algorithm is partly connected to the accuracy of background estimation. Another reason is the systematic shift of the pion mass as well as the background in the missing-mass distributions of two protons for the η Dalitz decay before the kinematic fit (See Figure 6.1(b)). Finally we can conclude that in the η region we can reconstruct only 62% of dileptons with a systematic shift of +6%.

The η meson reconstruction procedure is briefly discussed below (for more details see chapter 5).

The analysis has started with the selection of events with at least 3 positively charged particles and one negatively charged particle. During this step the candidates containing 3 positive and one negative particles were created by taking each time one of the positively charged particles to be e^+ if there was a matching with the RICH detector or π^+ in the other case. During this procedure the negative particle was assumed to be an electron or negative pion depending on the matching with the RICH detector (See for details section 5.3.1). For the reaction selection the missing-mass distributions of four particles were investigated. The missing-mass distribution of $pp\pi^+\pi^-$ shows an evident peak for π^0 corresponding to $\eta \rightarrow \pi^+\pi^-\pi^0$, as shown in Figure 5.11(a). After imposing a cut around the pion peak the events corresponding to the 3-pion decay of the η were selected. By imposing this cut we get rid of the events where no missing particle is present, corresponding to the reaction $pp \rightarrow pp\pi^+\pi^-$, in which we are not interested.

In a similar way, by plotting a missing-mass distribution of ppe^+e^- events one can see an evident peak for the missing photon centered at 0 (See Figure 5.11(b)); by putting a cut around the γ peak the events corresponding to the Dalitz decay of the η meson were selected.

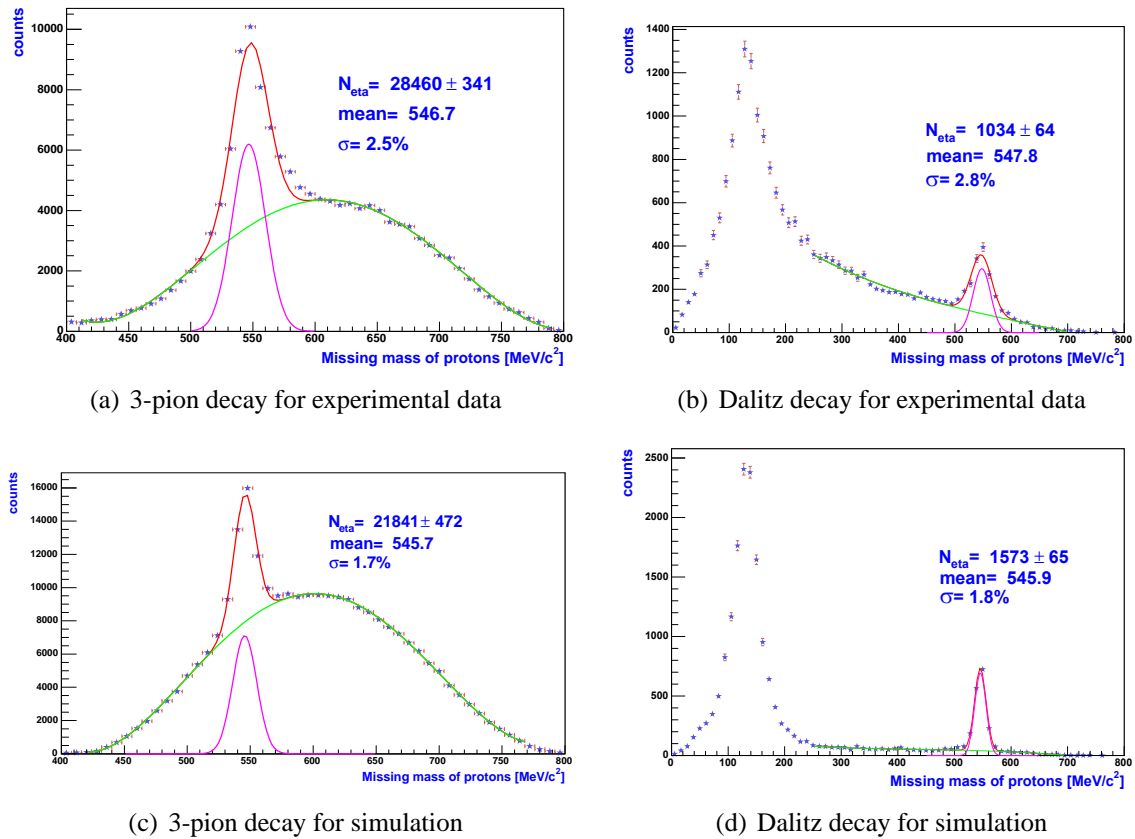


Figure 6.2: Missing-mass distributions of two protons after applying the kinematic fit algorithm; (a) for experimental data after applying a cut around π^0 peak in the missing-mass distributions of four particles, (b) for experimental data after applying a cut around γ peak in the missing mass distributions of four particles, (c) for simulation corresponding to the 3-pion decay of the η meson, and (d) for simulation corresponding to the Dalitz decay of the η meson.

After selecting the events corresponding to the above-mentioned two decay channels one can reconstruct the η mesons by plotting the missing-mass distributions of two protons. Figure 6.1(a) shows the missing mass distributions of two protons, after imposing a cut around π^0 peak in the missing-mass distribution of $pp\pi^+\pi^-$, corresponding to the 3-pion decay of the η meson. A prominent η peak, centered at the expected position, is clearly visible on top of a background coming mainly from non-resonant and resonant pion production. The η peak was fitted with a Gauss distribution plus a polynomial fit for the background. The number of reconstructed η mesons was estimated from the histogram counts above the background in Figure 6.1(a) due to the structure of the signal which can not be described by a Gauss function. This structure is due to the fact that the spectrometer was not fully set up at that time, and hence the reconstruction resolutions from the sectors with four and three MDC chambers are different. The reconstructed number of η mesons is equal to 26265 ± 378 . The η peak is centered around $553 \text{ MeV}/c^2$ with a resolution of 3.5%. In a similar way Figure 6.1(b) shows a missing-mass distribution of two protons after imposing a cut around the γ peak in the missing-mass distribution of ppe^+e^- , corresponding to the Dalitz decay of the η meson. The prominent peak centered around $549 \text{ MeV}/c^2$ corresponds to the reconstructed η mesons on top of the background coming mainly from multi-pion production. The reconstructed yield stems from two main mesons decays: the Dalitz decay of the type $X \rightarrow e^+e^-\gamma$ and two-photon decays $X \rightarrow \gamma\gamma$ followed by pair conversion of one of the decay photons (or both) in the target or by hitting some detector part. The yield was fitted with a Gauss distribution plus a polynomial fit for the background. The reconstructed number of η mesons from its Dalitz decay is equal to 1141 ± 76 . The η peak is centered around $549 \text{ MeV}/c^2$ with a resolution of 3.2%.

Figures 6.1(c) and 6.1(d) show the distributions of two-proton missing masses for 3-pion and the Dalitz decays of the η meson for simulation. The cuts imposed around the pion and photon peaks are the same in the simulation and experimental data. The reconstructed number of η mesons from the simulation is equal to 21568 ± 497 and 1678 ± 71 for its 3-pion and Dalitz decays, correspondingly. The width of the η signal is about 1.8%, both for the 3-pion and the Dalitz decays of the η meson for simulation.

In order to improve the tracking resolution and signal-to-background ratio, an algorithm of kinematic fit was developed using different constraints governing the decay processes. From a mathematical point of view the method varies the measured track parameters inside the corresponding error bars, until the required conditions are fulfilled. Only one condition was used for each decay channels: missing mass of four particles, $pp\pi^+\pi^-$, being equal to the π^0 mass for the 3-pion decay, and missing mass of ppe^+e^- being equal to 0 (photon mass). The method gives an improvement of the reconstructed mass resolution by a factor of 1.5 for the 3-pion and by a factor of 1.2 for the Dalitz decays of the η meson.

The obtained missing-mass distribution of two-protons for experimental data after the kinematic fit algorithm is shown in Figure 6.2(a) for 3-pion decay of the η meson. The η yield is fitted by a Gauss function plus a polynomial fit for a background. The reconstructed number of η mesons, performed by counting histogram counts above the background, is

equal to 28460 ± 341 . The η signal is centered around $547 \text{ MeV}/c^2$ with a resolution of 2.5%. Figure 6.2(b) shows the missing-mass distributions of two-protons for experimental data after the kinematic fit algorithm for the Dalitz decay of the η meson. The reconstructed number of the η mesons is equal to 1034 ± 64 . The η signal is centered around $547 \text{ MeV}/c^2$ with a resolution of 2.8%. The peak around $140 \text{ MeV}/c^2$ corresponds to the reconstructed π^0 mesons. As it is seen from Figure 6.2(b) the shift of the reconstructed π^0 mass observed in the two-proton missing-mass distributions before the kinematic fit algorithm (See Figure 6.1(b)) is gone after application of the kinematic fit algorithm. The corresponding two-proton missing-mass distributions for simulation are shown in Figures 6.2(c) and 6.2(d) for the 3-pion and the Dalitz decays of the η meson. The reconstructed numbers of the η mesons are equal to 21841 ± 472 and 1573 ± 65 for its 3-pion and the Dalitz decays, correspondingly.

6.0.2 η meson production

By fitting the pp missing-mass peak in various $\cos(\theta_{cm}^\eta)$ slices, the angular distribution of the η meson emission has been evaluated.

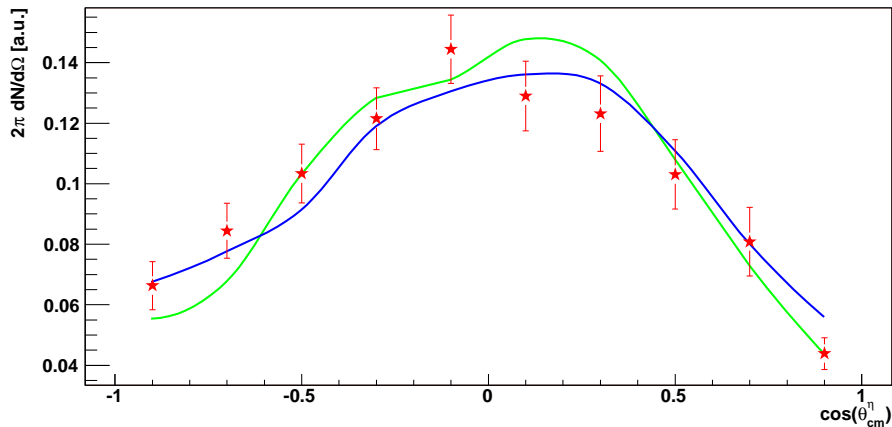


Figure 6.3: Angular distributions of η mesons in the center-of-mass system of the 2 protons. Red points are obtained from data, while blue and green lines are obtained from simulations through N_{1535}^* resonance with isotropic (blue) and anisotropic (green) angular distributions observed by the DISTO experiment.

In our simulations most of the parameters describing the η production and decay (matrix elements) have been fixed by information taken from other experiments. Therefore most of the degrees of freedom describing the $pp\eta$ final state are fixed (See section 5.2.1). Together with the fact that the beam axis has a rotational symmetry, only two angles are left for the alignment of the $pp\eta$ plane (See Figure 5.6). It was tested in simulations that

these parameters are not correlated, thus allowing us to compare directly 1-dimensional angular distributions without any multi-dimensional acceptance corrections.

The reconstructed angular distributions of the η mesons after the background subtraction is shown in Figure 6.3 (red points) together with two different model assumptions. Both models assume a production of the η meson through nucleon excitation $N^*(1535)$. In the first model (blue line) the isotropic η decay, while in the second model (green line) an anisotropic η decay observed by the DISTO experiment has been included. The results are consistent within the error bars with both models. The nice agreement between simulation and experimental distributions shows that the η mesons are mainly produced via $N^*(1535)$, as predicted by other experiments as well.

6.0.3 η meson decay

The Dalitz decay of the η meson was investigated by reconstructing the invariant-mass distribution of dileptons coming from the $\eta \rightarrow e^+e^-\gamma$ decay. To the η peak in the missing-mass distribution of two protons, besides the Dalitz decay of the η meson, the $\eta \rightarrow \gamma\gamma$ decay channel contributes as well. In order to suppress these events, several cuts have been used described in Section 5.4.4.

The matrix element of the Dalitz decay of the type $A \rightarrow Be^+e^-$ can be written as:

$$|M|^2 = |M(A \rightarrow B\gamma^*)|^2 \frac{1}{M^4} |M(\gamma^* \rightarrow e^+e^-)|^2. \quad (6.5)$$

This reflects in the differential decay rate, which can be written as a product of the conversion rate of the virtual gamma and the decay width $\Gamma_{A \rightarrow B\gamma^*}$ of A into a massive photon:

$$\frac{d\Gamma_{A \rightarrow Be^+e^-}}{dM} = \frac{2\alpha}{3\pi M} \sqrt{1 - \frac{4m_e^2}{M^2}} \left(1 + \frac{2m_e^2}{M^2}\right) \Gamma_{A \rightarrow B\gamma^*}. \quad (6.6)$$

the $A \rightarrow B\gamma^*$ width is given by

$$\Gamma_{A \rightarrow B\gamma^*} = \frac{|\vec{p}_{cm}|}{8\pi m_A^2} |M_{A \rightarrow B\gamma^*}|^2. \quad (6.7)$$

Here $|\vec{p}_{cm}|$ is the decay momentum

$$|\vec{p}_{cm}| = \frac{\lambda^{\frac{1}{2}}(m_A^2, m_B^2, M^2)}{2m_A} \quad (6.8)$$

with the kinematic function

$$\lambda(x^2, y^2, z^2) = (x^2 - (y+z)^2)(x^2 - (y-z)^2). \quad (6.9)$$

The matrix element $|M_{A \rightarrow B\gamma^*}|$ can be calculated as:

$$|M_{A \rightarrow B\gamma^*}|^2 = \frac{1}{2} |f_{AB}(M^2)|^2 \lambda(m_A^2, m_B^2, M^2). \quad (6.10)$$

The form factor $f_{AB}(M^2)$ is introduced to account for the strong interaction part of the vertex. It is common to normalize to the decay width into real photons:

$$\Gamma_{A \rightarrow B\gamma} = \frac{(m_A^2 - m_B^2)^3}{32\pi m_A^3} |f_{AB(0)}|^2, \quad (6.11)$$

which re-expresses the form factor to

$$F_{AB}(M^2) = \frac{f_{AB}(M^2)}{f_{AB(0)}} \quad (6.12)$$

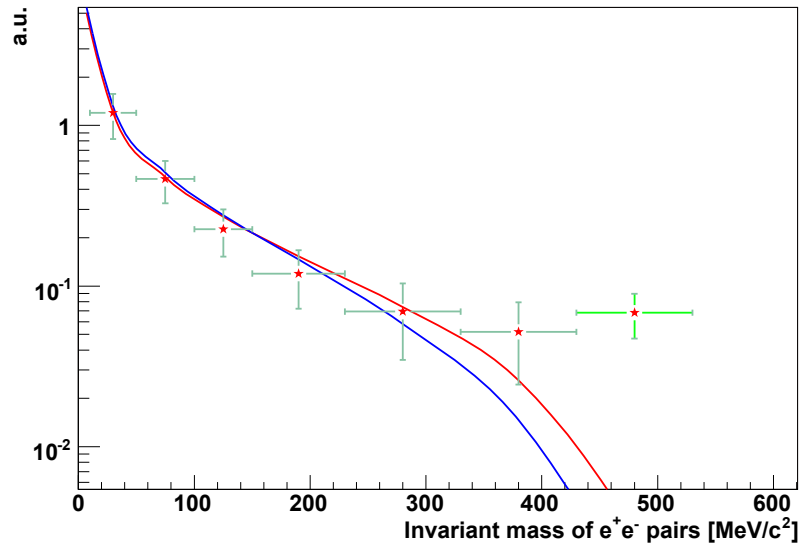
The form factor can be obtained from the vector meson dominance model (VDM). The following parametrization of the form factor of the η meson is commonly used:

$$F_\eta(M^2) = \left(1 - \frac{M^2}{\Lambda_\eta^2}\right)^{-1} \quad (6.13)$$

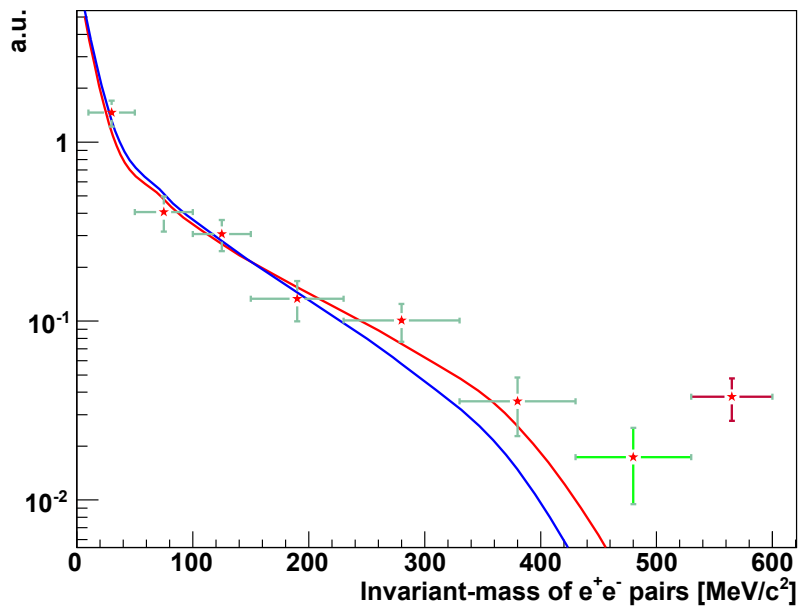
with $\Lambda_\eta=0.72$ GeV.

Figure 6.4(a) shows the reconstructed invariant-mass distribution of e^+e^- pairs from η Dalitz decay after background subtraction. The red line corresponds to the calculations with Equation 6.6 with the form factor parameterized by formula 6.13. The blue line corresponds to the pure QED calculations which is obtained also from formula 6.6 by putting the form factor equal to 1.

As it is seen from the Figure, within error bars, the VDM model describes the decay quite well. The discrepancy of the last bin from the VDM calculations was investigated using different methods for background subtraction. These investigations have shown that two different methods are giving similar results. It was shown that the background behavior in this bin can not be easily described. Therefore the discrepancy is coming from the inaccuracy of the background estimation in this bin. By reconstructing the e^+e^- invariant-mass distribution from the simulation (See Figure 6.4(b)), it was found that this bin has a similar behavior. As in the simulation we assumed the decay with VDM hypothesis the discrepancy may come only from the background estimation or fake track contributions.



(a) real data



(b) simulation

Figure 6.4: Invariant-mass distribution of e^+e^- pairs from the Dalitz decay of the η meson for real data (a) and for simulation (b). Red line corresponds to the VDM model calculations, while the blue line represents the pure QED calculations.

By comparing the e^+e^- invariant-mass distributions from simulation and experimental data, it was realized that in case of simulation there are pairs with invariant masses around the pole mass of the η meson (See Figure 6.4(b))¹. These pairs correspond to the direct decays of the η meson which is suppressed. The fact that these counts do not exist in the e^+e^- invariant-mass distribution from experimental data (See Figure 6.4(a)), together with the fact that the analyzed statistics is more for experimental data shows that the lower limit on the branching ratio of the $\eta \rightarrow e^+e^-$ decay channel is lower, than presented in [76]. One should mention that in simulation for the direct decay of the η mesons into e^+e^- pairs the branching ratio was taken from [76].

In 2007 a proton-proton run at 3.5 GeV will be taken with much more statistics. During this run the main emphasis will be put to the investigation of the ω meson decay. Furthermore the investigation of the η Dalitz decay will be repeated with high statistics as well with that data.

This investigation has shown that the HADES spectrometer can be used to investigate elementary collisions as well. The high resolution tracking which uses information from all four MDCs, is working properly. However, there are still some problems especially concerning the alignment of the magnetic field which are under investigation.

6.0.4 Investigation of the spectrometer performance using elastic scattering

The elastic proton-proton scattering was investigated to understand the spectrometer performance in terms of alignment and reconstruction resolution. The reaction selection is based on the kinematics of the elastic scattering (See section 4.2). As the kinematics of the elastic scattering is fully characterized by two parameters (See section 4.1), it was possible to estimate the momentum reconstruction resolution of the spectrometer in each sector separately by measuring the polar angle of the track and comparing the reconstructed momentum with the calculated one from kinematical relations (See Appendix B). The elastic scattering is also used to investigate the alignment of the magnetic coils with respect to MDC chambers. For the sectors equipped with all four MDC chambers the momentum resolution obtained from these analyzes is about 4% on average (See Figures 4.6). For the sector with 3 MDC chambers, the obtained momentum resolution is about 7%. However these resolutions are also affected by angular resolution as well, because for calculation of the momentum using elastic scattering kinematics the angular information is used (See appendix B). Furthermore the resolutions are obtained for the momentum range between 600MeV/c to 2500 MeV/c. The obtained resolution distributions have shown systematic shifts as a function of sector numbers as shown in Figures 4.7. This indicates that the alignment procedure must still be improved.

¹For details see section 5.7.

Appendix A

Lorentz transformations

A relativistic particle is fully characterized by its mass m and velocity β . The energy E and momentum \mathbf{p} are defined as:

$$E = \frac{m}{\sqrt{1 - \beta^2}} = m\gamma \quad (\text{A.1})$$

$$\mathbf{p} = \frac{m\beta}{\sqrt{1 - \beta^2}} = m\beta\gamma \quad (\text{A.2})$$

where $\gamma = \frac{1}{\sqrt{1 - \beta^2}}$

There is another representation of β , γ and η with hyperbolic functions:

$$\begin{aligned} \beta &= \tanh y \\ \gamma &= \cosh y \\ \eta &= \sinh y \end{aligned} \quad (\text{A.3})$$

with $\eta = \gamma\beta$

Let us define a 4-vector as

$$p = \begin{pmatrix} E \\ p_x \\ p_y \\ p_z \end{pmatrix} \quad (\text{A.4})$$

where E and \vec{p} are the energy and 3-momentum of a particle in the LAB frame.

The energy and momentum (E^*, \vec{p}^*) viewed from the CM frame which is moving with a velocity β_{cm} in z direction are given by

$$\begin{pmatrix} E^* \\ p_x^* \\ p_y^* \\ p_z^* \end{pmatrix} = \begin{pmatrix} \gamma & 0 & 0 & -\gamma\beta \\ 0 & 1 & 0 & 0 \\ 0 & 0 & 1 & 0 \\ -\gamma\beta & 0 & 0 & \gamma \end{pmatrix} \begin{pmatrix} E \\ p_x \\ p_y \\ p_z \end{pmatrix} \quad (\text{A.5})$$

For the backward transformation, i.e from CM frame to LAB, one should use instead of β_{cm} a $-\beta_{cm}$ in A.5

$$\begin{pmatrix} E \\ p_x \\ p_y \\ p_z \end{pmatrix} = \begin{pmatrix} \gamma & 0 & 0 & \gamma\beta \\ 0 & 1 & 0 & 0 \\ 0 & 0 & 1 & 0 \\ \gamma\beta & 0 & 0 & \gamma \end{pmatrix} \begin{pmatrix} E^* \\ p_x^* \\ p_y^* \\ p_z^* \end{pmatrix} \quad (\text{A.6})$$

Taking into account relations A.3 one can write the above transformation as:

$$\begin{pmatrix} E \\ p_x \\ p_y \\ p_z \end{pmatrix} = \begin{pmatrix} \cosh y & 0 & 0 & \sinh y \\ 0 & 1 & 0 & 0 \\ 0 & 0 & 1 & 0 \\ \sinh y & 0 & 0 & \cosh y \end{pmatrix} \begin{pmatrix} E^* \\ p_x^* \\ p_y^* \\ p_z^* \end{pmatrix} \quad (\text{A.7})$$

From a geometrical point of view Lorentz transformations are rotations in Ep_x , Ep_y , Ep_z planes. In our particular case, when the CM frame moves in z direction, the Lorentz transformation can be represented by a rotation in the Ep_z plane by an angle χ defined as:

$$\tanh \chi = i\beta \quad (\text{A.8})$$

Since $\tanh y = \beta$, an angle χ is related to rapidity as: $\chi = iy$

In practice it is sometimes useful to decompose momentum into two components: longitudinal p_{\parallel} (along β direction) and transverse p_{\perp} (perpendicular to β direction).

$$\begin{aligned} p &= p_{\parallel} + p_{\perp} \\ p^* &= p_{\parallel}^* + p_{\perp}^* \end{aligned} \quad (\text{A.9})$$

In these notations 4-momenta are written as:

$$\begin{pmatrix} E \\ 0 \\ p_{\perp} \\ p_{\parallel} \end{pmatrix} = \begin{pmatrix} E \\ 0 \\ p \sin \theta \\ p \cos \theta \end{pmatrix} \quad (\text{A.10})$$

where θ is the angle between the momentum vector and β in corresponding reference system. In other words, we did a transformation into spherical coordinates (p, θ, ϕ) .

The azimuthal angle under Lorentz transformation is not changing.

$$\phi = \phi^* \quad (\text{A.11})$$

From A.6 we have

$$\begin{pmatrix} E \\ 0 \\ p_{\perp} \\ p_{\parallel} \end{pmatrix} = \begin{pmatrix} \gamma & 0 & 0 & \gamma\beta \\ 0 & 1 & 0 & 0 \\ 0 & 0 & 1 & 0 \\ \gamma\beta & 0 & 0 & \gamma \end{pmatrix} \begin{pmatrix} E^* \\ 0 \\ p_{\perp}^* \\ p_{\parallel}^* \end{pmatrix} \quad (\text{A.12})$$

Appendix B

Kinematics of elastic scattering

Here we will derive some important kinematical relations for elastic scattering in both laboratory (LAB) and center-of-mass frames (CM).

The reference system attached to the laboratory of the user is called LAB system. Sometimes in the experiment the beam of particles is directed onto the target at rest, therefore the LAB system will be just the rest system of a target particle.

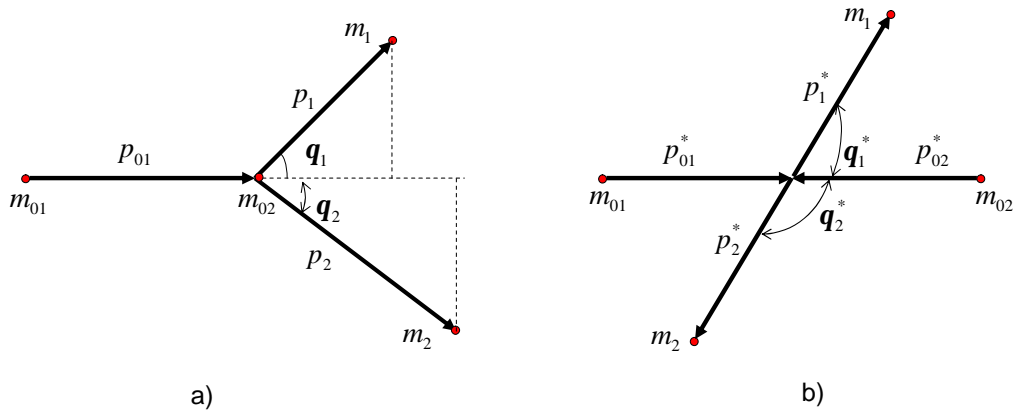


Figure B.1: Kinematics of elastic scattering in (a) LAB and (b) center of mass system of two protons.

The second most often used system is the center-of-mass system where the vector sum of all momenta particles taking part in a reaction equals 0.

The motion of the center of mass system of particles is equivalent to the motion of some quasi particle with an energy:

$$E = \sum E_i \tag{B.1}$$

and momentum

$$p = \sum p_i \quad (\text{B.2})$$

with the mass being equal to the total center-of-mass energy

$$M = S = \sqrt{\left(\sum E_i\right)^2 - \left(\sum p_i\right)^2} \quad (\text{B.3})$$

giving

$$\beta_{cm} = \frac{p}{E} = \frac{\sum p_i}{\sum E_i} \quad (\text{B.4})$$

Let us derive some kinematic relations for the reaction

$$a_{01} + a_{02} = a_1 + a_2 \quad (\text{B.5})$$

with four momentum being p_{01}, p_{02}, p_1 , and p_2 respectively. In addition we will assume that in B.5 that all particles are identical with mass m .

In the CM frame, from momentum conservation law we have:

$$\begin{aligned} E_1^* + E_2^* &= M \\ \vec{p}_1^* + \vec{p}_2^* &= 0 \end{aligned} \quad (\text{B.6})$$

with M defined in B.3. The second line of B.6 tells us that in CM frame the outgoing particles have the same momentum moving in opposite directions.

from B.1,B.2,B.3,B.4 one can easily get

$$\begin{aligned} S &= \sqrt{2m(E_{01} + m)} \\ \beta_{cm} &= \frac{p_{01}}{E_{01} + m} = \sqrt{\frac{\gamma_{01} - 1}{\gamma_{01} + 1}} \\ \gamma_{cm} &= \sqrt{\frac{E_{01} + m}{2m}} = \sqrt{\frac{\gamma_{01} + 1}{2}} \end{aligned} \quad (\text{B.7})$$

The relation between momenta and energies of the particles in these two reference systems are:

$$\begin{aligned} E_{01}^* = E_{02}^* &= \frac{\sqrt{s}}{2} = \sqrt{\frac{m(E_{01} + m)}{2}} = m * \gamma_{cm} \\ p_{01}^* = p_{02}^* &= \sqrt{\frac{m(E_{01} - m)}{2}} = m \sqrt{\frac{\gamma_{01} - 1}{2}} \end{aligned} \quad (\text{B.8})$$

From A.6 and A.9 we have

$$\begin{aligned} p_{\parallel} &= p \cos(\theta) = \gamma p^* \cos \theta^* + \gamma \beta E^* \\ p_{\perp} &= p \sin \theta = p^* \sin \theta^* \end{aligned} \quad (\text{B.9})$$

It is clear from the definitions of p_{\parallel} and p_{\perp} that

$$\tan \theta = \frac{p_{\perp}}{p_{\parallel}} \quad (\text{B.10})$$

Taking into account B.9 in B.10 we have

$$\tan \theta = \frac{p^* \sin \theta^*}{\gamma_{cm}(p^* \cos \theta^* + \beta_{cm} E^*)} = \frac{1}{\gamma_{cm}} \frac{\sin \theta^*}{\cos \theta^* + \frac{\beta_{cm}}{\beta^*}} \quad (\text{B.11})$$

In elastic scattering of identical particles $\frac{\beta_{cm}}{\beta^*} = 1$ therefore we can rewrite B.11 as:

$$\tan \theta_1 = \frac{1}{\gamma_{cm}} \frac{\sin \theta^*}{1 + \cos \theta^*} = \frac{1}{\gamma_{cm}} \tan \frac{\theta_1^*}{2} \quad (\text{B.12})$$

$$\tan \theta_2 = \frac{1}{\gamma_{cm}} \tan\left(\frac{\pi}{2} - \frac{\theta_1^*}{2}\right) = \frac{1}{\gamma_{cm}} \coth \frac{\theta_1^*}{2}$$

In B.12 the relation $\theta_1^* + \theta_2^* = \pi$ was taken into account (See Figure B.1)
Multiplication of the two lines in B.12 gives

$$\tan \theta_1 * \tan \theta_2 = \frac{1}{\gamma_{cm}^2} \quad (\text{B.13})$$

One can write the momentum conservation law for the reaction B.5 as :

$$\begin{aligned} p_1 \sin(\theta_1) - p_2 \sin(\theta_2) &= 0 \\ p_1 \cos(\theta_1) + p_2 \cos(\theta_2) &= p_{01} \end{aligned} \quad (\text{B.14})$$

solving this equations against p_1 yields:

$$p_1 = \frac{p_{01}}{\cos \theta_1} - \frac{p_1 \tan^2 \theta_1}{\tan \theta_2 \tan \theta_1} \quad (\text{B.15})$$

Finally taking into account B.13 in B.15 we can express the momentum of the outgoing particle as a function of its polar angle:

$$p_1 = \frac{p_{01}}{\cos(\theta_1) [1 + \tan^2(\theta_1) \gamma_{cm}^2]} \quad (\text{B.16})$$

Appendix C

Formulas for kinematic fit

From a mathematical point of view the kinematic fit means finding of a parameters $\tilde{\alpha}$ which gives a minimum of the function:

$$F_1 = \sum_{i=1}^n (\alpha_i - \tilde{\alpha}_i)^T W^{-1} (\alpha_j - \tilde{\alpha}_j) + \sum_{k=1}^s \lambda_k H_k \quad (\text{C.1})$$

where W^{-1} is the inverse of the measured covariance matrix, sometimes referred to as a weight matrix, α and $\tilde{\alpha}$ are track parameters before and after the kinematic fit algorithm, H_k are constraint equations and λ_k are Lagrange multipliers.

The minimization procedure consists of two steps:

- Finding of a first approximation for parameters
- Using least squares fit with constraints to minimize the function C.1

In order to find a first approximation for the track parameters we use so called helper function defined as:

$$F_2 = \sum_{i=1}^n \left(\frac{\alpha_i - \alpha_i(T)}{\sigma_{\alpha_i}} \right)^2 + T \sum_{k=1}^s \frac{H_k^2}{(\Delta H_k)^2} \quad (\text{C.2})$$

where $(\Delta H_k)^2$ is:

$$(\Delta H_k)^2 = \sum_{i=1}^{i=N} \left(\frac{\partial H_k}{\partial \alpha_i} \sigma_{\alpha_i} \right)^2 \quad (\text{C.3})$$

and parameter T is fixed according to the reaction channel under investigation.

When $T \rightarrow \infty$ the minimum of functions C.1 and C.2 can be described by the same set of parameters α_i . That is why it is assumed that the parameters corresponding to the

minimum of function C.1 will be in close vicinity of the parameters found by minimization of the helper function C.2.

The minimization procedure is based on least squares fitting with constraints, according to which the minimum of the function C.1 can be found by equating of all the partial derivatives of the function C.1 with respect to each parameter to 0:

$$\frac{\partial F_1}{\partial \alpha_i} = 0 \quad (\text{C.4})$$

We will derive the formulas by taking into account only diagonal elements of a covariance matrix.

We can write the conditions C.4 in a matrix form as:

$$\begin{pmatrix} \frac{1}{(\sigma_{\alpha_1})^2} & 0 & \dots & 0 & 0 \\ 0 & \frac{1}{(\sigma_{\alpha_2})^2} & \dots & 0 & 0 \\ \dots & \dots & \dots & \dots & \dots \\ \dots & \dots & \dots & \dots & \dots \\ \dots & \dots & \dots & \dots & \dots \\ 0 & 0 & \dots & \frac{1}{(\sigma_{\alpha_{n-1}})^2} & 0 \\ 0 & 0 & \dots & 0 & \frac{1}{(\sigma_{\alpha_n})^2} \end{pmatrix} \begin{pmatrix} \alpha_1 - \tilde{\alpha}_1 \\ \alpha_2 - \tilde{\alpha}_2 \\ \dots \\ \dots \\ \dots \\ \alpha_{n-1} - \tilde{\alpha}_{n-1} \\ \alpha_n - \tilde{\alpha}_n \end{pmatrix} = \begin{pmatrix} \lambda_k \frac{\partial H_k}{\partial \alpha_1} \\ \lambda_k \frac{\partial H_k}{\partial \alpha_2} \\ \dots \\ \dots \\ \dots \\ \lambda_k \frac{\partial H_k}{\partial \alpha_{n-1}} \\ \lambda_k \frac{\partial H_k}{\partial \alpha_n} \end{pmatrix} \quad (\text{C.5})$$

Let us denote by $\alpha_i(T)$ the values of the parameters giving the minimum of the helper function C.2. As it was stated before these parameters can be considered as a first approximation for the minimum of the function C.1. Therefore we can use a Taylor expansion for the constraints around these parameters:

$$H_k(\tilde{\alpha}_1, \tilde{\alpha}_1, \dots, \tilde{\alpha}_n) = H_k(T) + \sum_{i=1}^n \frac{\partial H_k}{\partial \alpha_i} (\tilde{\alpha}_i - \alpha_i(T)) \quad (\text{C.6})$$

by definition we have

$$H_k(\tilde{\alpha}_1, \tilde{\alpha}_1, \dots, \tilde{\alpha}_n) = 0 \quad (\text{C.7})$$

hence,

$$H_k(T) = - \sum_{i=1}^n \frac{\partial H_k}{\partial \alpha_i} (\tilde{\alpha}_i - \alpha_i(T)) \quad (\text{C.8})$$

from Equations C.5 we have

$$\tilde{\alpha}_i = \alpha_i - \sum_{k=1}^{k=s} \lambda_k \frac{\partial H_k}{\partial \alpha_i} \sigma_i^2 \quad (\text{C.9})$$

Taking into account C.9 in C.8 we have

$$\sum_{i=1}^n \frac{\partial H_k}{\partial \alpha_i} \sum_{k=1}^s \lambda_k \frac{\partial H_k}{\partial \alpha_i} \sigma_i^2 = H_k(T) + \sum_{i=1}^n \frac{\partial H_k}{\partial \alpha_i} (\alpha_i - \alpha_i(T)) \quad (\text{C.10})$$

The last equation can be written as a set of linear equations, which can be solved with Cramer's determinants method against λ_k :

$$\lambda_k = \frac{|X(k)|}{|X|} \quad (\text{C.11})$$

where X is the matrix of coefficients of λ_k 's
and X(k) is obtained from X by substituting column number k with

$$H_k(T) + \sum_{i=1}^n \frac{\partial H_k}{\partial \alpha_i} (\alpha_i - \alpha_i(T)) \quad (\text{C.12})$$

By substituting found λ_k 's from C.11 into C.9 we define the parameters from kinematic fit.

Obtaining a solution is not enough: we also want to know the errors of the parameters. In order to find the uncertainty in the estimation of the parameters $\tilde{\alpha}$ in our fitting procedure, we use error propagation method. Each of our data points α has been used in the determination of the parameters and each has contributed some fraction of its own uncertainty to the uncertainty in our final determination.

$$\sigma_{\tilde{\alpha}_j}^2 = \sum_{i=1}^n \sigma_{\alpha_i}^2 \left(\frac{\partial \tilde{\alpha}_j}{\partial \alpha_i} \right) \quad (\text{C.13})$$

Appendix D

Data levels

The main goal of HADES software framework, is to reconstruct the events ¹ recorded by the HADES spectrometer which means an application of various algorithms to transform the *row* data delivered by the HADES into elaborated data, ready for the analysis steps.

The reconstruction proceeds in steps; each algorithm reads some input data may be the output from another algorithm, and takes it to a new level. In this sense we speak of different data levels. The first data level is the so called *raw* data, corresponding directly to the electronic signals recorded by the spectrometer. The next level is called calibrated data. The algorithm going from row data to calibrated data is detector specific and generally known as a *calibrator*.

The information obtained from MDCs are hardware addresses where the signal was generated and TDC counts. After the *unpacking*, a data level called *row* is filled. The next data level is called *MDCall* and is obtained from *raw* data level through a calibration procedure. The first calibration step translates the hardware addresses into module and cell numbers. The information from TDCs are transformed to drift times in nanoseconds using a linear function interpolation for extraction of a TDC gain from special calibration events. Besides of this in the calibration procedure the time offsets are also determined in order to remove from the measured time the part that does not correspond to the drift time (the part corresponding to time of flight of the particle) [77]. This offset subtraction was done in a global way for each TDC channel by fitting with the linear function the edge of the integrated time spectrum the crossing point of which with the integrated background as shown in Figure D.1 defines the global time offset; therefore the global offset correction removes from the measured drift time the time corresponding to the fastest particle which passes the cell closest to the wire.

During the track finding and fitting two things should be taken into account:

¹The event holds all the information collected by the different detectors in the spectrometer regarding one interaction between beam particle and the target; moreover it also stores the totally or partially reconstructed data which are derived from the original signal; there can be different kind of events: real events, simulated events, calibration events.

- propagation of the signal through wire
- the fact that all drift times are measured with respect to the fastest particle drift time

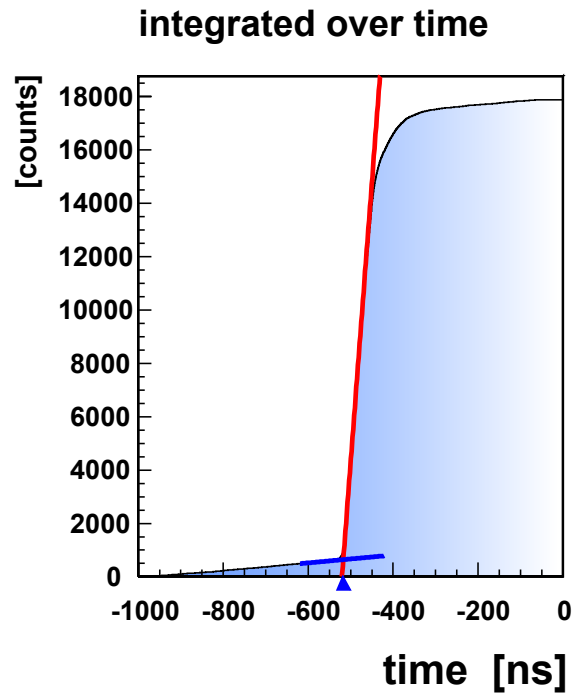


Figure D.1: Global time offset determination

Appendix E

Spline interpolation

As described in Section 3.8 we assume a cubic spline model for the track's second derivative, and as an input we take the following function

$$\frac{d^2Y}{dz^2} \equiv A(z)$$

with conditions

$$Y(z_0) = Y'(z_0) = 0$$

The Taylor series for a cubic polynomial $A(z)$ for interval $[z_i, z_{i+1}]$ expanded around the point z_i can be written as:

$$A(z) = A_i + (z - z_i) \frac{dA_i}{dz} + \frac{1}{2!} (z - z_i)^2 \frac{d^2A_i}{dz^2} + \frac{1}{3!} (z - z_i)^3 \frac{d^3A_i}{dz^3} \quad (\text{E.1})$$

where the function and derivatives are evaluated at z_i . The expression E.1 can be written in more concise way as

$$A(z) = A_i + (z - z_i)A'_i + \frac{1}{2}(z - z_i)^2A''_i + \frac{1}{6}(z - z_i)^3 \frac{(A''_{i+1} - A''_i)}{D_i} \quad (\text{E.2})$$

where A' and A'' stand for the first and second derivatives evaluated at $z = z_i$ and the third derivative has been replaced by its divided difference form, which is exact for a cubic function and $D_i = z_{i+1} - z_i$.

For $A(z)$ to be continuous we want

$$A_{i+1} = A_i + D_iA'_i + \frac{1}{2}D_i^2A''_i + \frac{1}{6}D_i^2(A''_{i+1} - A''_i) \quad (\text{E.3})$$

From the last equation we have

$$A'_i = \frac{A_{i+1} - A_i}{D_i} - \frac{1}{2}D_i A''_i - \frac{1}{6}D_i A''_{i+1} + \frac{1}{6}D_i A''_i \quad (\text{E.4})$$

And after some simplification of the last equation

$$A'_i = \frac{(A_{i+1} - A_i)}{D_i} - \frac{1}{3}D_i A''_i - \frac{1}{6}D_i A''_{i+1} \quad (\text{E.5})$$

Let us differentiate the equation E.2 at z_{i+1} (substitute z by z_{i+1} after differentiation)

$$A'_{i+1} = A'_i + \frac{1}{2}D_i A''_i + \frac{1}{2}D_i A''_{i+1} \quad (\text{E.6})$$

In the last equation we substitute an expression for A'_i from E.5 giving

$$A'_{i+1} = \frac{A_{i+1} - A_i}{D_i} - \frac{1}{3}D_i A''_i - \frac{1}{6}D_i A''_{i+1} + \frac{1}{2}D_i A''_i + \frac{1}{2}D_i A''_{i+1} \quad (\text{E.7})$$

On the other hand if we evaluate an expression E.5 at $i+1$ we have

$$A'_{i+1} = \frac{(A_{i+2} - A_{i+1})}{D_{i+1}} - \frac{1}{3}D_{i+1} A''_{i+1} - \frac{1}{6}D_{i+1} A''_{i+2} \quad (\text{E.8})$$

The left hand sides of E.7 and E.8 being equal we equate the write hand sides of them and take all differentials to one side

$$\frac{1}{6}D_i A''_i + A''_{i+1} \left(\frac{1}{3}D_i + \frac{1}{3}D_{i+1} \right) + \frac{1}{6}D_{i+1} A''_{i+2} = \left(\frac{A_{i+2} - A_{i+1}}{D_{i+1}} - \frac{A_{i+1} - A_i}{D_i} \right) \quad (\text{E.9})$$

Multiplication of the last equation by 3 and division by $(D_i + D_{i+1})$ yields

$$\frac{D_i}{2(D_i + D_{i+1})} A''_i + A''_{i+1} + \frac{D_{i+1}}{2(D_{i+1} + D_i)} A''_{i+2} = 3 \left(\frac{A_{i+2} - A_{i+1}}{D_{i+1}} - \frac{A_{i+1} - A_i}{D_i} \right) (D_i + D_{i+1})^{-1} \quad (\text{E.10})$$

The obtained equations E.10 are system of linear equations with the unknown second derivatives. As it can be seen from the expression we have $N-2$ equations and N second derivatives (unknowns). The equations can be solved as soon as we now the values of A''_1 and A''_N . One possibility is to set the second derivatives to 0 to obtain *natural splines*.

We choose for $A(x)$ the third order cubic spline so that we assume $A''_1 = A''_2$ and $A''_{N-1} = A''_N$. After this conditions we have N equations and N unknowns which can be solved by using Cramers Determinants method. The first derivatives are evaluated then using E.5. After substituting the found first and second derivatives into E.3 we have fully defined spline curve.

To evaluate the determinant each time may be time consuming therefore by taking $A''_i = P_i A''_{i+1} + Q_i$ we get the recursive relations from E.10

$$P_{i+1} = -t_2/(1 + t_1 P_i) \quad (E.11)$$

$$Q_{i+1} = (R_i - t_1 Q_i)/(1 + t_1 P_i)$$

where

$$\begin{aligned} t_1 &= D_i [2(D_i + D_{i+1})]^{-1} \\ t_2 &= D_{i+1} [2(D_i + D_{i+1})]^{-1} \end{aligned} \quad (E.12)$$

and R_i the right hand side of E.10. Starting with $P_1 = 1, Q_1 = 0$ and the equations E.10 can now be solved and then A_i'' can be determined from E.11 starting with $A_N'' = Q_{N-1}(1 - P_{N-1})^{-1}$.

E.1 Solution of field equations using cubic spline

To solve the field equations

$$p \frac{d^2 y}{dz^2} = k(z) \left[B_x \left(1 + \left(\frac{dy}{dz} \right)^2 \right) - B_y \frac{dx}{dz} \frac{dy}{dz} - B_z \frac{dx}{dz} \right] \quad (E.13)$$

$$p \frac{d^2 x}{dz^2} = k(z) \left[B_x \frac{dy}{dz} \frac{dx}{dz} - B_y \left(1 + \left(\frac{dx}{dz} \right)^2 \right) + B_z \frac{dy}{dz} \right]$$

we perform a cubic spline fit on the evaluated right hand sides of E.13 as in E.2 with the aim to calculate the double integrals

$$Y(z_i) = \int_{u=z_0}^{u=z_i} \left[\int_{v=z_0}^{v=u} A(v) dv \right] du \quad (E.14)$$

$$X(z_i) = \int_{u=z_0}^{u=z_i} \left[\int_{v=z_0}^{v=u} C(v) dv \right] du$$

Here we will show the solution only for the first integral of E.14. The second one is obtained in analogous way.

To get the first integrals $\int A(z) dz = Y'(z)$ integrate E.2 for corresponding functions $A(z)$ and after elimination of A' using E.5 we get

$$Y'_{i+1} = Y'_i + \frac{1}{2} D_i (A_{i+1} + A_i) - \frac{1}{24} D_i^3 (A_i'' + A_{i+1}'') \quad (E.15)$$

with $Y'_1 = 0$.

To get the double integral we integrate E.2 for corresponding functions twice and after eliminations of A' according to E.5 we get

$$Y_{i+1} = Y_i + Y'_i D_i + \frac{1}{6} D_i^2 (2A_i + A_{i+1}) - \frac{1}{36} D_i^4 (0.8A_i'' + 0.7A_{i+1}'') \quad (E.16)$$

with $Y_1 = 0$.

Appendix F

Software implementation

The software framework of the HADES spectrometer is called HYDRA. It is developed using the Object Oriented C++ programming language. The central class of the Hydra framework is the HADES class which encapsulates the whole reconstruction program, coordinating all Hydra subsystems. There must be one and only one instance of this class active at the same time. There are two ways to access this object, either by the *gHADES* global pointer or the *HADES::instance()* method¹. This class contains objects of different classes which it uses to implement the different subsystems. Since the reconstruction process is done event per event, the basic data structure is the event. An event is represented by an *HEvent* object. Within the *HEvent* data are organized in categories which are containers of objects. In this sense the *HEvent* is the container of categories. When we speak about a category of a given class, we mean the container holding the instances of that class. The interface for accessing the data inside categories is defined by the *HCategory* abstract class, all the other categories being inherited from this class. The *HCategory* interface provides different functions to access the data inside the categories

- Random access
- Sequential access

The random access means that one can access one particular object inside the category. Each object in the category is identified by an array of integers which are presented as an object inheriting from *HLocation* class. The corresponding function in the interface is *HCategory::getObject(HLocation & loc)*. It is also possible to access one object in the category giving only one index with the function *HCategory::getObject(int index)*.

Sequential access means to loop over a set of objects in the category and is performed using iterators. Iterators are objects created from the categories themselves by invoking the *HCategory::makeIterator()* method. The method *HIterator::Next()* keeps returning one

¹The second one is recommended.

object after the other in the container, until no objects are left and from there on it returns NULL.

For each event certain algorithm is performed (e.g. track finding, track fitting, momentum reconstruction and so on) which will be given a common name, task, represented by an *HTask* object. *HReconstructor* and *HTaskset* are two particular subclasses inheriting from *HTask*. The first one is meant for reconstruction algorithms, while the second one allows to group several tasks into one.

From a software point of view the main task for the track finder is *HMdcTrackFinder* which inherits from *HReconstructor* and takes an input information from category of *HMdcCall* class as it is shown in Figure F.1. The constructor of the *HMdcTrackFinder* class allows to set the mode of the track finder. In addition to that one more parameter can be set depending on whether the magnetic field was switched on or not. The task calculates the level of cluster finder as well, which can also be changed externally using corresponding methods provided by the class. The information about found clusters is stored in the *cat-MdcClus* category which stores instances of the *HMdcClus* class. The *HMdcClusterToHit* task fills the categories of the *HMdcSeg* and *HMdcHit* classes. The object of the *HMdcSeg* class contains all information about the track position in space. Using this information the intersection points with the mid planes of each chamber together with the hit directions (if the chamber is existing in the setup) are calculated and stored in the *HMdcHit* category, therefore, in some sense, these categories store the same information in different formats.

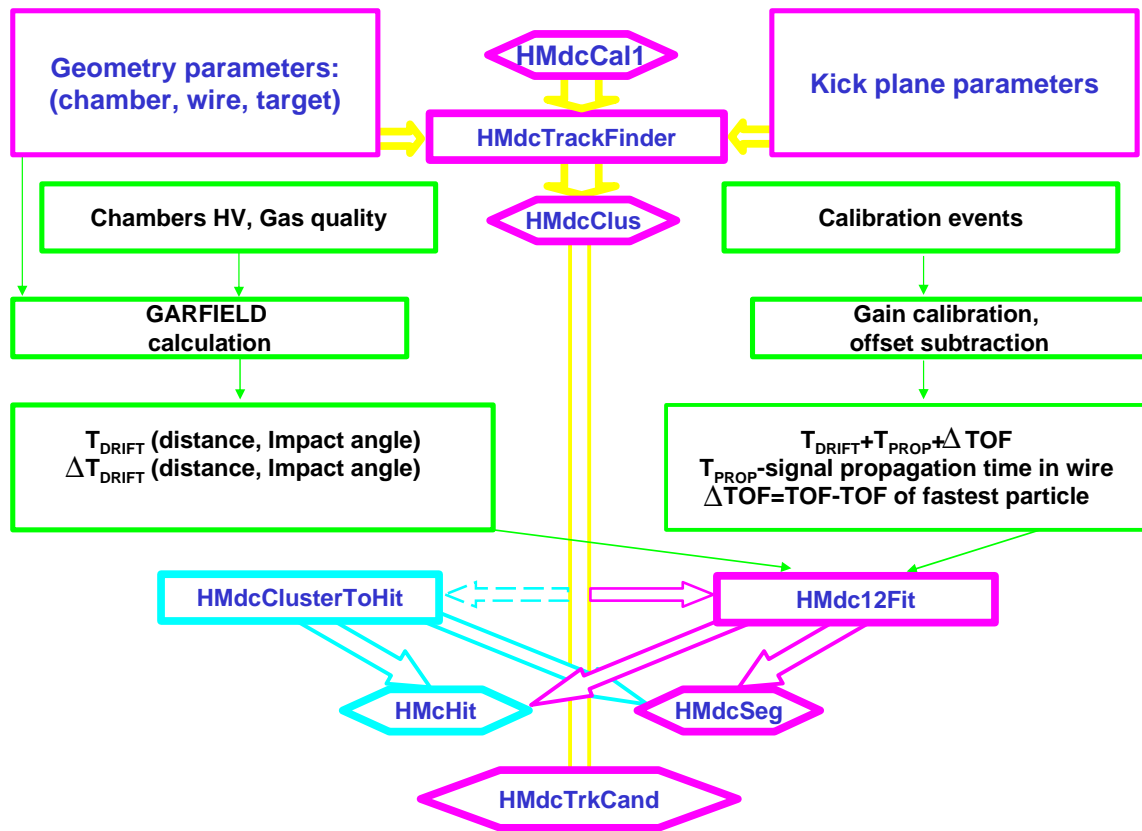


Figure F.1: Block diagram for track finder and fitter.

The track segment fitting is done with the task *HMdc12Fit* which takes the input from *HMdcClus* and fills the categories of *HMdcSeg* and *HMdcHit* classes. If the track was fitted the information in *HMdcSeg* and *HMdcHit* is updated with the fitted values, otherwise the information is left from cluster finder. The corresponding quality parameter of the track fitter, the χ^2 of the fit, is also a data member of the *HMdcSeg* class, whose value is set to -1 if it was decided that the fitting procedure has failed.

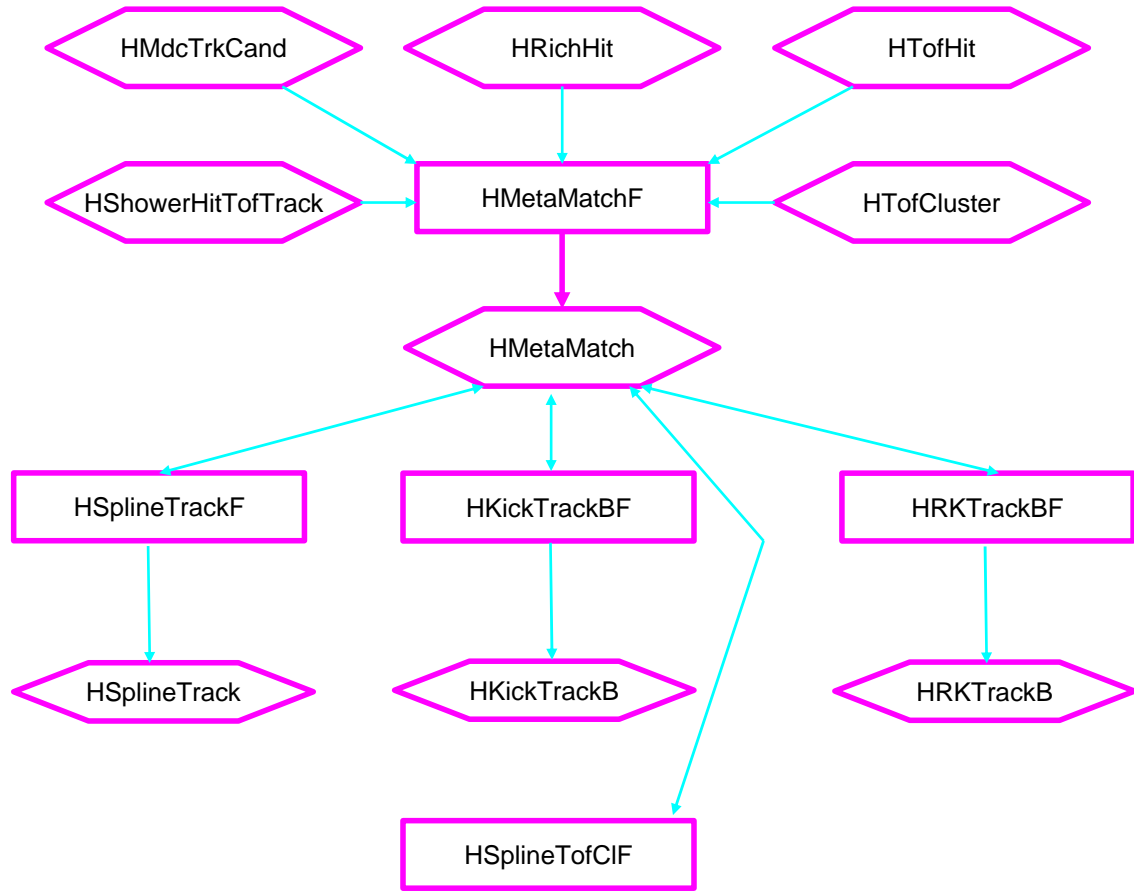


Figure F.2: Block diagram of matching code.

The matching code takes input information from the categories of *HMdcTrackCand* class which stores the indices of matched inner and outer segments in the category of *HMdcSeg* class, *HRichHit*, *HTofHit*, *HShowerHitTofTrack* storing the reconstructed hits from corresponding detector systems. The information about the tof clusters it takes from the category of *HTofCluster* class (See Figure F.2).

The main task for matching is called *HMetaMatchF* which performs an algorithm discussed in section 3.6 and creates the objects on *HMetaMatch* class.

As was explained before, e.g. in case of matching of track candidates with the META hits, one track candidate can match with several META hits as shown in Figure 3.8(a). In this case several instances of the *HMetaMatch* class will be created having the same track candidate (same inner and outer segments). Each instance of *HMetaMatch* object (yellow and green one in the Figure 3.8(a)) has a method for getting the first created object. (*HMetaMatch::getFirstTrackCand()* method). From the first object (green in Figure 3.8(a))

it is possible to obtain the next object by *HMetaMatch::getNextTrackCand()* method (the yellow in Figure 3.8(a)). For the last object the *HMetaMatch::getNextTrackCand()* returns -1. Furthermore, using the method *HMetaMatch::getNtrackCand()* it is possible to see how many times the given track candidate was matched with different META hits. The usefulness of this approach is that if, for example, one wants to calculate the momentum of the track for the *HMetaMatch* objects created in Figure 3.8(a) it is enough to calculate the momentum only for the first of them, as they have the same inner and outer segments. For the next objects it is enough only to recalculate the beta and path length of the track.

There are also methods giving a possibility to check how many times a given META hit was used with different track candidates and the corresponding methods for getting the next one.

If the matching with the META hit is done, the corresponding method *HMetaMatch::getSystem()* returns the value of 0 or 1 depending on whether the matching was done with SHOWER or TOF detectors correspondingly. In case of not matched META hits this method returns a value of -1.

The object of *HMetaMatch* keeps indices of all hits from different detector systems belonging to a given track. Furthermore it keeps matching qualities described in section 3.6.

The reconstruction of momentum starts taking an input information from the category of *HMetaMatch* class.

As there are several objects created from different momentum reconstruction methods and having the same data members the base class called *HBaseTrack* was created from which all the classes keeping an information about reconstructed momentum are inheriting.

The method of spline takes its input from the category of *HMetaMatch* class. The task which performs the momentum reconstruction is called *HSplineTrackF*. It calculates the momentum of the particle and the sign of the charge from inner and outer segments. If there is a matching with the META detectors the method calculates the path length and the velocity of the particle as well. The output is written to the category of *HSplineTrack* class which keeps the created objects of *HSplineTrack* class. The algorithm puts back into the *HMetaMatch* object (from which it has started) the index of the spline object in the category. If the object was created the corresponding method *HMetaMatch::isSplineAccepted()* is activated.

The algorithm of Runge Kutta is executed after the spline task. It starts from *HMetaMatch* objects which already have an index to the category of *HSplineTrack* from where the initial momentum and the polarity information can be taken. The angular information it takes using the index of *HMdcTrackCand* object which in turn keeps an index of *HMdcSeg* object. The output is written to *HRKtrackB* objects which are kept in the category of *HRKtrackB* class. The corresponding index of the created object in the category is written to the *HMetaMatch* object and the flag *HMetaMatch::isRungeAccepted()* is activated.

After the momentum reconstruction methods, the tof clustering task is running. This task takes care of Tof clusters and overlap between TOF and Shower detectors. In its

current design the task deactivates the corresponding *HMetaMatch::isAccepted()* flags for different methods for Tof hits entering the cluster and for SHOWER hits which are overlapping with Tof hits.

In order to keep compatibility with the kick plane algorithm, which works in case if there are no outer MDC chambers in the sector, the *HMetaMatch* objects are created even for the inner segments only (without outer segment). The kick plane algorithm has its own method of matching of segments with the *META* hits. The created objects from the kick plane method are compared with the objects of *HMetaMatch* class until the corresponding object is found. The index of the created *HKickTrackB* object is written to the *HMetaMatch* object. The corresponding flag of *HMetaMatch::isKickAccepted()* is set to true.

From a final user point of view the *HMetaMatch* object contains all necessary information for further analysis. By iteration over the category of the *HMetaMatch* class it is possible to obtain all necessary information for analysis. The example below shows how to obtain the momentum of the particle reconstructed by the spline method from *HMetaMatch* objects.

```

\\Retrieve a pointer to the categories
HEvent *event=HADES::instance()->GetCurrentEvent();
HCategory *cat=event->GetCategory(catMetaMatch);
HCategory *catSpline=event->GetCategory(catSpline);
Int_t splineInd=-1;
HSplineTrack *pSpline=NULL;
\\iterate over whole category
HIterator *iter=cat->MakeIterator();
iter->Reset();
HMetaMatch *temp=NULL;
while((temp=(HMetaMatch*)iter->Next())!=NULL)
{
    if(pMetaMatch->getSystem()==-1) continue; \\if there is
        matching with the META hit
    if(!(pMetaMatch->isSplineAccepted())) continue; \\if the
        spline objects exist?. Overlap and tof cluster checking.
    splineInd=pMetaMatch->GetSplineInd(); \\get an index of
    HSplineTrack object in the category
    pSpline=(HSplineTrack*)catSpline->GetObject(splineInd);\\get a
        pointer to the corresponding HSplineTrack object
    if(!pSpline) continue; \\check the pointer
    pSpline->getP(); \\get the momentum
}

```

Bibliography

- [1] K.N. Mukhin. *Experimental Nuclear Physics*. Moscow, 1993. In Russian. v, 3, 4, 77
- [2] L.G. Landsberg. Electromagnetic decays of light mesons. *Phys. Rep.*, 128,6:301–376, 1985. v, 4, 8, 9, 10, 108
- [3] R.P. Feynman. *Photon-Hadron Interactions*. W. A. Benjamin, Inc., 1972. 4, 6
- [4] J.J Sakurai. *Currents and Mesons*. THE UNIVERSITY OF CHICAGO PRESS, 1972. 4
- [5] Peter Koch. Low mass lepton pair production and pion dynamics in ultrarelativistic heavy ion collisions. *Z. Phys.*, C57:283–304, 1993. 6
- [6] C. Ernst, S. A. Bass, M. Belkacem, Horst Stoecker, and W. Greiner. Intermediate mass excess of dilepton production in heavy ion collisions at BEVALAC energies. *Phys. Rev.*, C58:447–456, 1998. 7, 108
- [7] M. R. Jane et al. *Phys. Lett.*, 59B:103, 1975. 9
- [8] H. Calen et al. Higher partial waves in $pp \rightarrow pp\eta$ near threshold. *Phys. Lett.*, B458:190–196, 1999. 10
- [9] M. Abdel-Bary et al. Measurement of the η production in proton proton collisions with the COSY time of flight spectrometer. *Eur. Phys. J.*, A16:127–137, 2003. 10
- [10] F. Balestra et al. Exclusive η production in proton-proton reactions. *Phys. Rev.*, C69:064003, 2004. 11, 81
- [11] I.Froelich. Hades internal report. 11, 81
- [12] D. Miśkowiec for the CERES collaboration. Recent results from CERES. *Quark Matter, Budapest*, 2005. 11
- [13] R. J. Porter et al. Dielectron cross section measurements in nucleus nucleus reactions at 1.0-A-GeV. *Phys. Rev. Lett.*, 79:1229–1232, 1997. 11, 14

- [14] J. Stroth for the HADES collaboration. Dielectrons as probes for the in-medium structure of hadrons. *DPG 2004, Koln*, Vortrag 2004. 11
- [15] P.Salabura for the HADES collaboration. Probing of in-medium hadron structure with HADES. *Nucl. Phys.*, A749:150–159, 2005. 11
- [16] R. Holzmann for the HADES collaboration. Di-electron mass spectrum in $^{12}\text{C}+^{12}\text{C}$ collisions at 2 AGeV by HADES. *Quark Matter, Budapest*, 2005. 11
- [17] Hendrik van Hees and Ralf Rapp. Medium modifications of vector mesons and NA60. 2006. 11
- [18] R. Rapp and J. Wambach. Chiral symmetry restoration and dileptons in relativistic heavy-ion collisions. *Adv. Nucl. Phys.*, 25:1, 2000. 11
- [19] Ralf Rapp and Jochen Wambach. Vector mesons in medium and dileptons in heavy-ion collisions. 1999. 11
- [20] J. Wambach and R. Rapp. Theoretical interpretations of low-mass dileptons. *Nucl. Phys.*, A638:171–182, 1998. 11
- [21] Tetsuo Hatsuda and Su Houng Lee. QCD sum rules for vector mesons in nuclear medium. *Phys. Rev.*, C46:34–38, 1992. 11
- [22] HADES collaboration. Proposal for High-Acceptance DiElectron Spectrometer. 1994. 14
- [23] P.Salabura et.al. HADES: High Acceptance DiElectron Spectrometer. *Nucl. Phys. Proc. Suppl*, 44:701–707, 1995. 14
- [24] R. Schicker et. al. Acceptance and resolution simulation studies for the dielectron spectrometer HADES at GSI. *Nucl. Instrum. Meth.*, A380:586–596, 1996. 14
- [25] E. Berdermann et. al. *Nucl. Phys. (Proc. Suppl.)*, B78:533–539, 1999. 15
- [26] P. A. Cherenkov. *Physical Review*, 52:378, 1937. 16
- [27] William R. Leo. *Techniques for Nuclear and Particle Physics Experiments*. Springer Verlag Berlin, 1994. 16
- [28] J. D. Jackson. *Classical Electrodynamics*. John Wiley and Sons, Inc., 1962. 16, 19
- [29] K. Zeitelhack et. al. The HADES RICH detector. *Nucl. Instrum. Meth.*, A433:201–206, 1999. 17

- [30] A. Toia. *Performance of the HADES Spectrometer for Dilepton Identification in the Reaction $C + C$ at 1 – 2 AGeV*. Dissertation, Justus-Liebig-Universität Gießen, 2004. 17
- [31] K. Hagiwara et al. *Physical Review*, D 66, 2002. 19
- [32] W. Blum and L. Rolandi. *Particle Detection with Drift Chambers*. Springer Verlag, CERN; European Organization For Nuclear Research, Geneva, 1993. 19, 20
- [33] H. Bokemeyer et al. Development of low-mass drift chambers for the HADES spectrometer. *Nucl. Instrum. Meth.*, A 477:397–400, 2002. 21
- [34] C. Müntz. The HADES Tracking System. *Nucl. Instrum. Meth.*, A535:242–246, 2004. 21
- [35] GARFIELD 7.02. Simulation of gaseous detectors; <http://www.cern.ch/garfield>; Online User Guide, 2000. 21
- [36] C. Garabatos et al. Optimisation of low-mass drift chambers for HADES. *Nucl. Instrum. Meth.*, A 412:38–46, 1998. 22
- [37] A. Godi et al. The HADES time-of-flight wall. *Nucl. Instrum. Meth.*, A494:14–25, 2002. 24
- [38] A. Balanda et al. The HADES Pre-Shower detector. *Nucl. Instrum. Meth.*, A531:445–458, 2004. 26
- [39] M. Atac, A. V. Tollestrup, and D. Potter. Selfquenching streamers. *Nucl. Instr. Meth.*, 200:345, 1982. 27
- [40] HADES Trigger Homepage in Gießen. <http://pcpig.physik.uni-giessen.de/hades/hades.htm>, 2000. Internetangebot der HADES Kollaboration in Gießen. 28
- [41] G. Agakichiev and V. Pechenov et.al. Fast method for track searching in multilayer drift chambers of the HADES experiment. *Particle and Nuclei, Letters*, 4,1001, 2000. 35
- [42] V. Pechenov, Private communications. 35, 39
- [43] G. Agakichiev, Private communications. 35, 39
- [44] A. Ierusalimov, Private communications. 39
- [45] A. Ierusalimov. Hades internal report. 2002. 39

- [46] I.A. Golutvin et.al. Optimal choice of track fitting procedure for contaminated data in high-accuracy cathode strip chambers. *Joint Institute for Nuclear Research, Preprint*. 39
- [47] A. Schmah. Alignment of the HADES spectrometer. *HADES internal report*, 2006. 43
- [48] M. Sánchez-García. *Momentum reconstruction and pion production analysis in the HADES spectrometer at GSI*. Dissertation, Universidade de Santiago de Compostela, 2003. 48, 49
- [49] Philip R. Bevington and D. Keith Robinson. *Data Reduction and Error Analysis*. McGraw-Hill, 2003. 51
- [50] H.Wind. Momentum analysis by using a quintic spline model for the track. *Nucl.Instrum.Meth.*, 115:431–434, 1974. 51
- [51] K. Kurek et al. An algorithm for track reconstruction in the large angle spectrometer of the COMPASS experiment. *Nucl. Instrum. Meth.*, A485:720–738, 2002. 51
- [52] R.K. Bock et.al. *Data Analysis Techniques for High-Energy Physics Experiments*. CAMBRIDGE UNIVERSITY PRESS, 2003. 51
- [53] N.S. Bakhvalov et.al. *Numerical Methods*. MIR, 2000. In Russian. 56
- [54] F. Halzen and Alan D. Martin. *Quarks and Leptons*. John Wiley and Sons, Inc., 1984. 75
- [55] H.Perkins. *Introduction to high energy physics*. Addison-Wesley Company, 1987. 75
- [56] L.F. Li T.P Cheng. *Gauge theory of elementary particle physics*. Oxford University Press, 1991. 75, 76
- [57] M.I Petrashen and E.D Trifonov. *Application of group theory to the quantum mechanics*. Moscow, 2002. In Russian. 75
- [58] Frederick J. Gilman and Russel Kauffman. The η η' mixing angle. *Phys. Rev.*, D36:2761, 1987. 77
- [59] A. Bramon, R. Escribano, and M. D. Scadron. The η η' mixing angle revisited. *Eur. Phys. J.*, C7:271–278, 1999. 77
- [60] M. Bardadin-Otwinowska et al. Six-prong interactions of π^+ mesons with protons at 8 gev/c. *Phys. Rev.*, D4:2711–2739, 1971. 77

- [61] A. Rustamov for the HADES coll. Meson production in pp collisions. *XLIV International Winter Meeting on Nuclear Physics, BORMIO, ITALY, 2006*. 77
- [62] C. Caso and A. Gurtu. The Z boson: in review of particle physics (rpp 1998). *Eur. Phys. J.*, C3:227–231, 1998. 79
- [63] E. Gedalin, A. Moalem, and L. Razdolskaja. A covariant OBE model for eta production in NN collisions. *Nucl. Phys.*, A634:368–392, 1998. 79
- [64] K. Nakayama, J. Speth, and T. S. H. Lee. η meson production in NN collisions. *Phys. Rev.*, C65:045210, 2002. 79
- [65] M. T. Pena, H. Garcilazo, and D. O. Riska. The reaction $pp \rightarrow pp\eta$ and the η nucleon and nucleon nucleon interactions. *Nucl. Phys.*, A683:322–338, 2001. 79
- [66] V. Baru et al. Production of η mesons in nucleon nucleon collisions. *Phys. Rev.*, C67:024002, 2003. 79
- [67] J. F. Germond and C. Wilkin. The $pp \rightarrow pp\eta$ reaction near threshold. *Nucl. Phys.*, A518:308–316, 1990. 80
- [68] Goran Faldt and Colin Wilkin. The production of η mesons in nucleon nucleon collisions near threshold. *Phys. Scripta*, 64:427–438, 2001. 80
- [69] K. Nakayama. Pseudoscalar and vector meson production in NN collisions. 2001. 80
- [70] M. A. Kagarlis. Pluto++. *GSI Report*, 2000-2003. 80
- [71] PLUTO. Pluto++, A Monte Carlo simulation tool for hadronic physics; <http://www-hades.gsi.de/>;, 2004. 80
- [72] HGEANT. HADES Simulation Package; <http://www-hades.gsi.de/>;, 2004. 80, 81
- [73] GEANT. Detector Description and Simulation Tool; <http://consult.cern.ch/writeup/geant/>; Online User Guide, 2004. 81
- [74] G.I. Kopilov. *Basics of Resonance Kinematics*. NAUKA, 1970. in Russian. 82
- [75] V.I. Moroz. Kinematic fit. *Preprint JINR, Dubna*, 1968. 94
- [76] S. Eidelman et al. *Phys. Lett.*, B 592(1), 2004. 110, 121
- [77] J. Markert. *Untersuchung zum Ansprechverhalten der Vieldraht-Driftkammern niedriger Massenbelegung des HADES Experimentes*. Dissertation, Fachbereich Physik der Johann Wolfgang Goethe-Universität der Johann Wolfgang Goethe-Universität, 2005. 135

Acknowledgments

I would like to thank:

- My supervisor, Prof. Dr. Peter Braun-Munzinger for inviting me to the HADES collaboration, for useful discussions, and for encouraging me in pursuing the goal.
- Dr. Ingo Froelich, Dr. Piotr Salabura, Prof. Dr. Joachim Stroth for a nice and useful discussions, "fresh" ideas during my data analysis.
- Prof. Dr. Herbert Ströbele, Dr. Jens Söeren Lang, Prof. Dr. Volker Metag.
- Dr. Heydar Agakishiyev, Mr. Alexander Ierusalimov and Dr. V. Pechenov for a help and discussions concerning both a technical and physics part, for a discussion about deep "secrets" of the HADES tracking.
- Dr. Romain Holzmann, for a lot of discussions about physics, software framework, "secrets" of Geant, and so on. I thank him also for reading first complete version of this thesis, and making valuable remarks.
- Dr. Christian Sturm for reading some parts of this thesis and making nice remarks.
- My roommates: Alexander Schmah, Dr. Jochen Markert, Yvonne Pachmayer, Khaled Teilab, Dr. Jörn Wüstenfeld and Dr. Peter Zumbruch for nice working atmosphere. I thank them also for their help especially with the German language.
- Tetyana Galatyuk, Dr. Burkhard Kolb, Dr Wolfgang König, Dr. Ilse König, Simon Lang, Dr. Christian Müntz, Dr. Jerzy Pietraszko, Dr. Mateusz Ploskon, Malgorzata Sudol for their help and friendship.
- Dr. Mohammad Al-Turany, Dr. Denis Bertini and A. Manafov for a nice discussions concerning especially software.
- My parents for they care and a lot of help

- My wife, without her help it would be impossible to finish this work, at least in time. I also thank our 1 year old daughter, in spite of the fact that she several times destroyed parts of this thesis, computer and my books. Of course all this brought only beauty to that parts.

Resume

Name: Anar Rustamov

Date of Birth: April 16, 1977 Shamakhi, Azerbaijan

Address: Gesellschaft für Schwerionenforschung mbH Planckstrasse 1 D-64291, Darmstadt, Germany

Tel: +49 6159 711303

Email: A.Rustamov@gsi.de

Education :

1983-1994 School

1994-1998 Baku State University, Physics Department, Bachelor degree

1998-2000 Baku State University, Physics Department, Master degree

2000-2002 Scientific researcher, Joint Institute for Nuclear Research, Laboratory of Particle Physics, Moscow region, Dubna

2002-2003 Guest Scientist, Gesellschaft für Schwerionenforschung mbH, Darmstadt, Germany

2003-2006 Technical University of Darmstadt Ph.D in Physics supervised by Prof. Dr. Peter Braun-Munzinger